Large Deformations of Polymers

Lindgreen, Britta

Publication date:
2008

Document Version
Publisher's PDF, also known as Version of record

Technical University of Denmark

Large Deformations of Polymers

Britta Lindgreen
PhD thesis
February 2008

DCAMM Special Report No. S104

Department of Mechanical Engineering

DTU Mekanik

Solid Mechanics

Large deformations of polymers

by

Britta Lindgreen

DEPT. OF MECHANICAL ENGINEERING
Solid Mechanics

TECHNICAL UNIVERSITY OF DENMARK

Preface

This thesis is submitted in partial fulfillment of the requirements for obtaining the degree of Ph.D. in mechanical engineering. The work was carried out at the Department of Mechanical Engineering, Solid Mechanics, Technical University of Denmark in the period March 2005 - February 2008, with Professor Dr. techn. Viggo Tvergaard as supervisor. The Ph.D. study was financially supported by The Technical University of Denmark.

First, I would like to thank my supervisor Professor Viggo Tvergaard for his outstanding support and for many valuable discussions during the project.

Part of this work was carried out with Professor Alan Needleman, Brown University, during a 4 month stay at Brown University in the autum 2006. I am very grateful to Professor Needleman for making this stay possible and for the friendly and inspiring atmosphere during my visit.

Finally, I would like to express my gratitude to my colleagues and fellow Ph.D. students at the department for helpfull discussions and suggestions as well as for creating a friendly, humorous and inspiring environment.

Kgs. Lyngby, 29. February 2008

Britta Lindgreen

Abstrakt (in Danish)
Polymerer udsat for store deformationer

Denne afhandling omhandler polymerers mekaniske opførsel. Numeriske beregninger er blevet udført ved anvendelse af to forskellige elastisk-viskoplastiske konstitutive modeller, som er specielt udviklede til at modellere polymerers sande ulineære opførsel. Fokus er på forskellige typer af problemer, der involverer polymerers mekaniske opførsel, og det hele løses med en implementering af modellen i et dynamisk finite element program. Eksempler på indsnøring og buling i symmetriske polymer rør samt dannelse af en zone med høje tværtøjninger i et polymer imellem fiberender, der overlapper, betragtes og diskuteres. Udbredelse af indsnøringer og plastisk blødgøring efterfulgt af hærdning, der fører til blokering over for yderligere deformation, observeres. Dette er polymer karakteristika i overensstemmelse med eksperimenter nævnt i litteraturen. Endelig viser ekstra vedlagte analyser, at graden af indsnøring og den generelle opførsel ved indsnøring afhænger af materialevalget.

Abstract
Large deformations of polymers

Numerical analyses that predict the mechanical behaviour of polymer materials have been carried out applying two different finite strain elastic–viscoplastic constitive relations that are particularly developed to model the true nonlinear behaviour of polymers. Focus in the present thesis is on investigating a number of polymer cases, which are considered using a dynamic finite element program with the constitutive model implemented. Examples of necking and bulging in symmetric polymer tubes as well as shear zone development in a polymer between overlapping fiber ends are presented and discussed. Polymer characteristics such as neck propagation and plastic softening followed by network hardning leading to network locking are observed which are in agreement with experiments known from the litterature. Finally, a few extra computations illustrating the extent of neck thinning and the necking behaviour to be rather material dependent are included.

Publications

The following publications are part of the thesis:

[P1] Lindgreen, B. and Tvergaard, V. and Needleman, A., 2008. Dynamic neck development in a polymer tube under internal pressure loading. *International Journal of Solids and Structures* **45**, 580-592.

[P2] Lindgreen, B. and Tvergaard, V. and Needleman, A., 2007. Bulge formation and necking in a polymer tube under dynamic expansion. *Submitted.*

[P3] Lindgreen, B., 2007. Analysis of a high intensity shear zone between overlapping fiber ends in a polymer matrix composite. *Accepted for publication in European Journal of Mechanics - A/Solids.*

Contents

Chapter 1
Introduction

A significant amount of work has been performed on predicting the mechanical behaviour of polymer materials. Polymers deform as elastic–plastic materials in the sense that elastic deformations initially occur while at a certain stress level plastic deformations initiate resulting in an irreversible stress-strain history. In several analyses the material behaviour has been modelled using the classical elastic–plastic material models developed for describing metal plasticity. However, this requires the plastic behaviour to be sensitive to hydrostatic pressure and that is usually not the case for material models representing metals. Another problem is that before plasticity is reached the elastic strains grow more than ten times as large as is the case for metals. Therefore larger strains must be assumed when the material behaviour of a polymer is to be modelled. Moreover, a stress peak usually appears at the stress–strain response marking a roll over from elastic deformation to plastic softening. Plastic softening causes the stress to decrease until, due to network hardening, a significant stress increase is achieved. This kind of material behaviour is very difficult to model with a classical constitutive model predicting the mechanical behaviour of metals.

It is the main purpose of the present thesis to apply more complex, nonlinear material models particularly developed to model the mechanical behaviour of polymers under large deformations in order to numerically analyse the true behaviour of a polymer material under different loading conditions and applications. The constitutive models used are based on material relations proposed by Boyce and co–workers (Boyce et al. (1988), Boyce and Arruda (1990), Arruda and Boyce (1993), Boyce et al. (2000), Mulliken and Boyce (2006)) with a version that is adopted by Wu and Van der Giessen (1996) and further used by Tvergaard and Needleman (2008).

Considering the stress-strain responses of a polymer, uniaxial compression experiments carried out by Mulliken and Boyce (2006) suggest that a realistic material model should include general material characteristics such as initial linear elastic deformation that is followed by softening in the nonlinear plastic regime with network hardening taking over at large strains. When the initial purely elastic deformation switches to the plastic decrease of stress a stress peak is left on the response to mark the initiation of plastic straining. As the increased network stiffness at large strains introduces very high stresses the network finally locks and essentially stops the plastic deformation. In the present thesis two different models (though sharing the main relations) introduced by Boyce, Van der Giessen and co–workers that satisfy these requirements are to be presented.

A plane large-strain dynamical program based on general continuum mechanics has been developed by the author of this thesis where the polymer material is described mechanically using constitutive relations that are based on adding deformation resistances. This very realistic material model is introduced by Boyce et al. (2000). Also a constitutive relation based on a back stress formulation has been implemented numerically in full three

dimensions by Tvergaard and Needleman (2008). The relation is adopted from Wu and Van der Giessen (1996) and developed from Boyce and co–workers (Boyce et al. (1988), Boyce and Arruda (1990), Arruda and Boyce (1993), Mulliken and Boyce (2006)). The plane strain program developed by the author is used for carrying out the analyses of high intensity shear zones in paper [P3], while the three dimensional program of Tvergaard and Needleman (2008) is applied in order to perform the tube analyses in papers [P1]–[P2]. Here the author has added the internal pressure loading and implemented the cylindrical tube analyses.

The basis for the two constitutive models used is the division of of the rate of deformation into an elastic and a plastic contribution. Also the plastic strain rate expression, that among others introduces a stress decay after initial elastic deformation, is identical for both models as is the hardness function specifying the extent of softening. For the two models considered a similar eight chain model is presented that essentially incorporates the network hardening leading to high stresses at large strains.

Principally, the material model used in the present thesis can be applied in order to numerically describe any polymer that shares the material characteristics mentioned above, but here the main focus will be on the group of thermoplasts including polycarbonate (PC), polyethylene (PE) or polyethylene terephthalate (PET), polymethyl methacrylate (Acrylic, PMMA) and acrylonitrile butadiene styrene (ABS). In this thesis PC is the main material chosen to represent the group of thermoplasts. Many of the material parameters needed are not measureable physical quantities defined for the polymer, but mostly numerical values that have to be specified by fitting the numerical data to existing experimental data.

Here, analyses of necking, neck propagation and bulge formation in polymer tubes are to be presented and discussed as has been the case for metal rings (Niordson (1965), Han and Tvergaard (1995)) and tubes (Larsson et al. (1982), Tvergaard (1990), Mikkelsen and Tvergaard (1999)). Neck propagation is a polymer phenomenon occurring once the necks have initiated as observed experimentally for tensile specimens by G'Sell and Jonas (1979) and Marquez-Lucero et al. (1989). Also the occurrence of high intensity shear zones between stiff overlapping fiber ends in a polymer matrix is investigated since they might cause debonding or matrix failure (Fleck (1997)), fiber pull out etc. as shown experimentally by Hampe and Marotzke (1992) and Andrews et al. (1994).

It has been chosen to include the three papers [P1]-[P3] that are written during the authors Ph.D study at the end of this thesis. The two first papers are written with coauthors and the last paper is written by the author herself. The two constitutive polymer models as well as the numerical formulation are described in Chapter 2. Chapter 3 contains a summary of the results presented in the three papers included and Chapter 4 contains the discussion. Extra results that were carried out at the end of the authors Ph.D study are added as the last section of Chapter 3.

The paper 'Dynamic neck development in a polymer tube under internal pressure loading', [P1], coauthored with Viggo Tvergaard and Alan Needleman focuses on initiation and growth of necks in polymer tubes subjected to rapidly increasing internal pressure assuming plane strain conditions to prevail in the axial direction. The sentivity to long

wave length and short wave length thickness imperfections is studied and polymer characteristics such as neck propagation and network hardening are analysed.

In the paper 'Bulge formation and necking in a polymer tube under dynamic expansion', [P2], coauthored with Viggo Tvergaard and Alan Needleman analyses of bulging and necking in long thin polymer tubes under increasing internal pressure loading are carried out numerically. Neck propagation in both axial and circumferential direction is observed and two different loading conditions, either linearly increasing pressure or linearly increasing enclosed volume, are studied. An extended abstract summing up the main ideas and the conclusion in paper [P2] was completed for a conference held in Gothenburg, Sweden (Lindgreen et al. (2007)).

The third paper 'Analysis of high intensity shear zone between overlapping fiber ends in a polymer matrix composite', [P3], deals with plane strain numerical analyses of high intensity shear zone development in a stiff fiber reinforced polymer. The influence of different ratios of the elongation strain and the transverse strain on shear zone development is studied together with the effect of fiber spacing and fiber thickness. A case assuming periodicity is included as well.

Finally, extra investigations of plane strain polymer tubes using a different polymer material than that of paper [P1]-[P3] reveal the extent and the mode of necking to be strongly material dependent. This is in good agreement with experiments carried out by Kyriakides (2007) for polyethylene.

Chapter 2
Model description

A contitutive relation for the polymer is needed in order to solve the problem numerically. In the paper [P3] an elastic–viscoplastic polymer model mainly adopted from Boyce et al. (2000) is used, but some changes are made to introduce softening when plastic deformation initiates since softening is not incorporated in the original model of Boyce et al. (2000). The changes are based on the mathematical formulations proposed by Boyce and co-workers (Boyce et al., 1988; Boyce and Arruda, 1990; Arruda and Boyce, 1993; Mulliken and Boyce, 2006) and references are drawn to Lai and Van der Giessen (1997) and Tvergaard and Needleman (2008) as well.

In the papers [P1]–[P2] another elastic–viscoplastic polymer model is applied based on models introduced by Boyce and co–workers (Boyce et al., 1988; Boyce and Arruda, 1990; Arruda and Boyce, 1993; Mulliken and Boyce, 2006), but adopted from Wu and Van der Giessen (1996) and most recently used in Tvergaard and Needleman (2008).

Both constitutive relations model the characteristics of a thermoplast polymer where the initial linear elastic deformation is followed by softening in the plastic regime with final hardening occurring at large strains. Though many of the equations of the two models are somewhat similar, the derived overall constitutive relations of the respective models are different.

Section 2.1 presents the contitutive relation first mentioned above which is based on the main idea of adding deformation resistances whereas the second constitutive relation to be described in Section 2.2 essentially features a back stress formulation. For the case considered in Section 2.2, also the Jauman rate of the stress is needed in order to update the stress and a rate tangent expression to update the plastic contribution is introduced.

2.1 Constitutive relations based on adding deformation resistances

In the following the elastic part of the deformation is handled by a linear hyperelastic equation since nonlinear elastic effects are neglected. Moreover, there is a clear distinction between the Cauchy stress $\boldsymbol{\sigma}$ and the Kirchhoff stress $\boldsymbol{\tau}$.

According to Boyce et al. (2000) the overall deformation resistance is divided into an intermolecular resistance A acting in parallel with a network resistance B. The deformation resistance A is further divided into an elastic $(\ )^e$ and plastic $(\ )^p$ contribution and the deformation resistance B is divided into stretching/orientation $(\ )^n$ of the molecular network and molecular relaxation $(\ )^f$. The total deformation gradient, $\boldsymbol{F}$, is the very same for each resistance and the total stress $\boldsymbol{\sigma}$ acting on the system has a contribution from each resistance. The present model is applied in paper [P3].

2.1.1 Material model

At first all contribution from resistance A is studied. Resistance A can be separated into an initial elastic deformation $(\,)^e$ and a plastic deformation $(\,)^p$ where the plastic deformation does not initiate before the stress has reached a critical level where the energy barrier to molecular chain segment rotation is overcome. At this stage a softening flow takes over so that the stress decreases during continued deformation leaving a stress peak on the stress–strain response which indicates the roll over to flow. The initial purely elastic deformation occurs from van der Waal interactions with the surrounding molecules.

The underlying basis is grounded on the total rate of deformation tensor $\boldsymbol{D}$ that is prescribed as

$$\boldsymbol{D} = \boldsymbol{D}^e + \boldsymbol{D}^p \tag{2.1}$$

where $\boldsymbol{D}^e$ is the elastic contribution and $\boldsymbol{D}^p$ to be the plastic contribution. The rate of deformation tensor, $\boldsymbol{D}$, is defined as the symmetric part of the velocity gradient tensor $\boldsymbol{L}$ that is given by

$$\boldsymbol{L} = \dot{\boldsymbol{F}}\boldsymbol{F}^{-1} \tag{2.2}$$

The deformation gradient $\boldsymbol{F}$ can be decomposed into an elastic deformation gradient $\boldsymbol{F}^e$ and a plastic deformation gradient $\boldsymbol{F}^p$ through mulitiplicative decomposition

$$\boldsymbol{F} = \boldsymbol{F}^e\boldsymbol{F}^p \tag{2.3}$$

where the elastic and the plastic deformation gradients can be further decomposed into stretch $\boldsymbol{V}$ and rotation $\boldsymbol{R}$ components

$$\boldsymbol{F}^e = \boldsymbol{V}^e\boldsymbol{R}^e \qquad , \qquad \boldsymbol{F}^p = \boldsymbol{V}^p\boldsymbol{R}^p \tag{2.4}$$

Now, by substituting eq. (2.3) into eq. (2.2) $\boldsymbol{L}$ in eq. (2.2) changes into

$$\boldsymbol{L} = (\dot{\boldsymbol{F}}^e\boldsymbol{F}^p + \boldsymbol{F}^e\dot{\boldsymbol{F}}^p)(\boldsymbol{F}^e\boldsymbol{F}^p)^{-1} = \dot{\boldsymbol{F}}^e\boldsymbol{F}^p\boldsymbol{F}^{e-1}\boldsymbol{F}^{p-1} + \boldsymbol{F}^e\dot{\boldsymbol{F}}^p\boldsymbol{F}^{e-1}\boldsymbol{F}^{p-1} \tag{2.5}$$

from where a new expression for $\boldsymbol{L}$ is found

$$\boldsymbol{L} = \dot{\boldsymbol{F}}^e\boldsymbol{F}^{e-1} + \boldsymbol{F}^e\dot{\boldsymbol{F}}^p\boldsymbol{F}^{p-1}\boldsymbol{F}^{e-1} = \boldsymbol{L}^e + \tilde{\boldsymbol{L}}^p \tag{2.6}$$

rearranging the terms in eq. (2.5) and applying $\boldsymbol{F}^p\boldsymbol{F}^{p-1} = \boldsymbol{I}$, $\boldsymbol{I}$ being the identity matrix. Applying that

$$\tilde{\boldsymbol{L}}^p = \boldsymbol{D}^p + \tilde{\boldsymbol{W}}^p \tag{2.7}$$

the decompostion in an elastic and a plastic term is made unique by specifying the spin tensor $\tilde{\boldsymbol{W}}^p = 0$ so that rotations are included in the elastic part $\boldsymbol{W}^e$. Comparison of the expression in eq. (2.7) with the plastic expression in eq. (2.6) yields

$$\boldsymbol{D}^p = \boldsymbol{F}^e\dot{\boldsymbol{F}}^p\boldsymbol{F}^{p-1}\boldsymbol{F}^{e-1} \tag{2.8}$$

Isolating the term $\dot{\boldsymbol{F}}^p$ in eq. (2.8) gives

$$\boldsymbol{F}^{e-1}\boldsymbol{D}^p\boldsymbol{F}^p\boldsymbol{F}^e = \dot{\boldsymbol{F}}^p \tag{2.9}$$

and so using $\boldsymbol{F} = \boldsymbol{F}^e\boldsymbol{F}^p$ from eq. (2.3) an expression for $\dot{\boldsymbol{F}}^p$ is derived

$$\dot{\boldsymbol{F}}^p = \boldsymbol{F}^{e-1}\boldsymbol{D}^p\boldsymbol{F} \tag{2.10}$$

from where $\boldsymbol{F}^p$ is updated by adding $\dot{\boldsymbol{F}}^p$ multiplied by the time increment Δt to the old value of $\boldsymbol{F}^p$. Subsequently, the elastic contribution, $\boldsymbol{F}^e$, is found from eq. (2.3) by inverting the plastic deformation gradient so that

$$\boldsymbol{F}^e = \boldsymbol{F}\boldsymbol{F}^{p-1} \tag{2.11}$$

The rate of plastic deformation, $\boldsymbol{D}^p$, is prescribed constitutively as

$$\boldsymbol{D}^p = \dot{\gamma}^p\boldsymbol{p}_A \tag{2.12}$$

with the plastic strain rate $\dot{\gamma}^p$ regarded to follow a thermally activated proces defined by (from Tvergaard and Needleman (2008))

$$\dot{\gamma}^p = \dot{\gamma}_0 \exp\left[-\frac{\Delta G}{kT}\left\{1 - \left(\frac{\tau}{s - \alpha(\mathrm{tr}\boldsymbol{\sigma})/3}\right)^m\right\}\right] - \dot{\gamma}_0 \exp\left[-\frac{\Delta G}{kT}\right] \tag{2.13}$$

Here, m, $\dot{\gamma}_0$, the energy barrier to flow ΔG and α are material constants, T is the temperature measured in Kelvin and k is Boltzmann's constant $k = 1.38 \cdot 10^{-23}$ J/K. The last term in eq. (2.13) is included so that $\dot{\gamma}^p = 0$ when $\tau = 0$. A decrease of $\dot{\gamma}_0$ defers the softening (through the plastic contribution) in the sense that it causes a higher stress peak at a larger strain at the point where the roll over from the elastic deformation to plastic softening takes place. If the constant m is increased the material will show less rate dependence even at small strains.

Here, $\boldsymbol{p}_A$ is the normalized deviatoric stress acting on resistance A

$$\boldsymbol{p}_A = \frac{\boldsymbol{\sigma}'_A}{\sqrt{2}\tau_A} \qquad \tau_A = \sqrt{\frac{1}{2}\boldsymbol{\sigma}'_A\boldsymbol{\sigma}'_A} \tag{2.14}$$

where $(\ )'$ denotes the deviatoric quantities. The stress $\boldsymbol{\sigma}_A$ is found from the elastic deformation gradient through

$$\boldsymbol{\sigma}_A = \frac{1}{J_A}L^e \ln\boldsymbol{V}^e \tag{2.15}$$

with the volume change $J_A = \det\boldsymbol{F}^e$ and the fourth order tensor L^e of elastic constants defined by

$$L^e_{ijkl} = \frac{E}{1+\nu}\left[\frac{1}{2}\left(\delta_{ik}\delta_{jl} + \delta_{il}\delta_{jk}\right) + \frac{\nu}{1-2\nu}\delta_{ij}\delta_{kl}\right] \tag{2.16}$$

applying the elasticity modulus E and Poisson's ratio ν. The strain $\ln\boldsymbol{V}^e$ is calculated using $(\boldsymbol{V}^e)^2 = \boldsymbol{F}^e\boldsymbol{F}^{eT}$.

The deformation resistance s in eq. (2.13) is taken to have the initial value s_0 and to evolve from

$$\dot{s} = h\left(1 - \frac{s}{s_{ss}}\right)\dot{\gamma}^p \tag{2.17}$$

which introduces the stress decrease through eq. (2.13) when the roll over from the stiff linear elastic deformation to plastic deformation occurs. The softening constants h and s_{ss} are material dependent and generally speaking they determine the extent of softening with h terming the slope of the softening drop with respect to plastic strain. A smaller softening constant s_{ss} introduces more pronounced softening since s_{ss} is the value that s reaches at steady state. The initial value of s is defined at the upper yield point and it may be designated the athermal shear yield strength, s_0, of the material. It is given as

$$s_0 = \frac{0.077\mu}{1-\nu} \tag{2.18}$$

where μ is the temperature-dependent shear modulus. The eq. (2.17) is not included in the version of Boyce et al. (2000), but has been used in Boyce et al. (1988), Boyce and Arruda (1990), Arruda and Boyce (1993), Mulliken and Boyce (2006), Wu and Van der Giessen (1996) and most recently it was applied by Tvergaard and Needleman (2008).

Now, all contribution from resistance B is to be defined. Resistance B is divided into stretching/orientation of the underlying molecular network $(\ )^n$ and molecular relaxation $(\ )^f$. The significant network hardening that is obtained at large strains is a consequence of a resistance against further stretching/orientation of the network that finally results in network locking of the polymer. This mechanism is to be introduced in the following through the $(\ )^n$–term. The molecular relaxation $(\ )^f$ is present for polymers above the glass transition temperature only.

First, the rate of deformation tensor $\boldsymbol{D}$ is written as a summation of stretching/orientation and relaxation

$$\boldsymbol{D} = \boldsymbol{D}^n + \boldsymbol{D}^f \tag{2.19}$$

Subsequently, the total deformation gradient $\boldsymbol{F}$ is decomposed into network stretching/-orientation of the molecular network and molecular relaxation

$$\boldsymbol{F} = \boldsymbol{F}^n \boldsymbol{F}^f \tag{2.20}$$

which is very similar to the elastic–plastic decomposition in eq. (2.3). Corresponding to $\dot{\boldsymbol{F}}^p$, eq. (2.10), derived for the elastic–plastic decomposition, $\dot{\boldsymbol{F}}^f$ for the stretching-relaxation decomposition is found to be

$$\dot{\boldsymbol{F}}^f = \boldsymbol{F}^{n-1}\boldsymbol{D}^f\boldsymbol{F} \qquad , \qquad \boldsymbol{F}^n = \boldsymbol{F}\boldsymbol{F}^{f-1} \tag{2.21}$$

by inserting eq. (2.20) into eq. (2.2) and comparing with the expression $\boldsymbol{L} = \boldsymbol{L}^e + \boldsymbol{D}^f + \tilde{\boldsymbol{W}}^f$ having the spin tensor $\tilde{\boldsymbol{W}}^f = 0$. The last term in eq. (2.21) has been derived by the use of eq. (2.20). Not surprisingly, eq. (2.21) is very similar to the expressions given in eq. (2.10) and eq. (2.11) since the rate kinematics for resistance B are similar to those given for resistance A.

The rate of deformation caused by molecular relaxation is given as

$$\boldsymbol{D}^f = \dot{\gamma}^f \boldsymbol{p}_B \tag{2.22}$$

with the normalized deviatoric stress

$$\boldsymbol{p}_B = \frac{\boldsymbol{\sigma}'_B}{\sqrt{2}\tau_B} \qquad \tau_B = \sqrt{\frac{1}{2}\boldsymbol{\sigma}'_B\boldsymbol{\sigma}'_B} \tag{2.23}$$

Also, as a consequence of stress supported chain reptation the rate of relaxation is

$$\dot{\gamma}^f = \frac{C}{\lambda_f - 1}\tau_B \tag{2.24}$$

where the constitutive relation in eq. (2.24) is developed by Bergstrom and Boyce (1998) based on a theory of reptational motion of chain molecules presented by Doi and Edwards (1986). The value C introduces the temperature dependence of relaxation and is together with λ_f calculated from the relations

$$\lambda_f^2 = \frac{1}{3}\mathrm{tr}(\boldsymbol{F}^f\boldsymbol{F}^{fT}) \qquad C = D\exp\left[-\frac{Q}{RT}\right] \tag{2.25}$$

with D, Q as material dependent constants and R is the gas constant. The relaxation part is needed only when the polymer studied has a temperature above that of the glass transition which is not the case in paper [P3]. Therefore, in paper [P3] where this model is used the network relaxation is disabled keeping $\dot{\gamma}^f = 0$ in eq. (2.22) and so the model of Boyce et al. (2000) reduces to that of Boyce et al. (1988).

Stretching/orientation of the underlying molecular network results in a stress $\boldsymbol{\sigma}_B$ that is calculated using the eight chain rubber–elasticity model (Boyce et al. (1988))

$$\boldsymbol{\sigma}_B = \frac{1}{J_B}\frac{C_R}{3}\frac{\sqrt{N}}{\lambda_c}\beta_c(\boldsymbol{B}^n - \lambda_c^2\boldsymbol{I}) \tag{2.26}$$

where $\boldsymbol{B}^n = J_B^{-2/3}\boldsymbol{F}^n\boldsymbol{F}^{nT}$, $J_B = \det\boldsymbol{F}^n$, C_R and $\sqrt{N}$ are specified material constants and

$$\lambda_c^2 = \frac{1}{3}\mathrm{tr}\boldsymbol{B}^n \qquad \beta_c = \mathcal{L}^{-1}\left(\frac{\lambda_c}{\sqrt{N}}\right) \tag{2.27}$$

with

$$\mathcal{L}(x) = \coth(x) - \frac{1}{x} \tag{2.28}$$

The relation in eq. (2.26) is derived assuming the network to consist of eight polymer chains that are non–Gaussian. Each chain stretches and rotates when the polymer is deformed and the matching stretch on each chain in the network is λ_c. The dramatic stress increase that is observed from the stress–strain response at large strains is implemented in the constitutive model through the inverse Langevin function $\mathcal{L}^{-1}$. From the relations stated above the stress is directly seen to rise significantly when λ_c approaches $\sqrt{N}$ which results in high stiffness against further deformation and finally locks the polymer.

The total Cauchy stress $\boldsymbol{\sigma}$ acting on the system is then found from adding the stress contributions

$$\boldsymbol{\sigma} = \boldsymbol{\sigma}_A + \boldsymbol{\sigma}_B \tag{2.29}$$

of each of the two resistances A and B.

All stresses mentioned previously in this section are Cauchy stresses in a current configuration defined with respect to a coordinate system (in a fixed Cartesian frame) that will be found for the individual cases considered in section 3 whereas the contravariant components τ^{ij} of Kirchhoff stress appearing in the principle of virtual work that is to be described subsequently in section 2.1.2 are components on the deformed convected coordinate system. Kinematical relations are applied as described in section 2.1.2 in order to calculate the Kirchhoff stresses from the Cauchy stresses defined in eq. (2.29).

2.1.2 Numerical formulation

The dynamic principle of virtual work is used to obtain the numerical solutions and it is written as

$$\int_V \tau^{ij}\delta\eta_{ij}\,dV = \int_S T^i\delta u_i\,dS - \int_V \rho\frac{\partial^2 u^i}{\partial t^2}\delta u_i\,dV \tag{2.30}$$

with

$$T^i = (\tau^{ij} + \tau^{kj}u^i_{,k})\nu_j \tag{2.31}$$

$$\eta_{ij} = \frac{1}{2}(u_{i,j} + u_{j,i} + u^k_{,i}u_{k,j}) \tag{2.32}$$

where V and S are the volume and surface of the body in the reference configuration, $(\ )_{,i}$ denotes covariant differentiation in the reference frame, ν_j and u_j are the covariant components of the reference surface normal and displacement vectors, respectively, and ρ is the mass density.

The tensor τ^{ij} is mentioned previously in section 2.1.1 and it is calculated according to Budiansky (1969)

$$\tau^{ij} = \sqrt{\frac{G}{g}}\sigma^{ij} \tag{2.33}$$

with σ^{ij} being the contravariant components of the Cauchy or true stress presented in eq. (2.29) and $\sqrt{\frac{G}{g}}$ is the ratio of current to reference volume where g and G are the determinants of the metric tensors g_{ij} and G_{ij} respectively (in reference configuration versus current configuration) and they are defined as

$$g_{ij} = \boldsymbol{e}_i\cdot\boldsymbol{e}_j \qquad , \qquad G_{ij} = \bar{\boldsymbol{e}}_i\cdot\bar{\boldsymbol{e}}_j \tag{2.34}$$

The covariant base vectors are specified by

$$\boldsymbol{e}_i = \frac{\partial \boldsymbol{r}}{\partial \xi^i} \qquad , \qquad \bar{\boldsymbol{e}}_i = \frac{\partial \bar{\boldsymbol{r}}}{\partial \xi^i} = \boldsymbol{e}_i + u^k_{,i}\boldsymbol{e}_k \tag{2.35}$$

where ξ^i are coordinates of the convected coordinate system that deforms with the material and u^k the are the contravariant displacement components. Furthermore, the Cauchy stress components needed in eq. (2.33) are given as

$$\sigma^{ij} = \bar{\boldsymbol{e}}^i\cdot\boldsymbol{\sigma}\cdot\bar{\boldsymbol{e}}^j \tag{2.36}$$

with the contravariant base vectors $\bar{\boldsymbol{e}}^i = G^{ij}\bar{\boldsymbol{e}}_j$.

The finite element method has been chosen to discretise and solve the numerical equations where the calculations are carried out using a convected coordinate Lagrangian formulation. The total volume V is divided into a finite number of K elements such that

$$V = \sum_{k=1}^{K} V_{(k)} \qquad , \qquad S = \sum_{k=1}^{K} S_{(k)} \tag{2.37}$$

Each element k contains a number of nodes that connects the element to the other elements forming the total volume and the K elements (subvolumes) represent a mesh altogether. For the plane strain case considered in paper [P3] the meshes consist of eight node isoparametric elements whereas in the papers [P1]–[P2] the calculations are based on a full three dimensional implementation with the mesh consisting of twenty node brick elements.

Inside the volume $V_{(k)}$ the displacement components u_i are expressed in terms of F_e different displacement fields $U_i^{(n)}$ as

$$\begin{gathered} u_i = \textstyle\sum_{n=1}^{F_e} U_i^{(n)} D_{(n)} \quad , \quad \eta_{ij} = \textstyle\sum_{n=1}^{F_e} E_{ij}^{(n)} D_{(n)} \\ E_{ij}^{(n)} = \tfrac{1}{2}\Big(U_{i,j}^{(n)} + U_{j,i}^{(n)} + u_{,i}^{k} U_{k,j}^{(n)} + u_{,j}^{k} U_{k,i}^{(n)} \Big) \end{gathered} \tag{2.38}$$

where F_e is the number of degrees of freedom in each element, $U_i^{(n)}$ denote the shape functions and $D_{(n)}$ are the nodal displacements.

The finite element method is now applied on eq. (2.30) by discretizing the expression through division of the volume V into K elements (subvolumes) as was described earlier and presented in eq. (2.37). Substituting eq. (2.38) into eq. (2.30) and using the shape-functions $U_i^{(n)}$ the discretised form of the dynamic principle of virtual work becomes

$$\sum_{k=1}^{K} \Big(- P_{(m)}^{int.} \Big)_{(k)} = \sum_{k=1}^{K} \Big(P_{(m)}^{ext.} \Big)_{(k)} - \sum_{k=1}^{K} \Big(\mathcal{M}_{(mn)} \Big)_{(k)} \frac{\partial^2 (D_{(n)})_{(k)}}{\partial t^2} \tag{2.39}$$

The nodal force vectors on each element are, due to internal stresses, written as

$$\Big(- P_{(m)}^{int.} \Big)_{(k)} = \int_{V_{(k)}} \tau^{ij} E_{ij}^{(m)} dV \tag{2.40}$$

Similarly the nodal force vectors, due to external loads, are

$$\Big(P_{(m)}^{ext.} \Big)_{(k)} = \int_{S_{(k)}} T^i U_i^{(m)} dS \tag{2.41}$$

and the element mass matrix is discretised into

$$\Big(\mathcal{M}_{(mn)} \Big)_{(k)} = \int_{V_{(k)}} \rho U_{(n)}^i U_i^{(m)} dV \tag{2.42}$$

Here, the shape functions $U_i^{(n)}$ and the corresponding $E_{ij}^{(n)}$ are time independent while the nodal displacements $D_{(n)}(t)$ are functions of time.

In order to sum the equation system, eq. (2.39), over the elements forming the total volume V a renumbering from the element degrees of freedom n within element number k to the corresponding global degrees of freedom $N = N(n,k)$ is carried out. Thereby, the discretised version of the dynamic principle of virtual work, eq. (2.30), is achieved

$$\sum_{N=1}^{F} \mathcal{M}_{(MN)} \frac{\partial^2 D_{(N)}}{\partial t^2} = P_{(M)}^{ext.} + P_{(M)}^{int.} = P_{(M)} \quad \text{for} \quad M = 1, 2, ...F \tag{2.43}$$

where F is the global number of degrees of freedom. In order to avoid the requirement of an equation solver and to save calculation time the mass matrix is further lumped into a diagonal matrix. Here, the diagonal terms in the lumped matrix are found from the lokal diagonal terms in eq. (2.42) scaled with one constant factor so that their total sum is the mass of the element. This is also called HRZ–lumping.

With a lumped mass matrix the equations (2.43) decouple completely so that the equations of motions take the form

$$\sum_{N=1}^{F} M_{(N)} \frac{\partial^2 D_{(N)}}{\partial t^2} = P_{(N)} \quad \text{for} \quad N = 1, 2, ...F \tag{2.44}$$

where $M_{(N)}$ denotes the mass corresponding to the global degree of freedom N.

In papers [P1]-[P2] $3 \times 3 \times 3$ Gauss points are needed in order to integrate the three dimentional mass matrix (2.42) and $2 \times 2 \times 2$ Gauss points are used for the integration of the force term (2.40). Considering plane strain as in [P3] 3×3 and 2×2 integration points are sufficient to integrate the mass matrix and the force term respectively. The extra Gauss point needed for each dimension in carrying out the integration of the mass matrix are required in order to achieve full precision since some of the polynomials to be integrated in eq. (2.42) are of fourth order. The fourth order polynomials arise from eq. (2.42) due the second order shape functions chosen and they can only be precisely integrated when at least three Gauss points for each dimension are used.

When the nodal accelerations $\partial^2 D_{(N)}/\partial t^2$ are computed from eq. (2.44) they must be integrated over time to obtain the nodal displacements $D_{(N)}$. Time integration is carried out using the Newmark β–method with $\beta = 0$ and $\gamma = 0.5$ (Belytschko et al. (1976)). That is

$$U_{n+1} = U_n + \Delta t V_n + \frac{1}{2}(\Delta t)^2 \frac{\partial V_n}{\partial t} \tag{2.45}$$

$$\frac{\partial V_{n+1}}{\partial t} = M^{-1} P_{n+1} \tag{2.46}$$

$$V_{n+1} = V_n + \frac{1}{2}\Delta t \left(\frac{\partial V_n}{\partial t} + \frac{\partial V_{n+1}}{\partial t} \right) \tag{2.47}$$

Here, U denotes the displacement, V denotes the velocity, P is the force, M is the mass and the time step $\Delta t = t_{n+1} - t_n$. The subscripts n and $n+1$ refer to quantities calculated

at t_n and t_{n+1} respectively. In case of low loading rates inertia has pratically no effect and the computations could have been carried out applying a static solution. However, in cases where a static solution would have been sufficient, the dynamic principle of virtual work eq. (2.30) is implemented for numerical convenience.

When λ_c in eq. (2.27) approaches the limit stretch $\lambda_{max} = \sqrt{N}$, the hardening rate given by the increased network stiffness grows very large which effectively suppresses all further plastic flow. Thus, the results are only affected slightly as all viscoplastic flow is disabled through $\dot{\gamma}_p = 0$ when λ_c exceeds $r_\lambda \lambda_{max}$. This was also done by Lai and Van der Giessen (1997) so that the instantaneous response becomes purely elastic at this stage. If the cut off r_λ was not implemented the calculations would turn unstable.

2.2 Constitutive relations with back stress formulation

In the model to be described subsequently, the nonlinear effects are ignored and the elastic part of the response is assumed to be governed by a linear hypoelastic relation as introduced by Wu and Van der Giessen (1996). A clear distinction between the Cauchy stress $\boldsymbol{\sigma}$ and the Kirchhoff stress $\boldsymbol{\tau}$ has been taken into consideration opposite to what is presumed in Tvergaard and Needleman (2008) requiring small elastic strains and incompressible plastic deformations to prevail. The numerical program was originally developed for the analyses performed and discussed by Tvergaard and Needleman (2008). The present model is applied in the papers [P1] and [P2].

2.2.1 Material model

The rate of deformation tensor $\boldsymbol{D}$ defined in eq. (2.2) is separated into an elastic and a plastic contribution

$$\boldsymbol{D} = \boldsymbol{D}^e + \boldsymbol{D}^p \tag{2.48}$$

with

$$\boldsymbol{D}^e = \boldsymbol{L}^{-1} \cdot \hat{\boldsymbol{\sigma}} \qquad , \qquad \boldsymbol{D}^p = \dot{\gamma}^p \boldsymbol{p} \tag{2.49}$$

where $\boldsymbol{L}$ is the isotropic tensor of moduli that contains the elastic constants Young's modulus E and Poisson's ratio ν.

Substituting eq. (2.49) into eq. (2.48) and isolating the Jauman rate of $\boldsymbol{\sigma}$ gives

$$\hat{\boldsymbol{\sigma}} = \boldsymbol{L} : \boldsymbol{D} - \dot{\gamma}^p \boldsymbol{P} \tag{2.50}$$

with $\boldsymbol{P} = \boldsymbol{L} : \boldsymbol{p}$ and $\dot{\gamma}^p$ specified in eq. (2.13). In Cartesian tensor notation $P^{ij} = L^{ijkl} p_{kl}$.

Principally the Jauman rate of the stress $\boldsymbol{\sigma}$ can now be calculated to update the stress state, but the calculations would demand very small time steps to ensure accuracy and to prevent the analysis from turning unstabile. Therefore, in Wu and Van der Giessen (1996) a tangent rate approach (Peirce et al. (1984)) is used in order to increase the very small time steps of eq. (2.50) so that

$$\hat{\boldsymbol{\sigma}} = \boldsymbol{L}^{tan} : \boldsymbol{D} - \boldsymbol{P}^{tan} \tag{2.51}$$

where

$$\boldsymbol{L}^{tan} = \boldsymbol{L} - H\boldsymbol{P} \otimes \boldsymbol{P} \qquad , \qquad \boldsymbol{P}^{tan} = \frac{\dot{\gamma}^p(t)}{1+\xi}\boldsymbol{P} \tag{2.52}$$

and

$$\xi = g\theta\Delta t\frac{\partial\dot{\gamma}^p}{\partial\tau} \qquad , \qquad H = \frac{\xi}{\sqrt{2}g(1+\xi)} \tag{2.53}$$

with $\dot{\gamma}^p$ to be calculated according to eq. (2.13). The quantity θ is a parameter of the numerical procedure, Δt is the magnitude of the time step and in Cartesian tensor notation $L^{tan} = L^{ijkl} - HP^{ij}P^{kl}$. Eq. (2.50) is now replaced by eq. (2.51), (2.52) and (2.53) that altogether are used directly to update the stress state. The contravariant components τ^{ij} of Kirchhoff stress needed to solve the dynamic principle of virtuel work, eq. (2.30), are found from the convected rates of Kirchhoff stresses $\dot{\tau}^{ij}$ that are calculated from (Hutchinson (1973))

$$\dot{\tau}^{ij} = \hat{\tau}^{ij} - G^{ik}\tau^{jl}\dot{\eta}_{kl} - G^{jk}\tau^{il}\dot{\eta}_{kl} \tag{2.54}$$

The stress tensor $\hat{\tau}^{ij}$ is obtained from $\hat{\sigma}^{ij}$ in eq. (2.51) using the kinematical relation eq. (2.33) and subsequently the stresses τ^{ij} are updated from $\dot{\tau}^{ij}$. The updating procedure of the stress state presented in (2.54) is somewhat different from that of Wu and Van der Giessen (1996) since the implementation of the model in the present thesis is total Lagrangian whereas the version of Wu and Van der Giessen (1996) is based on an updated Lagrangian implementation of the model.

The hardness s is taken to develop according to eq. (2.17) as also was implemented in the previous model described in section 2.1.1 in order to introduce plastic softening after initial purely elastic deformation. Similar to eq. (2.12) the rate of plastic deformation in eq. (2.49) is given as a function of a normalized deviatoric stress $\boldsymbol{p}$ though here it is applied with the change that

$$\boldsymbol{p} = \frac{\boldsymbol{\sigma}' - \boldsymbol{b}'}{\sqrt{2}\tau} \qquad \tau = \sqrt{\frac{1}{2}(\boldsymbol{\sigma}' - \boldsymbol{b}') : (\boldsymbol{\sigma}' - \boldsymbol{b}')} \tag{2.55}$$

where the backstress b formulation for the eight chain model is

$$\boldsymbol{b} = \frac{C_R}{3}\frac{\sqrt{N}}{\lambda_c}\beta_c\boldsymbol{B} \qquad \lambda_c^2 = \frac{1}{3}\mathrm{tr}\boldsymbol{B} \tag{2.56}$$

with $\boldsymbol{B} = \boldsymbol{F}\boldsymbol{F}^T$, β_c defined previously in eq. (2.27) now using the λ_c stated above. The backstress relation eq. (2.56) enforces the dramatic stress upturn observed at large strains for the stress-strain response as was the case for eq. (2.26) in section 2.1.1. The expressions of eq. (2.56) and eq. (2.26) are seen to be somewhat similar og they both include the Langevin spring that introduces the stiffness hardening required.

The quantity g in eq. (2.53) is defined by

$$g = \frac{1}{\sqrt{(2)}}\left[\frac{E}{1+\nu} + \boldsymbol{p} : \boldsymbol{R}' : \boldsymbol{p}\right] \tag{2.57}$$

where the contravariant components of the tensor $\boldsymbol{R}'$ are given by

$$R'^{ijkl} = R^{ijkl} - \frac{1}{3} G_{mn} R^{mnkl} G^{ij} \tag{2.58}$$

Here, G_{mn} and G^{ij} are respectively the covariant and the contravariant metric tensors associated with the current frame, see last term defined in eq. (2.34), and R^{ijkl} is calculated from

$$R^{ijkl} = \hat{R}^{ijkl} + \frac{1}{2}\left[G^{ki}b^{lj} + G^{li}b^{kj} + G^{lj}b^{ik} + G^{kj}b^{il}\right] \tag{2.59}$$

with

$$\hat{R}^{ijkl} = \frac{C_R}{3}\sqrt{N}\left[\left(\frac{\chi_c}{\sqrt{N}} - \frac{\beta_c}{\lambda_c}\right)\frac{B^{ij}B^{kl}}{G^{mn}B_{mn}}\right] \qquad \chi_c = \frac{\beta_c^2}{1 - \beta_c^2\,\mathrm{csch}^2\beta_c} \tag{2.60}$$

Finally the plastic strain $\gamma^p = \gamma^p + \dot{\gamma}^p_{com}\Delta t$ is updated from the rate tangent relation

$$\dot{\gamma}^p_{com} = \frac{\dot{\gamma}^p(t)}{(1+\xi)} + \frac{\sqrt{2}E\xi}{2g(1+\xi)(1+\nu)}\boldsymbol{p} : \boldsymbol{D} \tag{2.61}$$

where $\dot{\gamma}^p(t)$ is the value of $\dot{\gamma}^p$ computed from eq. (2.13) at time t and $\dot{\gamma}^p_{com}$ is a linear combination of the values of $\dot{\gamma}^p(t)$ and $\dot{\gamma}^p(t+\Delta t)$ calculated from eq. (2.13).

The numerical formulation is similar to that of section 2.1.2, but considering the present constitutive model with back stress formulation the time step Δt is controlled so that the plastic strain increment $\dot{\gamma}_p\Delta t$ never exceeds a specified value $\Delta\gamma$ which is generally enforced to $\Delta\gamma = 0.000004$.

Chapter 3
Summary of results

This chapter presents a summary of the main results obtained and discussed in the papers included at the end of the thesis. In the respective papers a more detailed description of the individual cases, background and results can be found.

Section 3.1 contains the essential results from the paper [P1] where a plane strain polymer tube is analysed with respect to neck initiation and neck propagation along the tube wall under dynamically increasing internal pressure.

In section 3.2 focus is on bulge formation and necking in three dimensional polymer tubes under dynamic expansion as presented in paper [P2]. Expansion caused by the enclosed volume increasing linearly with respect to time is compared to expansion under pressure increasing linearly with time. The results to be shown are from the paper [P2], but two extra plots pertaining to the subject analysed in this paper are presented as well.

Shear zone development between overlapping fibers is the subject of the third paper [P3] discussed in section 3.3. The shear zone is shown to depend on fiber spacing, fiber thickness and on the ratio of the elongation strain and the transverse strain.

The polymer used is representative of an amorphous glassy polymer such as polycarbonate (PC). Young's modulus is $E = 1814.6$ MPa, $\nu = 0.38$, density $\rho = 1300$ kg/m^3, temperature $T = 298$ K. More material parameters are $\Delta G = 0.374 \cdot 10^{-18}$ J, $\dot{\gamma}_0 = 0.894 \cdot 10^4$ s^{-1}, $m = 0.20$, $C_r = 12.6$ MPa, $N = 2.30$ and the parameters $\alpha = 0.08$, $s_0 = 81.65$ MPa, $s_{ss} = 22.71$ MPa, $h = 50.0$ MPa. Same parameters were used by Tvergaard and Needleman (2008) and they are the ones chosen for the numerical calculations in [P1], [P2] and [P3] as well (see eq. (2.13), eq. (2.16), eq. (2.17), eq. (2.18), eq. (2.26), eq. (2.27) and eq. (2.56), eq. (2.57), eq. (2.60), eq. (2.61) used for the material models presented in section 2.1 and 2.2 respectively). Figure 3.1 shows the uniaxial stress-strain curves in tension and compression for the material parameters chosen with the true strain being logarithmic. The fitting of the compression responses so that they qualitatively represent the experimental compression curves for PC given in Mulliken and Boyce (2006) is carried out by the author of this thesis. Polymer characteristics such as a roll over from purely linear elastic deformation to plastic softening leaving a sharp stress peak and a significant network hardening occurring at large strains are observed from the uniaxial stress-strain curves in Figure 3.1.

Furthermore, in section 3.4 extra results for another polymer than the one used for papers [P1]-[P3] are shown and interesting observations regarding necking mechanisms are made.

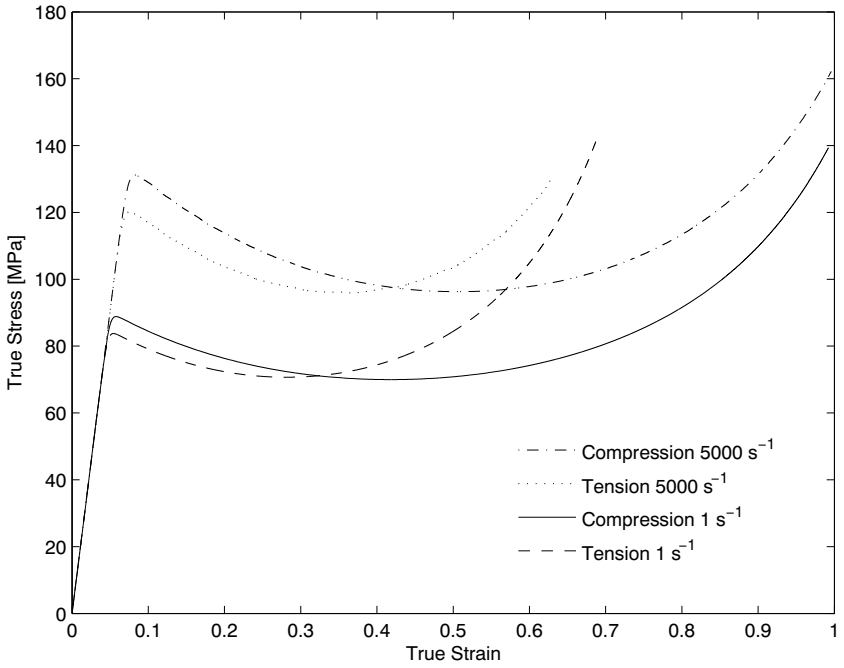

Figure 3.1 Stress-strain curves for uniaxial tension and uniaxial compression at the rates 5000 s^{-1} and 1 s^{-1} for the material parameters used in the present thesis. The true strain is logarithmic.

3.1 Two dimensional neck development in polymer tubes under dynamic expansion

Several studies of circumferential neck development for metal rings expanded rapidly have been carried out by Niordson (1965), Han and Tvergaard (1995), Tŭgcu (1996) and Sørensen and Freund (2000) showing that the necks follow a short wave length pattern around the circumference and form through localization. This is also lately emphasised experimentally by Zhang and Ravi-Chandar (2006). Similarly in paper [P1] plane strain polymer tubes are investigated numerically with respect to neck initiation and neck formation along the circumference. A switch from neck localization to neck propagation is observed which is in agreement with experiments performed by G'Sell and Jonas (1979) and Marquez-Lucero et al. (1989) revealing neck propagation to be a polymer characteristic. The tube is expanded rapidly under an internal applied pressure that is taken to increase linearly as a function of time. It is shown that also a plane strain tube consisting of a thermoplast polymer may prefer to neck at several locations following a short wavelength pattern. Moreover, the neck development is seen to depend on the rate of deformation and a case of network locking is presented.

An internal pressure p that increases linearly as a function of time t is imposed on the inner surface of the tubes through eq. (2.30) in chapter 2 in order to make them expand.

The corresponding components of the nominal traction vector T^i on the reference base vectors are defined by

$$T^i = -p\alpha^{ir}n_r, \qquad \text{for} \qquad \{(y^1)^2 + (y^2)^2\}^{1/2} = R_0 - h_0/2 + \Delta h_0 \tag{3.1}$$

where the tensor α^{ir} is specified by

$$\alpha^{ir} = \frac{1}{2}\varepsilon^{ijk}\varepsilon^{lmr}(g_{jl} + u_{j,l})(g_{km} + u_{k,m}) \tag{3.2}$$

As was introduced by (Sewell, 1965) ε^{ijk} is the alternating tensor and n_r is the normal to the inner surface in the reference coordinate system. The geometry of the tube is specified by the initial mean thickness h_0 and the initial mean radius R_0 as given in Figure 3.2.

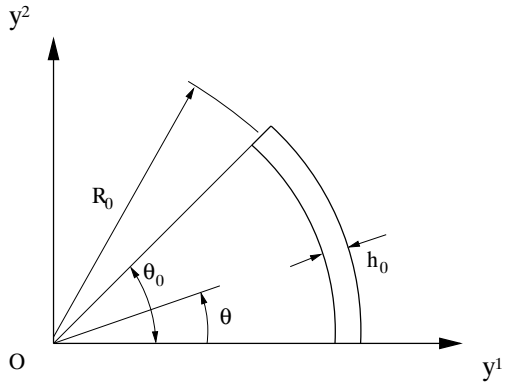

Figure 3.2 A (y^1,y^2)-plane segment of the tube specimen defined by the initial mean radius R_0, the initial mean thickness h_0 and the angle θ_0. Plane strain is assumed to prevail in the axial direction perpendicular to the (y^1,y^2)-plane.

To trigger the onset of necking along the tube wall an initial sinusoidal thickness inhomogeneity Δh_0 which is similar to that used by Han and Tvergaard (1995) is applied on both the inner and the outer surfaces of the tube so that the initial wall thickness is $h_0 - 2\Delta h_0$. The initial thickness imperfection Δh_0 is given by

$$\Delta h_0 = -h_0\xi_n \cos\left(\frac{n\pi\theta}{\theta_0}\right) \tag{3.3}$$

where θ is the angle defined in Figure 3.2, ξ_n is the amplitude of the thickness imperfection and n is the wave number. Symmetry about the planes $\theta = 0$ and $\theta = \pi/2$ (see Figure 3.2) is assumed and so analyses need only be carried out for a 90° segment of the tube circumference and not for the entire specimen considered. Therefore, the angle constant $\theta_0 = \pi/2$ is chosen and symmetry boundary conditions are applied which reduces the large calculation time needed to solve the full three dimensional problem. Moreover, the numerical calculations are only carried out for plane strain prevailing in the axial

direction y^3 of the tubes so all displacements in the direction of y^3 are enforced to zero and one element in the third direction is sufficient.

All the thin tubes to be analysed subsequently are discretised into 320 three dimensional 20 noded isoparametric elements with 2 elements through the thickness and 160 along the circumference. The extent of necking is measured in terms of the interior volume change ΔV inside the tube normalized by the initial interior volume V_0 or by the average logarithmic hoop strain ε_{av} that is found on the inner surface of the tube as

$$\varepsilon_{\text{av}} = \ln\left(\frac{R_i}{R_{i0}}\right) \tag{3.4}$$

where R_{i0} is initial inner radius of the perfect tube without the imperfection and R_i is the average inner radius

$$R_i = \sqrt{\frac{V}{\pi L}} \tag{3.5}$$

based on current volume V and on the assumption of the cross section of the tube to remain circular under deformation. Here, L is the length of the tube.

In Figure 3.3 the contours of effective plastic strain γ^p are shown in the deformed

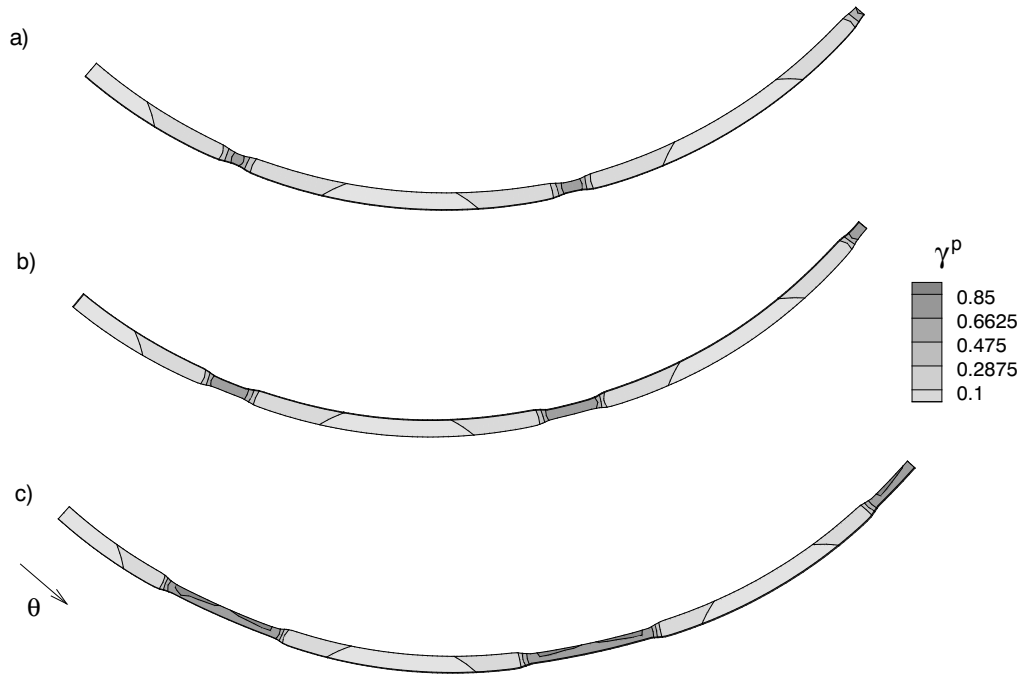

Figure 3.3 Plastic strain contours γ^p of the deformed thin walled tube with $h_0 = 0.002$ m, $h_0/R_0 = 0.0392$, $n = 5$ and $\xi_5 = 0.001$. The applied pressure rate is $\dot{p} = 411.7$ MPa/s and θ increases from 0° to 90° in the direction shown. The average logarithmic hoop strain, ε_{av}, for the situations shown above is: (a) $\varepsilon_{\text{av}} = 0.160$ (b) $\varepsilon_{\text{av}} = 0.194$ (c) $\varepsilon_{\text{av}} = 0.286$.

state for the thin walled tube with the initial wall thickness $h_0 = 0.002$ m and the ratio

$h_0/R_0 = 0.0392$. The imposed thickness imperfection is chosen to have the wave number $n = 5$ and the amplitude $\xi_5 = 0.001$ and the internal pressure is applied to increase linearly with respect to time at a rate of $\dot{p} = 411.7$ MPa/s. Initially at all thin point locations necks are observed to localize and subsequently thin down as the interior pressure grows and the tube expands. In agreement with experiments carried out by G'Sell and Jonas (1979) and Marquez-Lucero et al. (1989) the mode of deformation is seen to switch to neck propagation after the necks have thinned somewhat down. This is a polymer characteristic whereas in case of circumferential necking in metal rings the localized necks continue to thin down until fragmentation of the ring interrupts any further deformation. The explanation for the switch to neck propagation is that the material in the propagating necks have reached a high network stiffness as a consequence of the stretch in the necks approaching the material dependent limit stretch, see eq. (2.26), eq. (2.27) and eq. (2.28). It is during the tube expansion in Figure 3.3 noticed that necks form at initial thin points only and not elsewhere along the circumference.

The responses of the thin walled tube analysed in Figure 3.3 but expanded under the different pressure rates $\dot{p} = 41.17$ MPa/s, $\dot{p} = 411.7$ MPa/s and $\dot{p} = 4117$ MPa/s respectively are illustrated in Figure 3.4. First in Figure 3.4a, the normalized applied pressure is

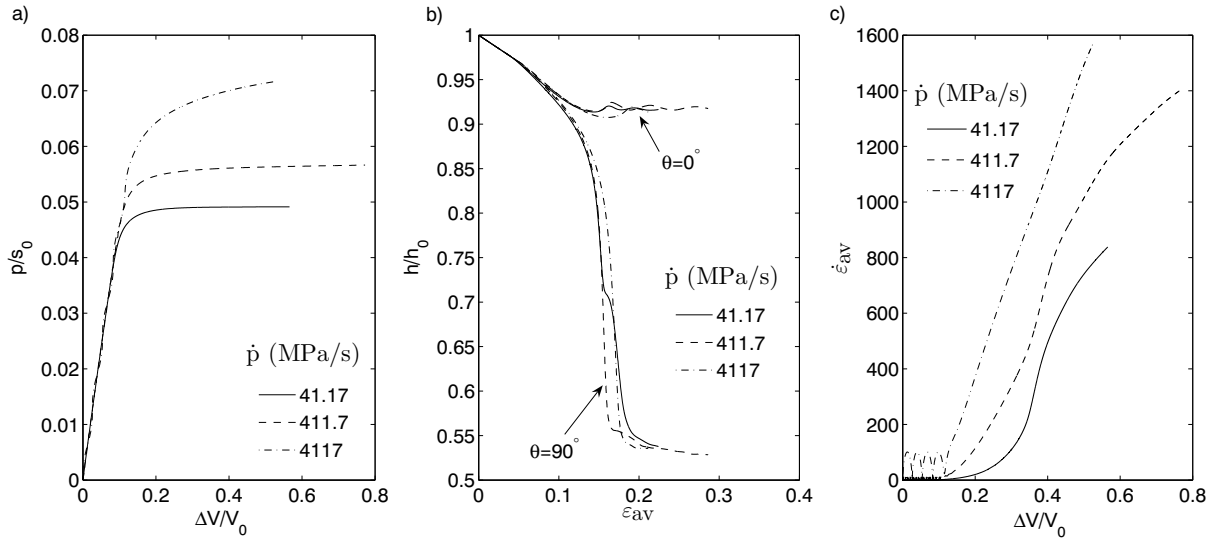

Figure 3.4 Curves for a thin walled tube with $h_0 = 0.002$ m, $h_0/R_0 = 0.0392$, $n = 5$ and $\xi_5 = 0.001$ under different rates of pressure. (a) Normalized internal pressure, p/s_0, with respect to normalized internal volume change of the tube, $\Delta V/V_0$. (b) Normalized wall thickness at 0° and at 90° with respect to average hoop strain ε_{av}, see eq. (3.10). (c) Average hoop strain rate, $\dot{\varepsilon}_{\text{av}}$, with respect to the normalized internal volume change of the tube, $\Delta V/V_0$.

shown to increase approximately linearly with interior volume during elastic deformation, but as plastic deformation initiates the volume suddenly grows rapidly causing the tube to expand so dramatically that the pressure appears nearly constant in comparison even though it increases with time. Not surprisingly, higher pressure rate results in a higher

pressure level in the nonlinear regime of deformation. Also the average hoop strain rate $\dot{\varepsilon}_{\text{av}}$ increases with pressure rate, see Figure 3.4c.

Figure 3.4b presents the normalized wall thickness evolution at the thin point location $\theta = 90^\circ$ where a neck forms and at the thick point location $\theta = 0^\circ$ where no neck forms respectively. Due to the Poisson effect, initially the wall thickness at 0° reduces somewhat as the tube expands until necks begin to develop elsewhere around the circumference. However, as necks form the wall thickness at 0° remains essentially constant with some oscillations on the response that die out as the tube expands and the necks elsewhere propagate. The oscillations emerge as a consequence of the neck development elsewhere along the circumference. The thickness decrease at 90° indicates that a neck has localized at this position and that it is thinning down as was observed already in Figure 3.3. As the deformation mode switches to neck propagation the thickness remains approximately constant. Oscillations appear on the thickness curves due to more dominant necks developing elsewhere along the tube circumference.

From Figure 3.4b the development of necks is discovered to be strain rate sentitive. Particularly for the pressure rate $\dot{p} = 41.17$ MPa/s a bump emerges on the thickness response which is in agreement with the numerical analyses carried out by the author of this thesis showing the neck next to the one at 90° to be the clearly most dominant neck throughout the expansion even though the imperfection amplitude is the same at all three thin point locations. With increased loading rate the necks tend to develop into a more equal size so that at $\dot{p} = 4117$ MPa/s the necks are essentially similar in size. This is also observed in Figure 3.4b where no oscillations appear on the thickness response for $\dot{p} = 4117$ MPa/s.

Figure 3.5 illustrates a situation identical to that in Figure 3.3 and 3.4, but with the difference that the imperfection is now defined by $n = 1$ and $\xi_1 = 0.001$ so that only one thin point is added on the quarter of the tube analysed. The corresponding responses are presented in Figure 3.6. Compared to the case in Figure 3.3 and 3.4 the necking pattern in Figure 3.5 is nearly not noticeable and the extent of necking and the necking behaviour in general are in Figure 3.6 seen to be very strain and loading rate dependent. In paper [P1] a case where 5 thin points ($n = 9$ and $\xi_9 = 0.001$) are imposed on the quarter of the tube is analysed showing a fully developed necking pattern. This confirms the observations discussed previously emphasising that the necking along the circumference of a polymer tube may prefer to neck following a short wave length mode as was the case for metal tubes, but with the major difference the necks along the polymer tube will localize much less when a sufficient number of thin points is not present. An explanation for this phenomenon is that the polymer may prefer to neck at thin point locations only due to the main characteristics of the uniaxial stress-strain response resulting in the necks to get locked at their respective positions during the significant softening that follows the sharp stress peak initiating the neck development. Once some points along the circumference have passed the stress peak initiating necking, it may seem less easy for the material to initiate extra necks than the ones just formed.

Considering a thick tube applied the same thickness imperfection as the one for the situation in Figure 3.5 and 3.6 plastic strain contours appear as shown in Figure 3.7 de-

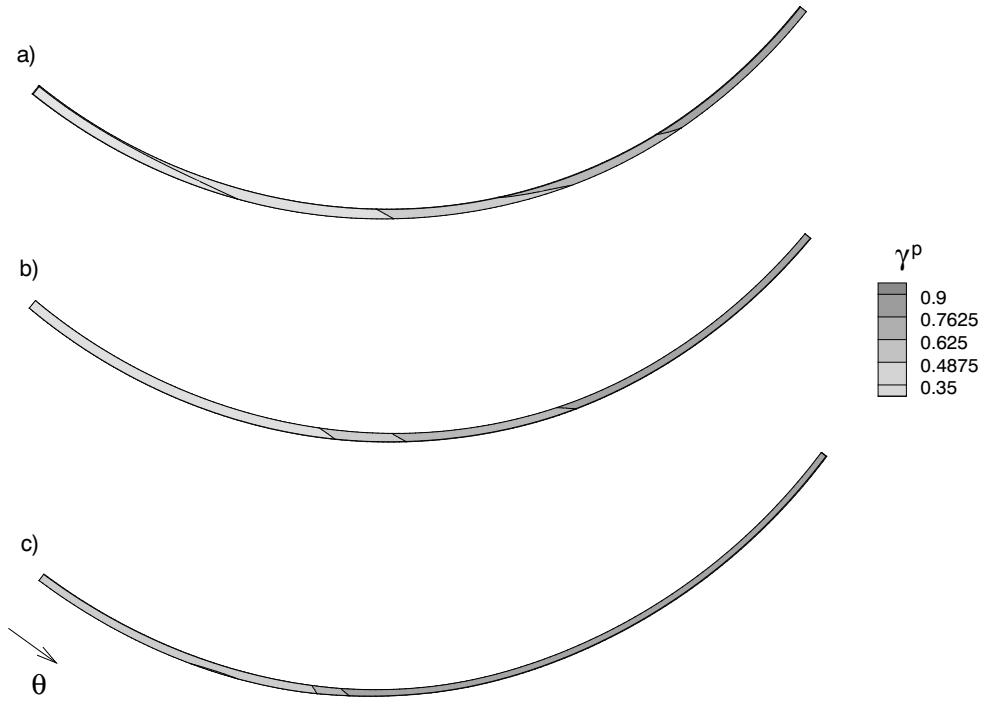

Figure 3.5 Plastic strain contours γ^p of the deformed thin walled tube with $h_0 = 0.002$ m, $h_0/R_0 = 0.0392$, $n = 1$ and $\xi_1 = 0.001$. The applied pressure rate is $\dot{p} = 411.7$ MPa/s and θ increases from 0° to 90° in the direction shown. The average logarithmic hoop strain, ε_{av}, for the situations shown above is: (a) $\varepsilon_{\text{av}} = 0.449$ (b) $\varepsilon_{\text{av}} = 0.505$ (c) $\varepsilon_{\text{av}} = 0.624$.

picting the deformed state of the tube and the corresponding responses are seen in Figure 3.8. The tube in Figure 3.7 is discretised into 720 elements so that it has 6 elements through the thickness and 120 along the circumference and the pressure is imposed at a rate of $\dot{p} = 823.4$ MPa/s. Now for the thicker tube in Figure 3.7, the neck localization and neck propagation are clearly visible opposite to what was observed for the thinner tube in Figure 3.5. However, the wall thickness at 0° location of the thick tube decays a little instead of remaing constant during the neck propagation at 90°, as can be seen from Figure 3.8b. When more thin points are added along the quarter of the thick tube, as has been done in paper [P1], the necks localize, but since the thickness at 0° does not decay from $h/h_0 = 0.95$ the thickness remains essentially constant when at first the Poisson effect is overcome. Thus, considering a thick tube the extent of localization is a little larger in case of more thin points applied along the circumference and this reveals that some trace to the phenomenon of short wave length necking previously found for the thin tube is kept.

Next, the loading of the tube illustrated in Figure 3.3 and Figure 3.4 is continued for a longer time so that a larger hoop strain is obtained and the appertaining curves are shown in Figure 3.9. At the cut-off value $r_\lambda = 0.93$ (see section 2.1.2) plasticity is disabled since the stretching at this stage has grown so large that the network stiffness dramatically increases which effectively oppresses continued plastic flow. The large stretching occurs as the necks have spread to the entire tube. Therefore as the network hardened tube is further

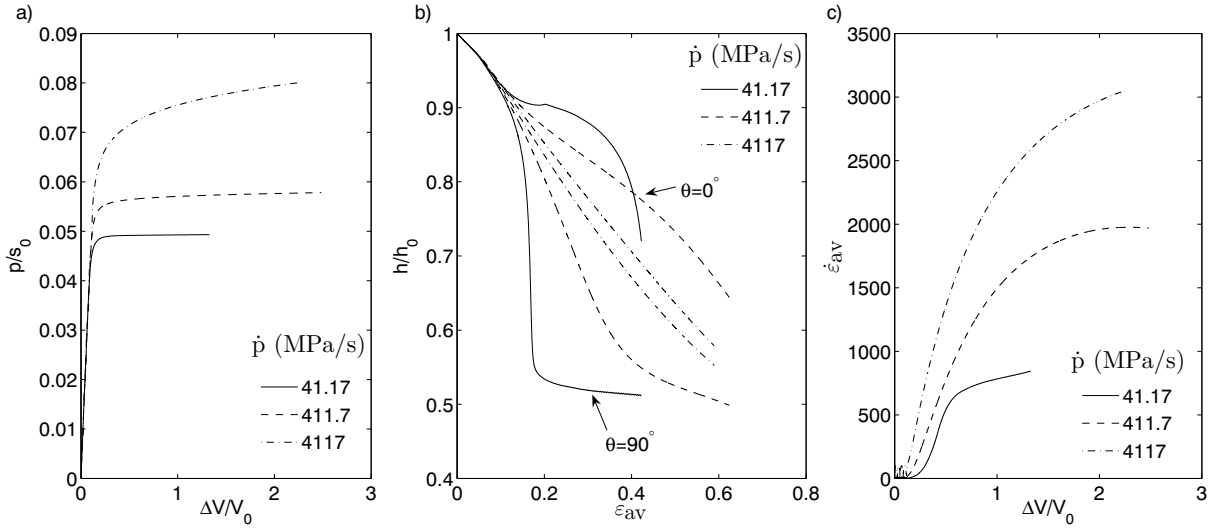

Figure 3.6 Curves for a thin walled tube with $h_0 = 0.002$ m, $h_0/R_0 = 0.0392$, $n = 1$ and $\xi_1 = 0.001$ under different rates of pressure. (a) Normalized internal pressure, p/s_0, with respect to normalized internal volume change of the tube, $\Delta V/V_0$. (b) Normalized wall thickness at $0°$ and at $90°$ with respect to average hoop strain ε_{av}, see eq. (3.10). (c) Average hoop strain rate, $\dot{\varepsilon}_{\text{av}}$, with respect to the normalized internal volume change of the tube, $\Delta V/V_0$.

expanded so that the stretching λ_c in eq. (2.27) exceeds $0.93\sqrt{N}$ the material behaviour changes from elastic-plastic back to purely elastic. However, it must be emphasised that modelling the actual network hardening as dependent on initial elastic characteristics only is a somewhat coarse assumption, but it is expected to give a good understanding of the tube behaviour during network hardening.

The sudden dramatic increase in the imposed pressure observed from Figure 3.9a results from network hardening introducing a high stiffness against further expansion of the tube. Also, network hardening causes elastic vibrations in the volume change and in the average hoop strain which is seen in Figure 3.9a and 3.9b respectively as a dynamic mode is taking over. The vibration frequency in Figure 3.9c rely on the hardening behaviour of the polymer material that for this specific case has been changed from elastic-plastic to fully linear elastic. As the necks propagate throughout the entire tube finally the point at $0°$ is reached as can be seen from Figure 3.9b. As the neck propagation passes $0°$ the wall thickness at this point decreases towards the wall thickness at $90°$ and due to network hardening subsequently the dynamic mode takes over introducing vibrations in the wall thickness of the tube as well.

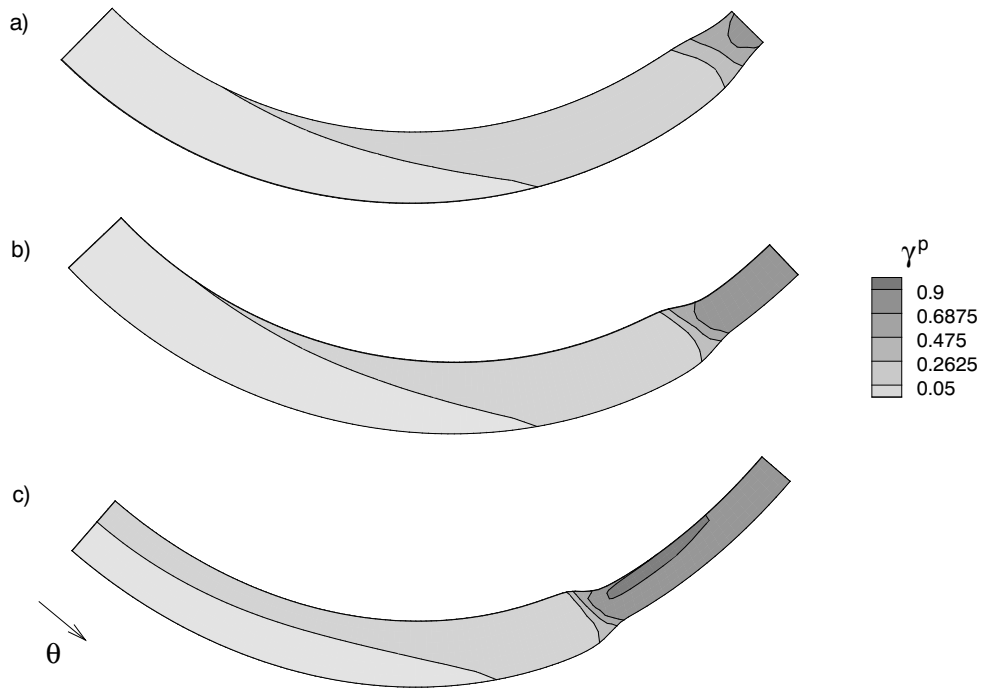

Figure 3.7 Plastic strain contours γ^p of the deformed thick walled tube with $h_0 = 0.01$ m, $h_0/R_0 = 0.182$, $n = 1$ and $\xi_1 = 0.01$. The applied pressure rate is $\dot{p} = 823.4$ MPa/s and θ increases from 0° to 90° in the direction shown. The average logarithmic hoop strain, ε_{av}, is: (a) $\varepsilon_{\text{av}} = 0.133$ (b) $\varepsilon_{\text{av}} = 0.178$ (c) $\varepsilon_{\text{av}} = 0.271$.

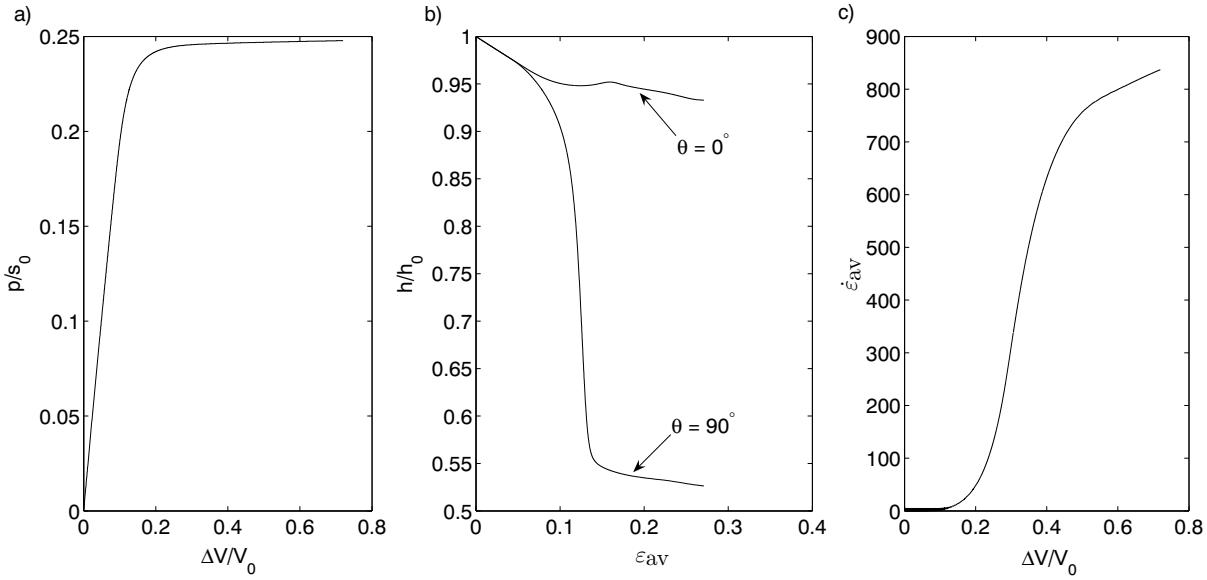

Figure 3.8 Curves of a thick walled tube with $h_0 = 0.01$ m, $h_0/R_0 = 0.182$, $n = 1$, $\xi_1 = 0.01$ under the pressure rate $\dot{p} = 823.4$ MPa/s. (a) Normalized internal pressure, p/s_0, with respect to normalized internal volume change of the tube, $\Delta V/V_0$. (b) Normalized wall thickness at 0° and at 90° with respect to average hoop strain ε_{av}, see eq. (3.10). (c) Average hoop strain rate, $\dot{\varepsilon}_{\text{av}}$, with respect to the normalized internal volume change of the tube, $\Delta V/V_0$.

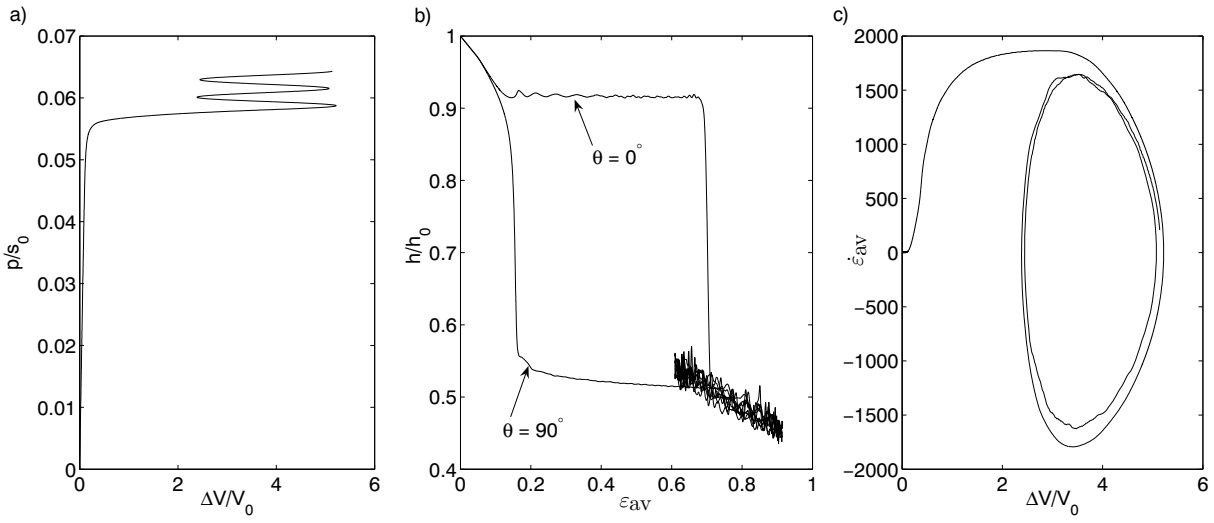

Figure 3.9 Curves for a thin walled tube with $h_0 = 0.002$ m, $h_0/R_0 = 0.0392$, $n = 5$ $\xi_5 = 0.001$, $\dot{p} = 411.7$ MPa/s and a cut-off value $r_\lambda = 0.93$. (a) Normalized internal pressure, p/s_0, with respect to normalized internal volume change of the tube, $\Delta V/V_0$. (b) Normalized wall thickness at 0° and at 90° with respect to average hoop strain ε_{av}, see eq. (3.10). (c) Average hoop strain rate, $\dot{\varepsilon}_{\text{av}}$, with respect to the normalized internal volume change of the tube, $\Delta V/V_0$.

3.2 Three dimensional neck development and bulging in polymer tubes under dynamic expansion

The numerical analyses presented in paper [P1] and previously discussed in section 3.1 do not take three dimensional effects into consideration. In paper [P2] full three dimensional studies of a pressurised long polymer tube are carried out investigating bulge formation and neck development as has been done for metal tubes (Larsson et al. (1982), Tvergaard (1990) and Mikkelsen and Tvergaard (1999)). Necking occurs in the bulge of the polymer tube as was found by Mikkelsen and Tvergaard (1999) for metal tubes, but neck propagation as observed by G'Sell and Jonas (1979), Marquez-Lucero et al. (1989) and investigated in paper [P1] is seen as well. First, the pressure is taken to increase linearly with respect to time as was done in paper [P1], but subsequently the pressure is controlled so that the enclosed volume is to increase linearly with time. The last type of imposed loading is in agreement with experiments where the tube is expanded by pumping an imcompressible fluid into the tube and a pressure maximum is introduced.

Similar to the two dimensional case in section 3.1 also here geometrical imperfections along the tube wall are required in order to trigger the onset of necking and bulging. An internal pressure p is applied on the inner surface of the tubes. The corresponding components T^i are identical to those specified by eq. (3.1) in section 3.1, but they are here applied on the internal surface specified by

$$\{(y^1)^2 + (y^2)^2\}^{1/2} = R_0 + \Delta R_0 - h_0/2 + \Delta h_0 \tag{3.6}$$

where Δh_0 is the thickness inhomogeneity introduced and ΔR_0 is a inhomogeneity imposed on the radius. The initial mean radius R_0 and the initial mean thickness h_0 prescribe the geometry of the tube. Together with the angle θ_0 these parameters specify the segment of the tube shown in Figure 3.10 that is to be analysed numerically (the y^3-axis points into the paper). Again $\theta_0 = \pi/2$ is used with symmetry boundary conditions im-

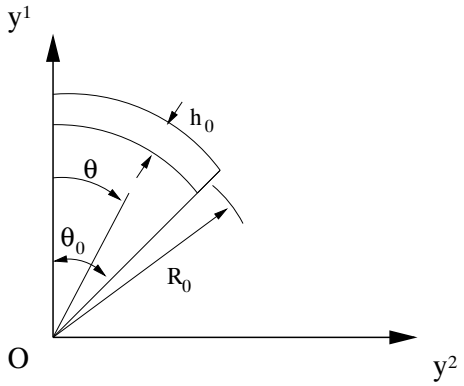

Figure 3.10 A (y^1,y^2)-plane segment of the perfect tube where R_0 is the initial mean radius, h_0 is the initial mean thickness, θ_0 is the angle of the segment chosen and the y^3-axis points into the (y^1,y^2)-plane.

plemented along the planes $\theta = 0$ and $\theta = \pi/2$ so that the total number of degrees of freedom needed to solve the symmetric problems considered are reduced to a minimum. Also symmetry boundary conditions are applied at $y^3 = 0$ so that numerical results need only be carried out for one half of the tube. The half tube has the length L and the length of the entire tube is $2L$ with the bulge forming at the middle of the tube at $y^3 = 0$.

The thickness imperfection Δh_0 introducing necking and the radius imperfection ΔR_0 added to the initial mean radius introducing axisymmetric bulging are respectively defined by

$$\Delta h_0 = -g(y^3) h_0 \xi_n \cos\left(\frac{n\pi\theta}{\theta_0}\right) \tag{3.7}$$

and

$$\Delta R_0 = g(y^3) \xi R_{i0} \tag{3.8}$$

with the cosine dimple function (Hutchinson et al. (1971)) given by

$$g(y^3) = \begin{cases} \frac{1}{2}\left(1 + \cos\left(\frac{\pi y^3}{R_{i0}}\right)\right) & 0 \le y^3 \le R_{i0} \\ 0 & R_{i0} < y^3 \le L \end{cases} \tag{3.9}$$

which ensures that the geometrical imperfections are imposed in the front of the half tube only (where $0 \le y^3 \le R_{i0}$). Here, $R_{i0} = R_0 - h_0/2$ is the initial inner radius of the tube cross section when no imperfection is added. The thickness inhomogeneity Δh_0 is added to the inside and the outside of the tube surface respectively so that the initial wall thickness becomes $h_0 + 2\Delta h_0$ as was the case in section 3.1 whereas the radius inhomogeneity ΔR_0 inciting the axisymmetric bulge is imposed on the initial mean radius R_0.

The results to be shown subsequently are computed for a long thin polymer tubes all specified by an intial wall thickness $h_0 = 0.002$ m, initial mean radius $R_0 = 0.051$ m and entire length $2L = 0.8162$ m though only half length is studied when symmetri conditions are applied. All tubes are discretised into 9180 three dimensional 20 noded isoparametric elements with 60 elements along the circumference, 153 along the length L and 1 element through the thickness. The average logarithmic hoop strain

$$\varepsilon_{\text{av}} = \ln\left(\frac{R_i}{R_{i0}}\right) \qquad \text{for} \qquad y^3 = 0 \tag{3.10}$$

is used to measure the degree of deformation in the bulge region where the average inner radius R_i is found from

$$R_i = \sqrt{\frac{A}{\pi}} \qquad \text{for} \qquad y^3 = 0 \tag{3.11}$$

Here, A is the current inner cross sectional area at $y^3 = 0$.

Figure 3.11 shows the contours of plastic strain for the deformed tube at three levels of deformation as an internal pressure increasing linearly with respect to time is applied.

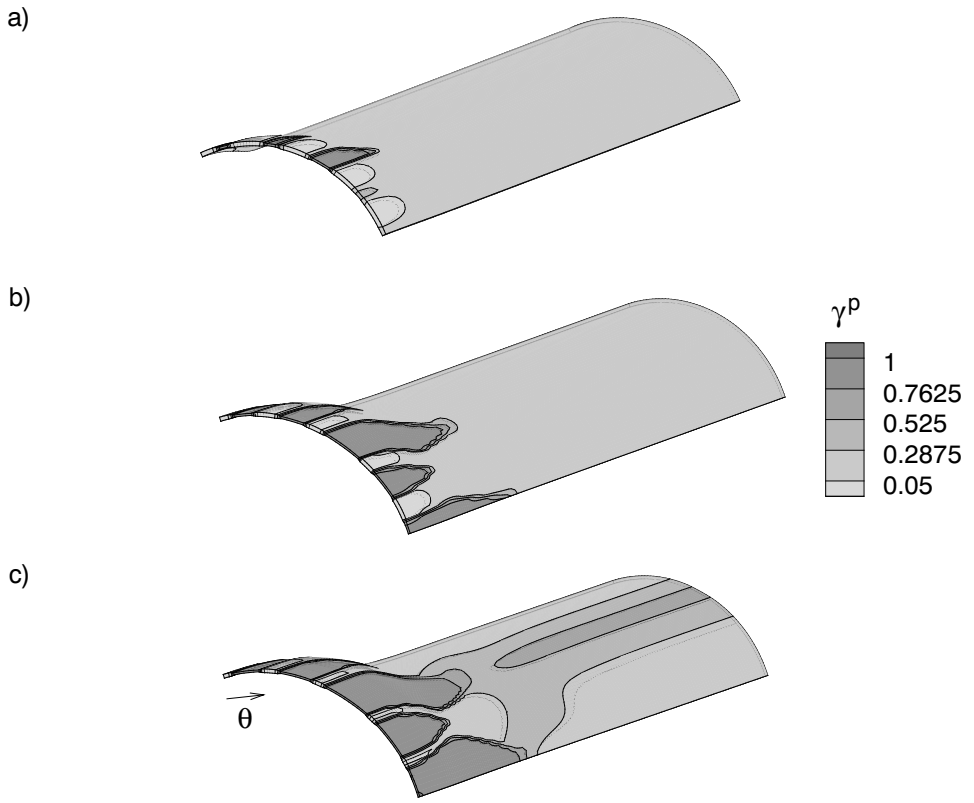

Figure 3.11 Plastic strain contours γ^p of the deformed tube with $h_0 = 0.002$ m, $h_0/R_0 = 0.0392$, $n = 9$, $\xi_9 = 0.01$ and $\xi = 0.01$. The applied pressure increases linearly with time where $\dot{p} = 411.7$ MPa/s and θ increases from 0° to 90° in the direction shown. (a) $V/V_0 = 1.302$ and $\varepsilon_{\text{av}} = 0.217$ (b) $V/V_0 = 1.596$ and $\varepsilon_{\text{av}} = 0.404$ (c) $V/V_0 = 1.996$ and $\varepsilon_{\text{av}} = 0.540$.

The thickness imperfection and the radius imperfection are specified by the wave number $n = 9$, the thickness amplitude $\xi_9 = 0.01$ and the radius amplitude $\xi = 0.01$ respectively. As expected a bulge is seen to develop and it grows largest at $y^3 = 0$ that is the middle of the entire tube. Necks initiate and localize only at the thin points along the circumference and subsequently they propagate both in the circumferencial direction and in the axial direction. Neck propagation is a polymer characteristic and the phenomenon was observed experimentally by G'Sell and Jonas (1979) and Marquez-Lucero et al. (1989). Also, numerical analyses carried out in paper [P1] for plane strain polymer tubes reveal circumferential necks to form and propagate at initiatial thin points along the circumference. The phenomenon of neck propagation was previously clarified in paper [P1] and furthermore discussed in section 3.1.

As the pressure continues to grow at some stage the stress level of plasticity is reached outside the region of initial imperfections and necks will form and propagate rapidly here as well. This is seen to be the case in Figure 3.11c where a neck has developed for $R_{i0} < y^3$ and has started to connect with the necks in the bulge region. If a fracure

criterion, a crazing model for example, was implemented in the constitutive formulations, the tube would inevitably be undergoing fracture at a certain point.

Figure 3.12a illustrates how the the enclosed volume of the tube rapidly increases when plastic deformation takes place in the region of the bulge. This explosive expansion

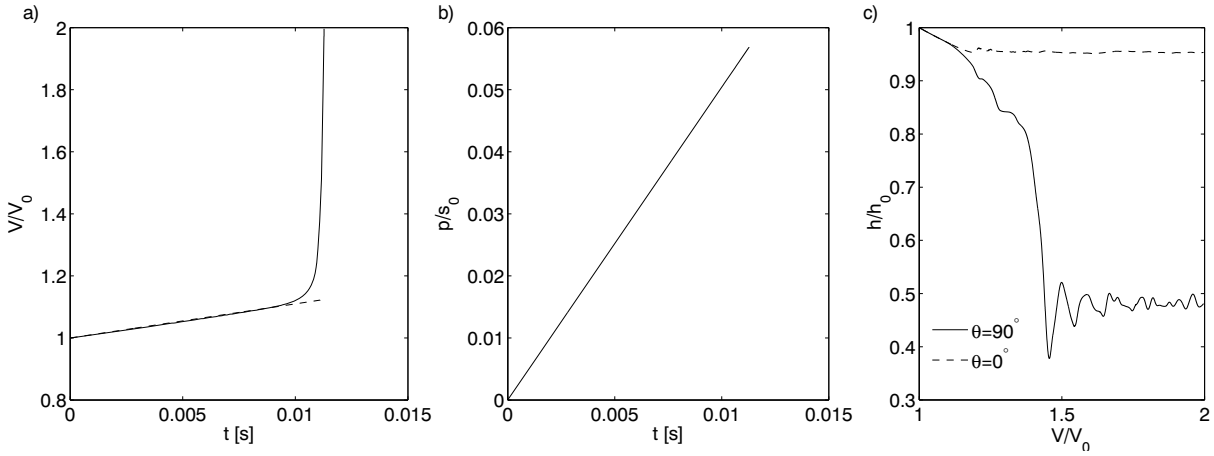

Figure 3.12 Curves for a tube with $h_0 = 0.002$ m, $h_0/R_0 = 0.0392$, $n = 9$, $\xi_9 = 0.01$ and $\xi = 0.01$ under internal pressure increasing linearly as a function of time. (a) Normalized internal volume, V/V_0, with respect to time, t. (b) Normalized internal pressure, p/s_0, with respect to time, t. (c) Normalized wall thickness at $0°$ and at $90°$, for $y^3 = 0$, with respect to V/V_0.

is a consequence of large strain rates introducing a great influence of viscoplastic effects. From analyses of metal rings (and from plane strain polymer tubes in paper [P1]) such rapid expansion is known to minimize the circumferential inertia, but anyway some necks in Figure 3.11 grow to become more dominant in the axial direction of the tube despite the fact that the amplitude of the imperfection is identical at all thin points.

The linearly increasing pressure is illustrated in Figure 3.12b and the change of the wall thickness at the location $\theta = 90°$ where a neck is present and at the location $\theta = 0°$ where no neck is present is pictured in Figure 3.12c. The small thickness reduce at $0°$ is a consequence of the Poisson effect whereas the curve depicting the thickness change at $90°$ decreases as the neck thins down, but after a while it converges towards a constant value as a consequence of the neck propagation. The oscillations on the thickness response arise because more dominant necks develop close to the neck at $90°$. These observations on the thickness responses are similar to those of paper [P1].

In the previous example (and in paper [P1] as presented shortly in section 3.1) the internal pressure is assumed to increase linearly with respect to time, but this may be difficult to carry out experimentally. In experiments, when neck development and particularly bulge formation is studied, the tube is expanded much more slowly by pumping an almost imcompressible fluid into the tube so that the enclosed volume increases linearly with time. Therefore all subsequent results to be presented are produced by controlling the pressure so that the volume-time dependence remains approximately linear also in the plastic regime as was not the case for the previous situation illustrated in Figure 3.12a.

The outcome is expected to be more reliable and show higher agreement with experiments already known and as the plasticity initiates at a slower rate also the bulge and the necks are to form more slowly. Nevertheless, the first applied type of loading where the pressure increases linearly with time is expected to give a reasonable understanding of the behaviour of the long polymer tubes during expansion.

In Figure 3.13 contours of plastic strain for the same deformed tube as the one that

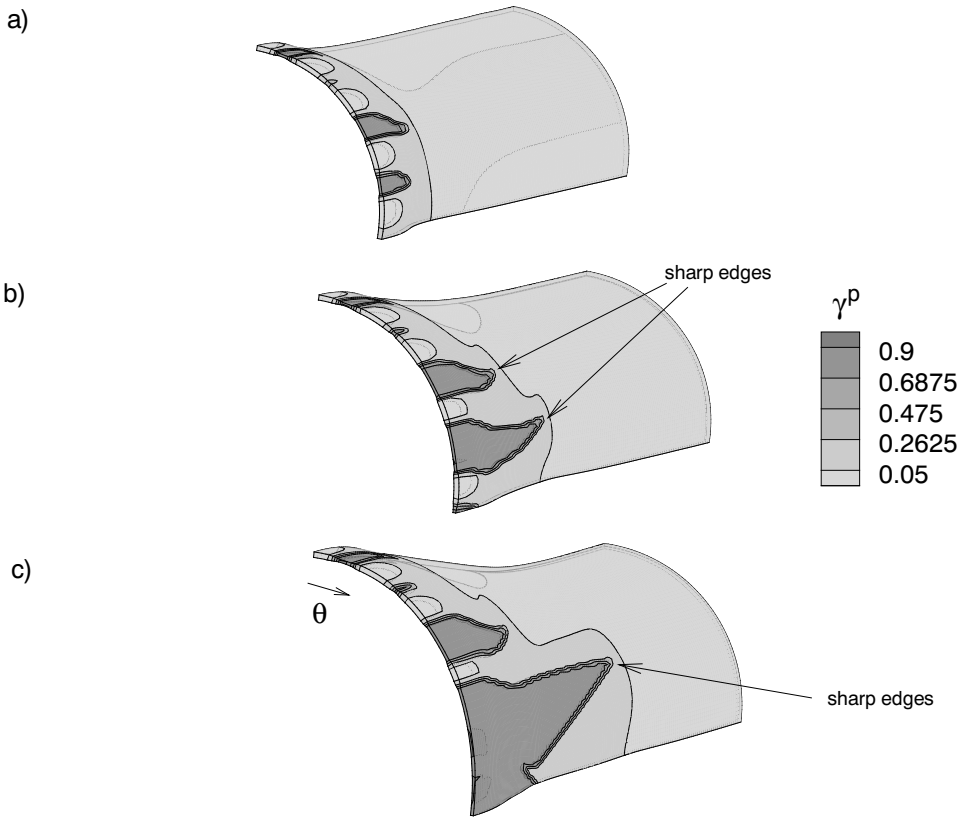

Figure 3.13 Plastic strain contours γ^p of the deformed tube with $h_0 = 0.002$ m $h_0/R_0 = 0.0392$, $n = 9$, $\xi_9 = 0.01$ and $\xi = 0.01$. The applied pressure rate is controlled to give $\dot{V}/V_0 = 11.0$ s^{-1} and θ increases from 0° to 90° in the direction shown. (a) $V/V_0 = 1.209$ and $\varepsilon_{\mathrm{av}} = 0.209$ (b) $V/V_0 = 1.291$ and $\varepsilon_{\mathrm{av}} = 0.286$ (c) $V/V_0 = 1.466$ and $\varepsilon_{\mathrm{av}} = 0.400$.

was studied previously is shown, but here the pressure is controlled so that the volume increases linearly with respect to time. Bulge formation and neck propagation are observed as for the first case, but now some necks are obviously much more dominant than others both axially and circumferentially probably due to a high strain rate dependence as discussed in paper [P1]. As the hoop strain increases, the most dominant necks in the initial stage (Figure 3.13a) are exceeded by a neck at 90° that suddenly forms partly by coalescence with the neighbouring neck, see Figure 3.13c.

Sharp edges at the end of the necks are observed from Figures 3.13b and 3.13c and that is in high agreement with experiments performed by Kyriakides (2007) for polymer

tubes consisting of polyethylene where the same charateristic sharp edges were noticed. This polymer phenomenon does not appear in Figure 3.11 where the bulge grows at an explosive rate during constantly increasing pressure.

Now that pressure is controlled so that the volume approximately increases linearly with time as in Figure 3.14a, the applied pressure has a maximum soon after that plastic

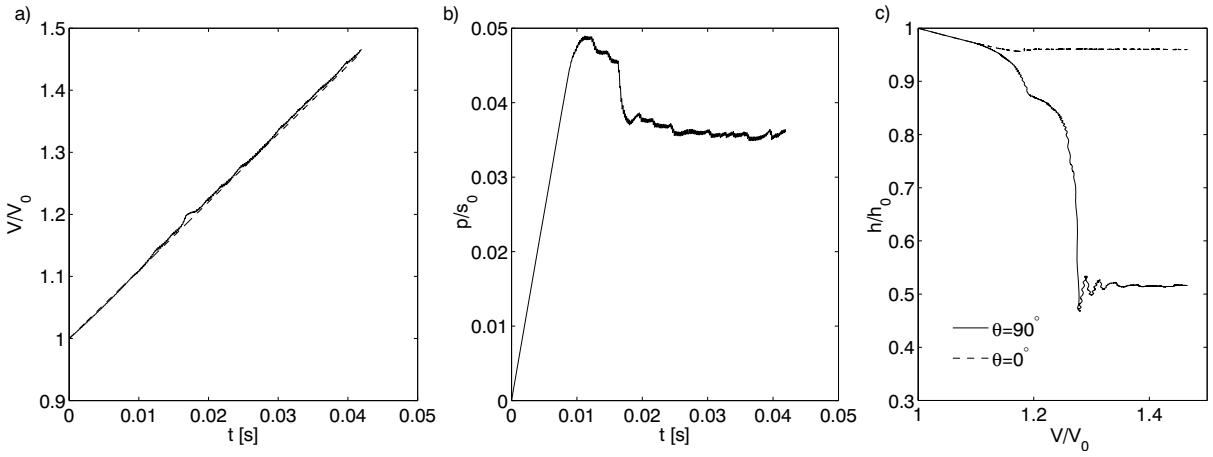

Figure 3.14 Curves for a tube with $h_0 = 0.002$ m, $h_0/R_0 = 0.0392$, $n = 9$, $\xi_9 = 0.01$ and $\xi = 0.01$ under internal volume increasing linearly as a function of time. (a) Normalized internal volume, V/V_0, with respect to time, t. (b) Normalized internal pressure, p/s_0, with respect to time, t. (c) Normalized wall thickness at $0°$ and at $90°$, for $y^3 = 0$, with respect to V/V_0.

deformation has initiated in the bulge region, see Figure 3.14b. The pressure is reduced towards a constant value and is essentially held there while the necks propagate. Still, oscillations on the thickness response at $90°$ are observed to emerge due to larger necks forming next to the one at $90°$. The oscillations die out as the neck at $90°$ coalescs with the one closest and becomes the most dominant neck both along the circumference and along the tube axis. However, as in the case of linearly increasing pressure also for linearly increasing volume the necks are seen to propagate somewhat more in the axial direction.

If the number of initial thin points is reduced as is the situation in Figure 3.15 where the thickness imperfection is specified by $n = 5$ og $\xi_5 = 0.01$ and the radius imperfection is given by $\xi = 0.01$ the most dominant neck develops at $90°$ without coalescence of necks. In contradiction coalescence of necks is needed in order to obtain the most dominant neck at $90°$ when the number of thin points along the quarter of the tube is further increased from 9 to 13 as observed from Figure 3.16. Generally it is concluded that when a smaller number of necks ($n \leq 5$) are initiated as is the case in Figure 3.15 the neck at $90°$ grows most dominant without coalescence whereas for a larger nummer of necks coalescence is reached in order to achieve the most dominant neck at $90°$. Therefore the smallest number of necks produces the earliest neck propagation at $90°$ as was discovered in paper [P2]. Also for all cases analysed in paper [P2] the growth rate of the necks is observed to switch during neck propagation so that the finally largest neck achieved at $90°$ is not the largest neck obtained initially, see Figures 3.13, 3.15 and 3.16.

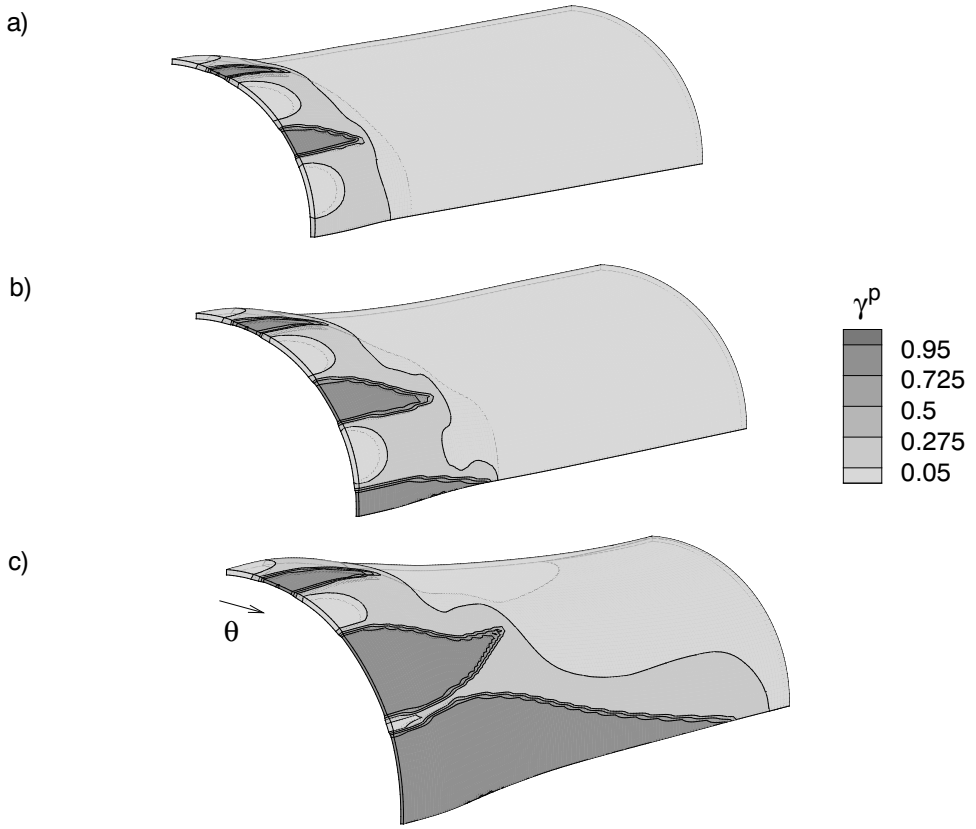

Figure 3.15 Plastic strain contours γ^p of the deformed tube with $h_0 = 0.002$ m, $h_0/R_0 = 0.0392$, $n = 5$, $\xi_5 = 0.01$ and $\xi = 0.01$. The applied pressure rate is controlled to give $\dot{V}/V_0 = 11.0\ \text{s}^{-1}$ and θ increases from 0° to 90° in the direction shown. (a) $V/V_0 = 1.198$ and $\varepsilon_{\text{av}} = 0.191$ (b) $V/V_0 = 1.255$ and $\varepsilon_{\text{av}} = 0.260$ (c) $V/V_0 = 1.582$ and $\varepsilon_{\text{av}} = 0.434$.

Under linear volume-time dependence a pressure maximum as the one pictured in Figure 3.14b is seen to develop for all cases considered with the pressure reducing until it achieves an essentially constant value during bulge formation.

Next, a situation neither shown nor mentioned in paper [P2] is to be presented. The thickness imperfection and the radius imperfection are given by $n = 1$, $\xi_1 = 0.01$ and $\xi = 0.01$ respectively so that along the quarter circumference of the tube only one thin point is applied and the appertaining plastic strain contours are illustrated in Figure 3.17. The necks propagate and they thin much more down than was observed for the corresponding plane strain 2D tube from paper [P1] where only a thin point was given at $\theta = 90^\circ$ (by $n = 1$, $\xi_1 = 0.01$) and an almost invisible neck development was seen. However, the average strain $\varepsilon_{\text{av}} = 0.298$ at the largest internal normed volume $V/V_0 = 1.534$ never reaches the somewhat larger values of $\varepsilon_{\text{av}} \geq 0.4$ obtained for all the earlier cases shown and almost no bulge is seen to form in Figure 3.17. Also in Figure 3.17, the plastic strain γ^p achieves a larger value of 0.1 just before necking occurs whereas the plastic strain $\gamma^p = 0.05$ for all other cases shown previously in Figures 3.13, 3.15 and 3.16 has not

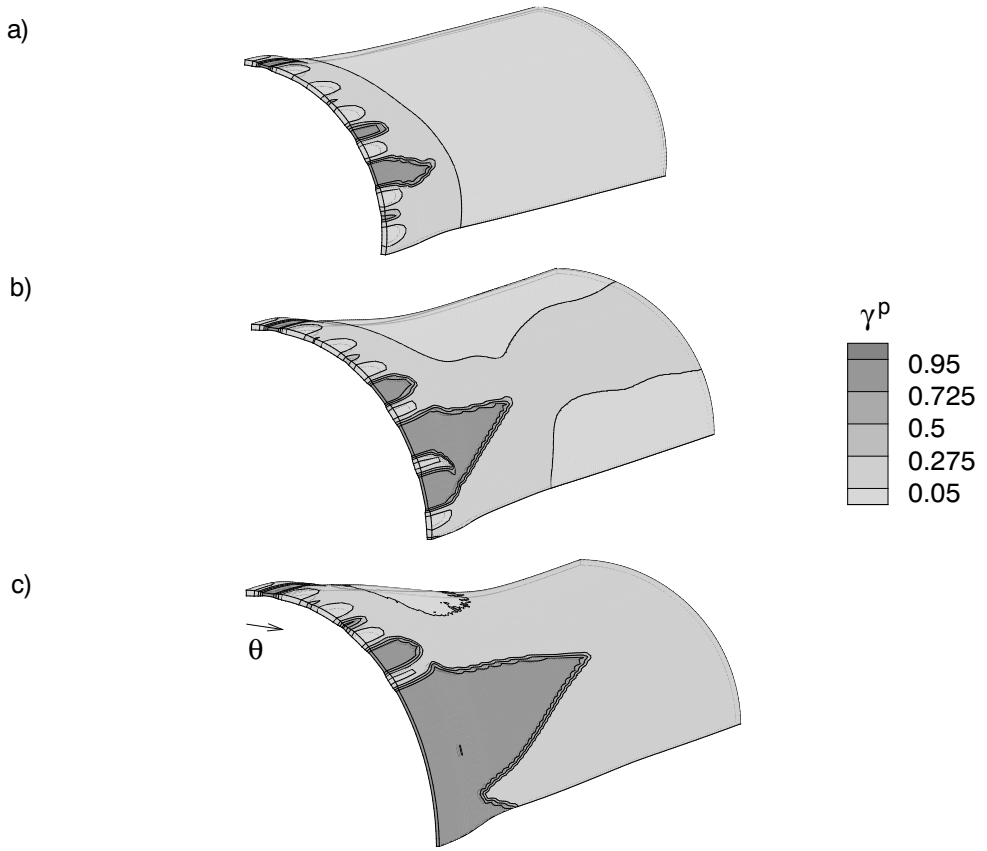

Figure 3.16 Plastic strain contours γ^p of the deformed tube with $h_0 = 0.002$ m, $h_0/R_0 = 0.0392$, $n = 13$, $\xi_{13} = 0.01$ and $\xi = 0.01$. The applied pressure rate is controlled to give $\dot{V}/V_0 = 11.0$ s^{-1} and θ increases from 0° to 90° in the direction shown. (a) $V/V_0 = 1.218$ and $\varepsilon_{\text{av}} = 0.214$ (b) $V/V_0 = 1.306$ and $\varepsilon_{\text{av}} = 0.296$ (c) $V/V_0 = 1.510$ and $\varepsilon_{\text{av}} = 0.420$.

grown that large before necking and bulging initiate. This shows that in case of $n = 1$, $\xi_1 = 0.01$ and $\xi = 0.01$ even though a neck develops it localizes a little less than is the case when several necks around the circumference are initiated. All in all some trace is kept to the less localized single neck in paper [P1].

Figure 3.18a shows that the enclosed volume is very close to increase linearly with respect to time for the situation considered in Figure 3.17. The corresponding pressure curve has a maximum just before plastic deformation initiates and it is generally not much different from the pressure curves earlier obtained for cases of linear volume-time dependence. However, it is observed that as the pressure maximum is passed the pressure reduces slowly for a larger time interval until $t \approx 0.02$ s where the pressure decreases very fast and converges towards an approximately constant value.

Since no other necks develop next to the one at 90° no oscillations are found on the thickness response in Figure 3.18c. Also the constant thickness achieved in the neck is noticeable larger than the corresponding thicknesses obtained in any of the previously investigated cases which is in agreement with the observation of a little less neck local-

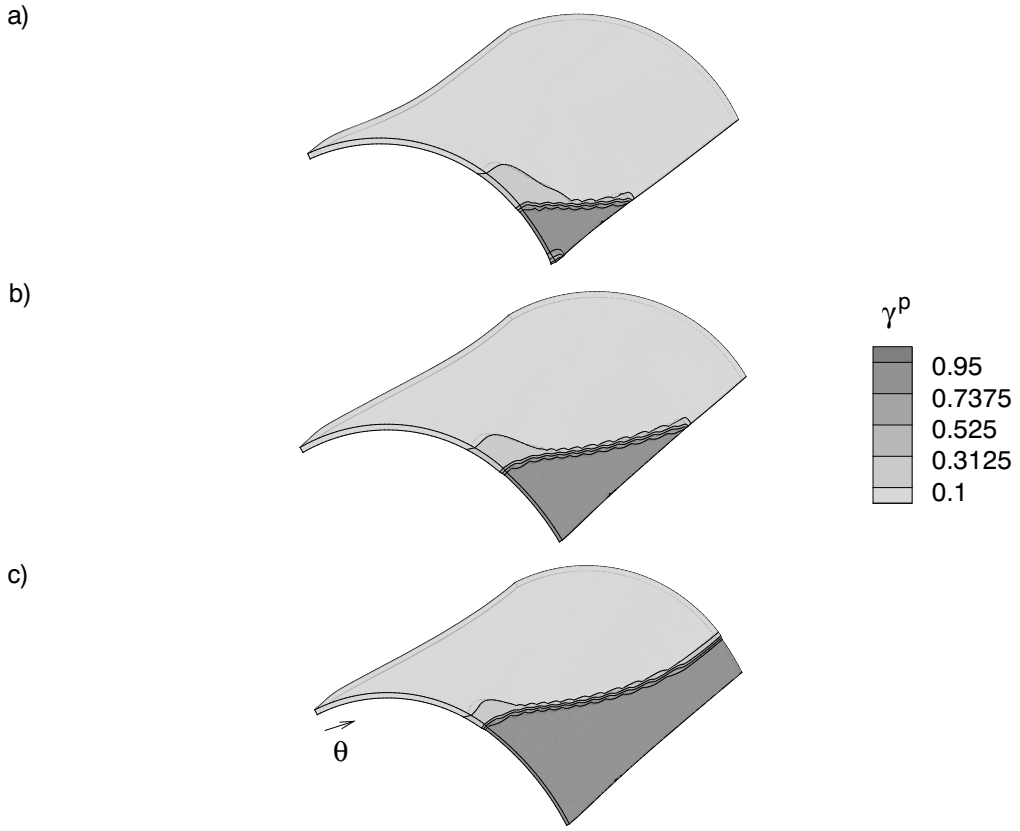

Figure 3.17 Plastic strain contours γ^p of the deformed tube with $h_0 = 0.002$ m, $h_0/R_0 = 0.0392$, $n = 1$, $\xi_1 = 0.01$ and $\xi = 0.01$. The applied pressure rate is controlled to give $\dot{V}/V_0 = 11.0\,\mathrm{s}^{-1}$ and θ increases from 0° to 90° in the direction shown. (a) $V/V_0 = 1.257$ and $\varepsilon_{\mathrm{av}} = 0.198$ (b) $V/V_0 = 1.336$ and $\varepsilon_{\mathrm{av}} = 0.237$ (c) $V/V_0 = 1.534$ and $\varepsilon_{\mathrm{av}} = 0.298$.

ization for the situation in Figure 3.17.

Here, as in paper [P1] it is generally seen that necks only initiate at thin points along the circumference whereas for metal rings a short wave necking pattern tends to develop along the circumference independent of the spacing between the initial thin points. As mentioned, this difference is thought to be a consequence of the stress peak being followed by plastic softening which is characteristic for a thermoplast.

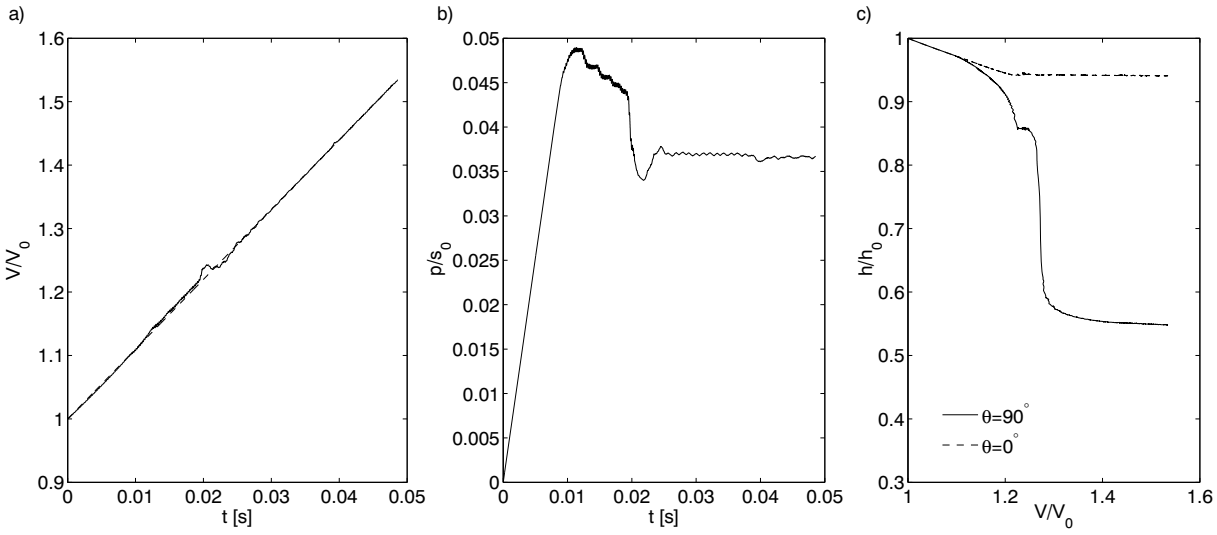

Figure 3.18 Curves for a tube with $h_0 = 0.002$ m, $h_0/R_0 = 0.0392$, $n = 1$, $\xi_1 = 0.01$ and $\xi = 0.01$ under internal volume increasing linearly as a function of time. (a) Normalized internal volume, V/V_0, with respect to time, t. (b) Normalized internal pressure, p/s_0, with respect to time, t. (c) Normalized wall thickness at $0°$ and at $90°$, for $y^3 = 0$, with respect to V/V_0.

3.3 Development of high intensity shear zones in a fiber reinforced polymer

Both analytical and experimental investigations have dealt with the failure mechanisms of polymer composites and they show that high strain and stress concentrations in the matrix may be expected to cause cracking of the matrix or debonding and interfacial fracture (Karbhari and Wilkins (1990); Hampe and Marotzke (1992); Andrews et al. (1994); Laws and Dvorak (1988)). Analyses of diagonal high intensity shear zones forming in a polymer matrix between the reinforcement of transversely staggered overlapping fiber ends are carried out in paper [P3] showing high strain and stress concentrations to develop at the sharp fiber edges. This is in high agreement with observations for cases of stiff fibers embedded in a metal matrix performed by Llorca et al. (1991) and Tvergaard (2003) even though the mechanical behaviour of a polymer matrix is rather different from that of a metal matrix. The observations are furthermore supported by experiments carried out by Hampe and Marotzke (1992) predicting brittle facture at the fiber-matrix interface during fiber pull out in a glass fiber reinforced polycarbonate and also Laws and Dvorak (1988) has presented simulations of interface damage and matrix cracking in fiber reinforced epoxy. Finally, a case is shown in which periodicity of the polymer matrix between the fibers has been assumed.

The specimen to be studied is illustrated in Figure 3.19. It has initial overall length

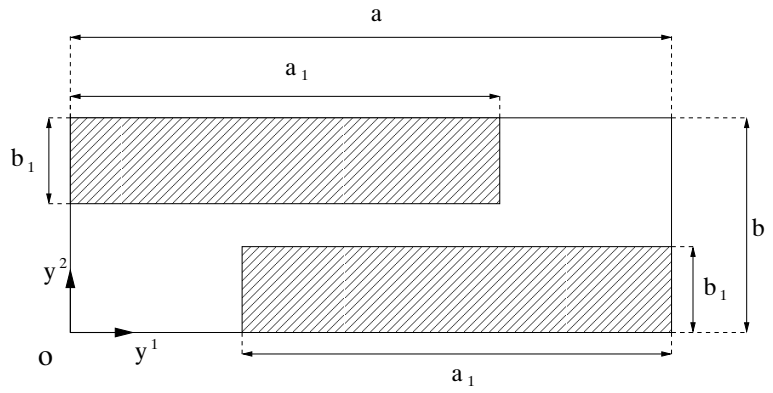

Figure 3.19 The plane strain specimen to be analysed defined by length a, width b, half fiber length a_1 and half fiber width b_1.

a and width b, and it is a part of a fiber reinforced polymer with periodically distributed stiff fiber ends. The fibers are transversely staggered with symmetry boundary conditions applied along $y^1 = 0$ and $y^2 = 0$ so that each fiber specified by the total length $2a_1$ and width $2b_1$. Here, focus is on the region near the fiber overlap since the results are expected to describe the material behaviour between much larger fibres as well. As shown in Figure 3.19 the y^1-axis follows the length a of the specimen and the y^2-axis follows the width b in the Cartesian reference coordinate system y^i.

The numerical analyses are executed for the length and width ratios $a_1/a = 2/3$, $b/a = 1/4$ and $b_1/b = 1/3$ unless otherwise stated for the specific cases considered. Actually, the numerical calculations ar carried out for the unrealistically large fiber length $a = 0.60$ m, but at the loading rates applied in paper [P3] inertia plays nearly no role. Therefore the results to be presented later on also apply to realistic fiber dimensions specified by the length and width ratios just mentioned above. Since plane strain conditions are assumed to prevail in the third direction perpendicular to the (y^1,y^2)-plane in Figure 3.19 the finite element code is based on a two dimensional plane strain implementation of the constitutive model as discussed in section 2.1.2.

A prescribed time dependent velocity

$$v(t) = \begin{cases} v_1 t/t_r & \text{for} \quad t < t_r \\ v_1 & \text{for} \quad t > t_r \end{cases} \tag{3.12}$$

is imposed along $y^1 = a$ so that

$$\dot{u}_1(a, y^2) = v(t) \qquad \text{for} \qquad 0 \leq y^2 \leq b \tag{3.13}$$

where t_r is the ramping time. For all the cases studied in paper [P3] and to be shown here subsequently, the constant velocity v_1 is chosen to $v_1 = (5/6)a$ s^{-1} and the ramping time is fixed to $t_r = 0.02$ s.

If the volume V_c is to remain constant during deformation (i.e. the region analysed is incompressible), the incremental displacement rate $[\dot{u}_2]_{incomp}$ to be applied along $y^2 = b$ in the direction of y^2 is given by

$$[\dot{u}_2]_{incomp} = -\dot{u}_1 \frac{b + u_2}{a + u_1} \tag{3.14}$$

where u_1 is the displacement at $y^1 = a$ in the direction of y^1, u_2 is the displacement at $y^2 = b$ in the direction of y^2 and $\dot{u}_1$ is found from eq. (3.13).

Along $y^2 = b$ a velocity prescribed by

$$\dot{u}_2 = \alpha[\dot{u}_2]_{incomp} \qquad \text{for} \qquad 0 \leq \alpha \leq 1 \tag{3.15}$$

is applied. The limit $\alpha = 1$ corresponds to pure incompressibility whereas $\alpha = 0$ results in $\dot{u}_2 = 0$ causing a significant volume change. Different values of α have been chosen in paper [P3] and in the analyses to be discussed subsequently. As argued in 2.1.2 a cut-off that disables plastic flow when λ_c exceeds $r_\lambda \lambda_{max}$ is implemented and for the cases to be shown here $r_\lambda = 0.85$ has been chosen.

Figure 3.20 illustrates the contours for a specimen with the dimensions $b/a = 1/4$, $a_1/a = 2/3$ and $b_1/b = 1/3$ for $\alpha = 0.75$ at the stage of $\varepsilon_1 = 0.0575$. Here, ε_1 is the logarithmic strain defined by $\varepsilon_1 = \ln(1 + u_1/a)$, ε_{max} is the maximum principal logarithmic strain, λ_c/λ_{max} is the normalized stretch and $\sigma_m = \frac{1}{3} G_{kl} \sigma^{kl}$ is the mean stress. The fibers consist of E-glass that is approximated to be much stiffer than the polymer matrix. Here, focus is on investigating the material behaviour of the matrix

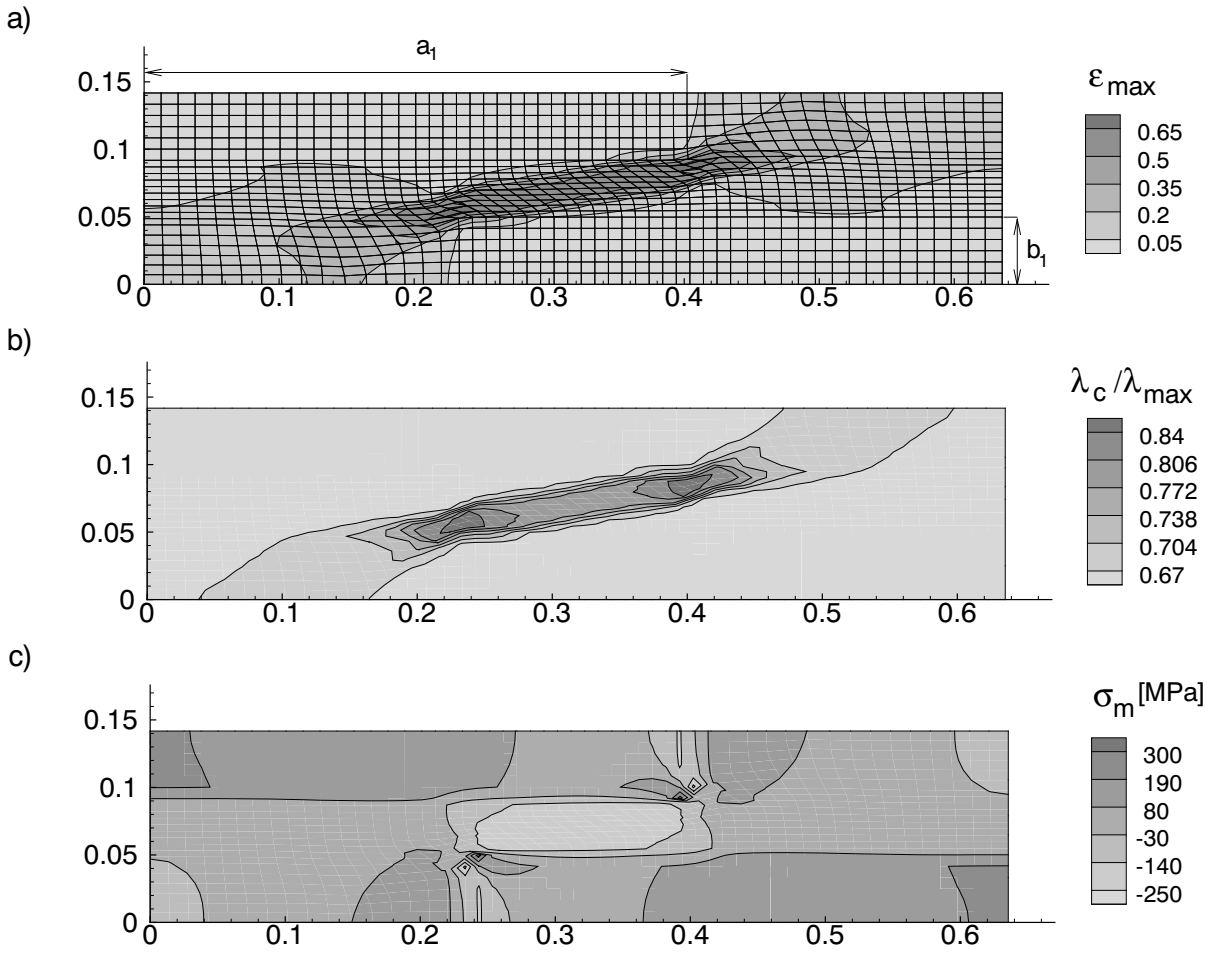

Figure 3.20 Contours for the case of $\alpha = 0.75$, $\varepsilon_1 = 0.0575$ with the initial length $a_1/a = 2/3$ and the initial widths $b/a = 1/4$, $b_1/b = 1/3$. (a) Maximum principal logarithmic strain ε_{max} (b) Normalized stretch λ_c/λ_{max} (c) Mean stress σ_m .

betweeen the overlapping fiber ends and the material behaviour of the fibers is modelled as isotropic elastic.

From Figure 3.20a and 3.20c it is seen that the embedded fibers result in high strain and stress concentrations at the sharp fiber edges. This is in agreement with experiments performed by Hampe and Marotzke (1992) for a polymer composite and the observations that fibers embedded in a metal give rise to higher strain concentrations at the sharp fiber edges (Llorca et al. (1991); Tvergaard (2003)). As predicted, a diagonal band of elevated shear intensity is seen to form between the fibers in Figure 3.20 as is the case for fiber reinforced metal (Llorca et al. (1991)).

At the stage illustrated in Figure 3.20b the polymer deforms purely elastically at the very high strain concentrations emerging at the sharp fiber edges due to the exceeded cut-off at $\lambda_c = 0.85\lambda_{max}$ where high network stiffening has taken over. Elsewhere, the network stiffening obtained is not high enough to reach the cut-off value of λ_c. However,

in the zone of high shear intensity the network stiffening is high (Figure 3.20b) and the nearly parallel mesh lines in the deformed state of the shear zone in Figure 3.20a are a consequence of the polymer deforming almost elastically. This reveals the network hardening to be that large that any further plastic flow in the shear zone is already heavily suppressed by the influence of $\boldsymbol{\sigma}_B$ in eq. (2.26).

Negative mean stresses develop in the load carrying matrix between the fibers because $\alpha = 0.75$ nearly corresponds to the case of uniaxial plane strain deformation where $\alpha = 1$. For lower values of α in paper [P3] high strain and strain concentrations are still found at the sharp edges of the fiber, but the diagonal shear zone fades in intensity as α is gradually decreased to $\alpha = 0$. This is seen from Figure 3.21 where $\alpha = 0$. Also, the rate at which

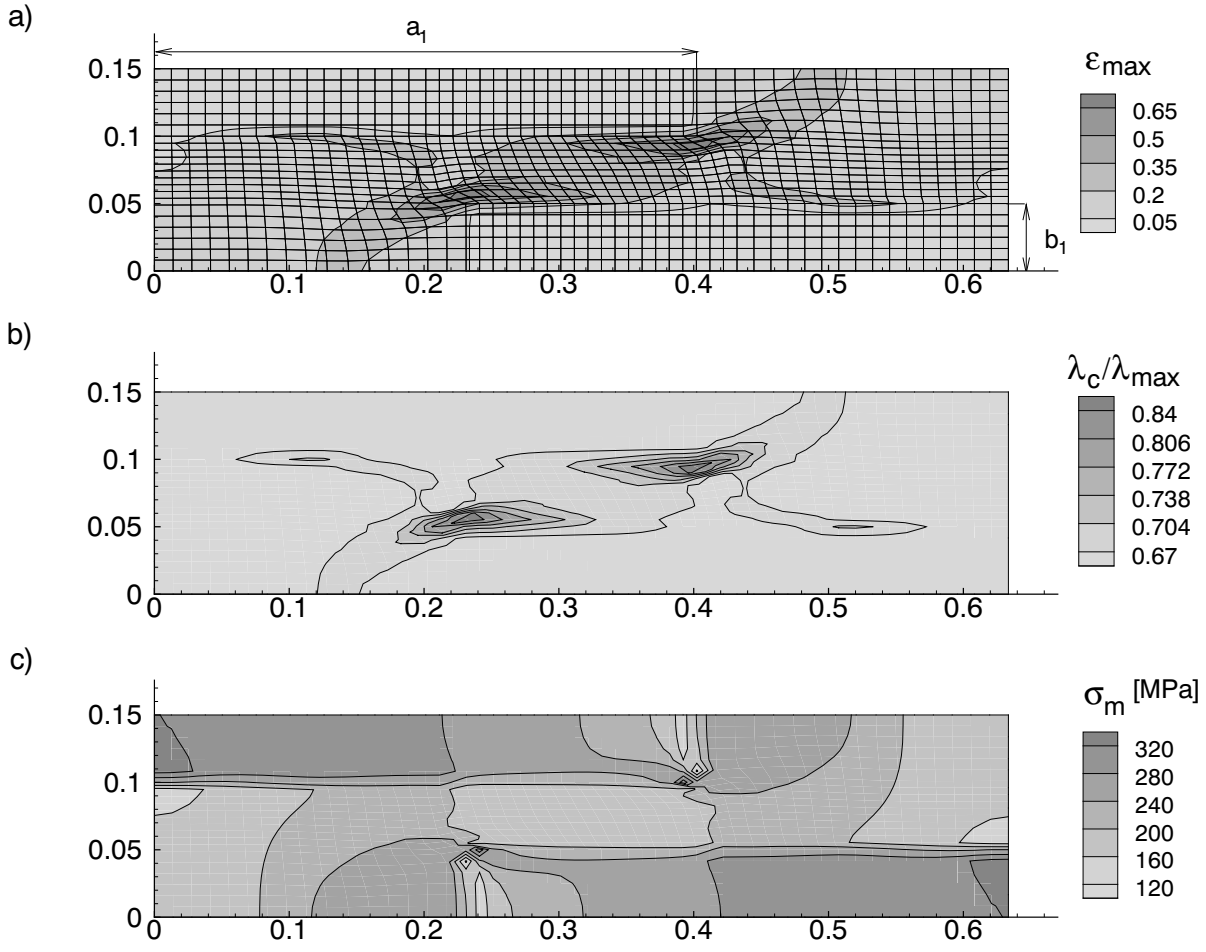

Figure 3.21 Contours for the case of $\alpha = 0$, $\varepsilon_1 = 0.0542$ with the initial length $a_1/a = 2/3$ and the initial widths $b/a = 1/4$, $b_1/b = 1/3$. (a) Maximum principal logarithmic strain ε_{max} (b) Normalized stretch λ_c/λ_{max} (c) Mean stress σ_m .

the local strain level contours in Figure 3.20a are achieved with respect to ε_1 is a little lower as α is reduced from $\alpha = 0.75$ to $\alpha = 0.50$. However, the same strain levels are reached much slower as $\alpha = 0.50$ is reduced to $\alpha = 0$. This is illustrated in figures

and discussed in much more detail in paper [P3]. The level of average mean stress in the matrix area between the fibers is elevated as α is decreased first to $\alpha = 0.50$ and finally to $\alpha = 0$ due to more deviation from uniaxial plane strain.

The stress curves in Figure 3.22 present the average stress σ_1 computed along $y^1 = a$ and average stress σ_2 computed along $y^2 = b$ versus the logarithmic strain ε_1 for the different values of α chosen. It is seen that an increased α results in a reduced level of

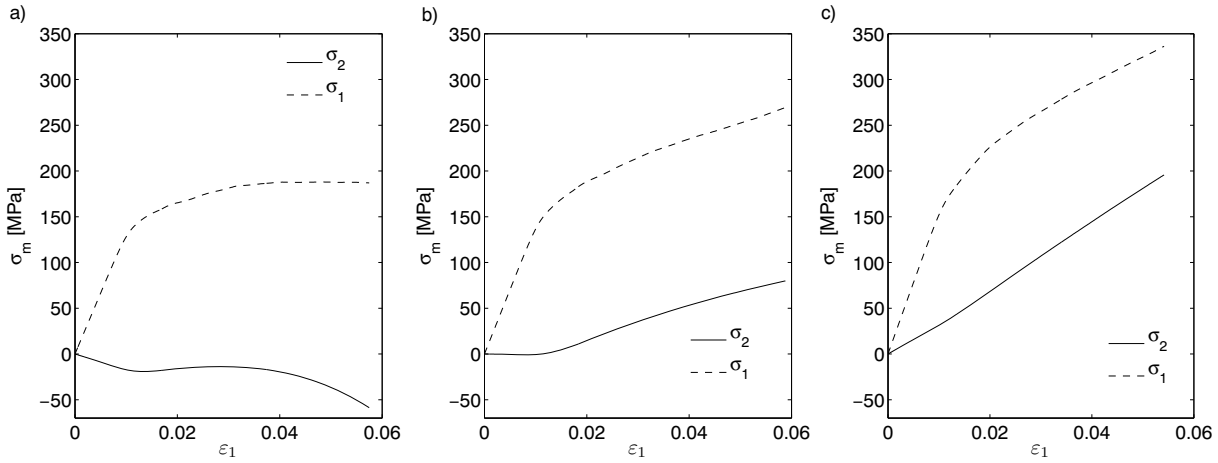

Figure 3.22 Average stress σ_1 along $y^1 = a$ and average stress σ_2 along $y^2 = b$ with respect to logarithmic strain ε_1. (a) $\alpha = 0.75$, corresponding to Figure 3.20 (b) $\alpha = 0.50$ (c) $\alpha = 0$, corresponding to Figure 3.21.

the transverse stress σ_2 in accordance with the prescribed overall deformation that also introduces the decrease of σ_m. The same is observed to be the case for the longitudinal stress σ_1 particularly at higher values of the strain ε_1. This is in agreement with the rising stress triaxiality for decreasing α.

In paper [P3] a comparison with an infinitely stiff fiber embedded in the polycarbonate matrix reveals the E-glass fibers to be that highly stiff compared to the surrounding polymer matrix that their results can be assumed be a good estimation for other fibers of high stiffnes. Also, investigations predict among others the speed at which the local strain levels form with respect to the strain ε_1 to be very sensitive to fiber spacing and fiber thickness. A more detailed explanation is given in paper [P3].

If the overlap length of the fiber ends is much larger than the spacing the material behaviour of the matrix between the stiff fibers can be assumed nearly periodic. Figure 3.23 shows the contours for the periodic case corresponding to the situation in Figure 3.21 where $\alpha = 0$. An imperfection is imposed on the plastic strain increment $\dot{\gamma}^p$ given by eq. (2.13) to trigger a possible onset of shear localization at $y^2 = b/2$. The average shear strain $\gamma = 0.489$ obtained at the stage depicted in Figure 3.23 is identical to that achieved for the case in Figure 3.21 in order to be able to compare the two cases. For the fiber reinforced case in Figure 3.21 the average shear strain is computed along the central transverse line of the overlap so that it is not affected by the strain concentrations

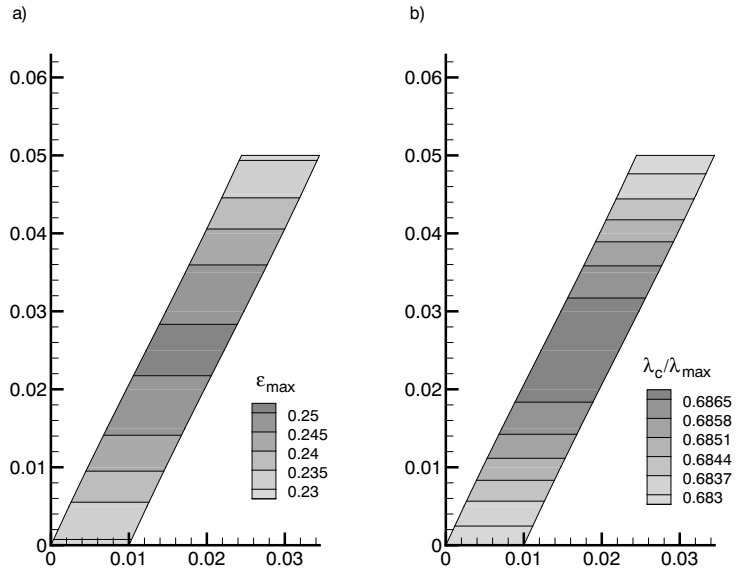

Figure 3.23 Contours for the case of $\alpha = 0$ assuming periodicity of the polymer matrix between the fibers at the stage of the average shear strain $\gamma = 0.489$. (a) Maximum principal logarithmic strain ε_{max} (b) Normalized stretch λ_c/λ_{max}. The region analysed is specified by the initial thickness $a/a_{old} = 1/60$ and hight $b/a_{old} = 1/12$.

emerging at the fiber corners. Similar to the actual case in Figure 3.21 no clear localization into a shear band is seen in Figure 3.23 though a slightly increased strain is found at the centre of the matrix between the fibers as is shown in Figure 3.21.

Figure 3.24 presents the shear stress τ at the fiber-matrix interface with respect to the average shear strain γ for the fiber reinforced case in Figure 3.21 and the periodic case in Figure 3.23 respectively. For the fiber reinforced case the shear stress τ is computed from the forces in the five nodes along the fiber-matrix interface close to the transverse line at the centre of the overlap from which γ is found. In Figure 3.24 the curve depicting the fiber reinforced case ends at $\gamma = 0.489$ as in Figure 3.21 and corresponding to the periodic situation shown in Figure 3.23. The fiber ends in Figure 3.21 influence the shear stress as observed in Figure 3.24 where the shear stress for the fiber reinforced case deviates somewhat from the shear stress corresponding to the periodic case assuming infinitely long fibers. A longer fiber overlap than that in Figure 3.21 would cause the curve obtained for the fiber reinforced case to converge towards the stress curve of periodicity. However, the stress curves share nearly the same value $\gamma \approx 0.097$ at the maximum points where the roll over to plastic flow occurs.

From Figure 3.24 it is observed that at $\gamma = 0.489$ the fiber-reinforced case in Figure 3.21 as well as the periodic case in Figure 3.23 are far from achieving the final network hardening. This is also seen directly from Figure 3.21a where the shearing in the middle of the overlap zone is much less than that in the region of strain concentration peaks.

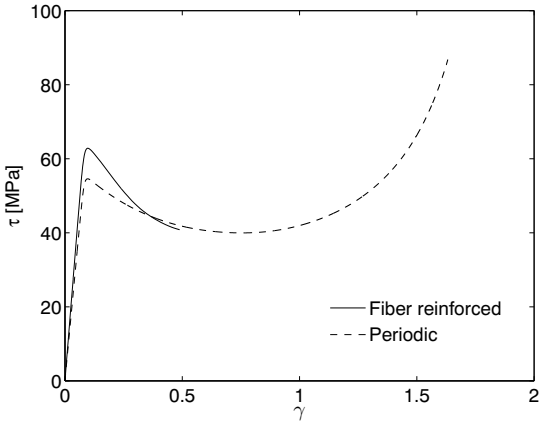

Figure 3.24 Shear stress τ with respect to average shear strain γ for the fiber reinforced case in Figure 3.21 and the periodic case in Figure 3.23 respectively where $\alpha = 0$. The periodic case has an implemented cut off at $\lambda_c = 0.95\lambda_{max}$ that is never reached.

When the peak in Figure 3.24 has been passed the plastic strain at $y^2 = b/2$ increases slightly without really localizing as mentioned previously, but as hardening takes over the deformation, the zone of higher plastic strain stops localizing and the high plastic strain propagates to the entire region similar to the phenomenon of shear zone propagation, or shear band widening, discussed by Wu and Van der Giessen (1994) and the phenomenon of neck propagation observed in paper [P1]. In general it is found that Figures 3.23 and 3.24 predict the assumption of periodicity for the situation illustrated in Figure 3.21 to be reasonable. This makes it possible to model the mechanical behaviour of the polymer matrix between the stiff fibers in a simplified way.

3.4 Numerical computations for polyethylene

All the investigations carried out in papers [P1], [P2] and [P3] and presented in the previous chapters are based on material parameters that represent PC or another polymer with a similar uniaxial stress-strain response as the one illustrated in Figure 3.1. However, it must be emphasised that under tensile load PC tends to fail before large plastic strains are achieved as discussed by Gearing and Anand (2004). In the present section other polymers are studied, which do not reach the high stresses obtained in Figure 3.1 before hardening but still share the main polymer characteristics. In Figure 3.25 stress-strain responses are shown representing another thermoplast, polyethylene terephthalate (PET), when subjected to uniaxial tension. Only the numerical parameters C_r, N, s_{ss} and h have been changed from those of Figure 3.1 in order to obtain the curves in Figure 3.25.

The slightly different curves in Figure 3.25 all represent PET at the rate 1 s^{-1} and the materials are denoted by A, B, C, D respectively. Compared to the polymer in Figure 3.1, the network hardening occurs at larger strains when the material considered is PET. The delayed hardening is introduced through a much larger value of N in eq. (2.27) than is

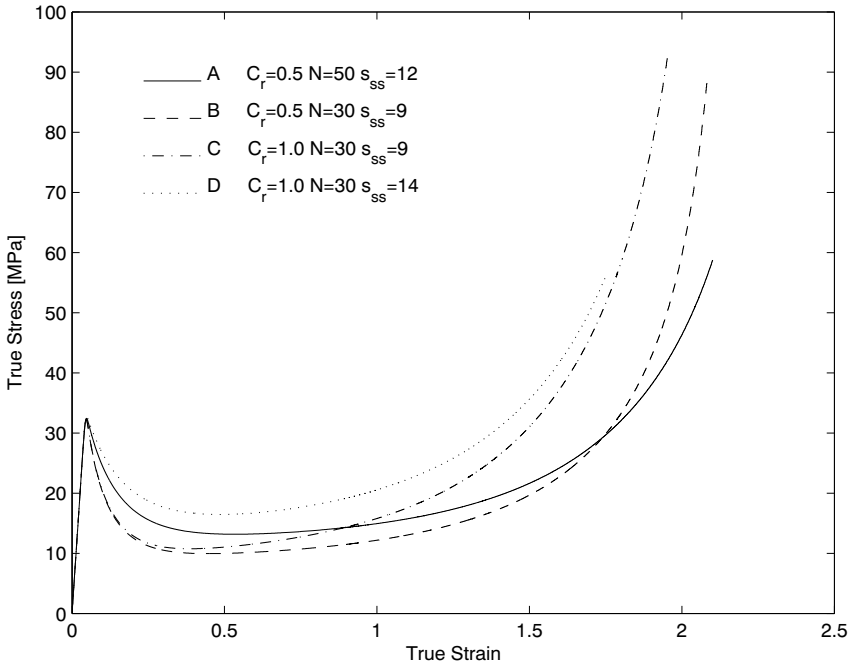

Figure 3.25 Stress-strain curves for uniaxial tension at the rate 1 s^{-1} for different materials chosen with the true strain being logarithmic.

the case in [P1]-[P3] where $N = 2.3$. Also, the first stress peak before plastic softening is much lower for PET in Figure 3.25 than is the case for the polymer in Figure 3.1.

In Figure 3.26 the plastic strain contours are shown in a deformed state for a tube that consists of material A. The initial geometry corresponds to that analysed in Figure 3.5 with a larger initial imperfection along the circumference of the tube specified by $n = 1$ and $\xi_1 = 0.01$. The internal pressure increases linearly with respect to time at a rate specified by $\dot{p} = 41.0$ MPa/s and the mesh is graduated since particularly the region at 90° where a neck is present is of high interest. In Figure 3.26 it is seen that the neck thins much more down than was found for PC or a similar polymer, see Figure 3.3 for comparison. This is not surprising since the PET material hardens much later than the polymer in Figure 3.1 (compare the stress-strain curve in Figure 3.25 with the lower tension curve in Figure 3.1) and in Hutchinson and Neale (1983) the Maxwell line contruction for neck propagation prescribes that a wide strain range of the softening region results in more thinning of the respective neck independent of the stress level.

The mesh in the neck in Figure 3.25 is observed to deform so strongly during the large thickness reduction resulting from necking that mesh distortion plays a big role. Remeshing would be required in order to avoid this mesh distortion in the neck particularly when the neck propagates even further than illustrated in Figure 3.26. Both 2 and 4 elements through the thickness of the tube in Figure 3.26 were tried, but causing even more distorted elements than is the case with one element through the thickness they did not solve

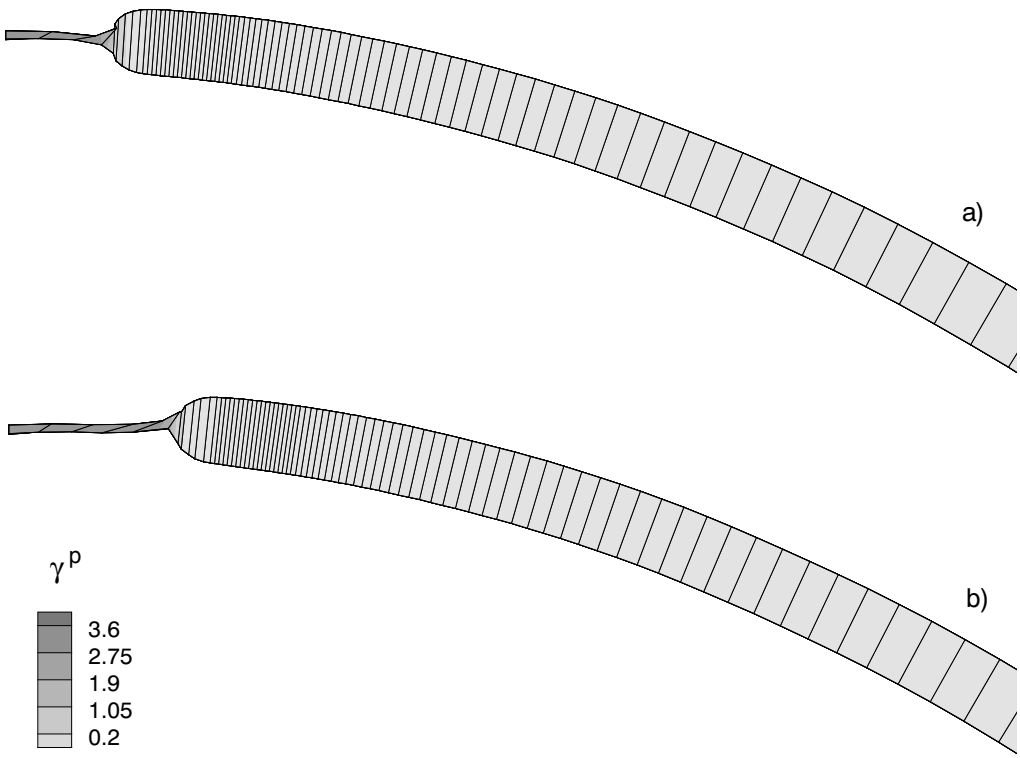

Figure 3.26 Plastic strain contours γ^p of the deformed thin walled tube at the region around the location 90° where a neck is present. The initial tube is specified by $h_0 = 0.002$ m, $h_0/R_0 = 0.0392$, $n = 1$ and $\xi_1 = 0.01$ and the applied pressure rate is $\dot{p} = 41.0$ MPa/s. Here, the tube consists of the PET material A depicted in Figure 3.25.

the problem of large mesh distortion. The neck in Figure 3.26 localizes much more than is the case for the situation presented in Figures 3.5 and 3.6 where no clear neck was found. This variation arises due to the different choise of material for the cases in Figure 3.26 and Figure 3.5 respectively and it reveals that the extent of necking is very material dependent.

Next, in Figure 3.27 plastic strain contours in the deformed state are given for a tube consisting of a different material D. A different number of elements (1,2,3,4,5) through the thickness have been applied and 2 elements through the thickness were observed to result in least mesh distortion contrary to the case in Figure 3.26 where 1 element through the thickness was sufficient. The selected material D has the stress-strain response given in Figure 3.25. Material D obtains less softning and earlier network hardening compared to material A and therefore the neck in Figure 3.27 is a little thicker than that observed in Figure 3.26. However, the neck in Figure 3.27 is still thinner and much more deformed than those in Figure 3.3 representing the polymer in Figure 3.1. If the computation for the neck in Figure 3.27 was to continue any further, remeshing would be required. Otherwise

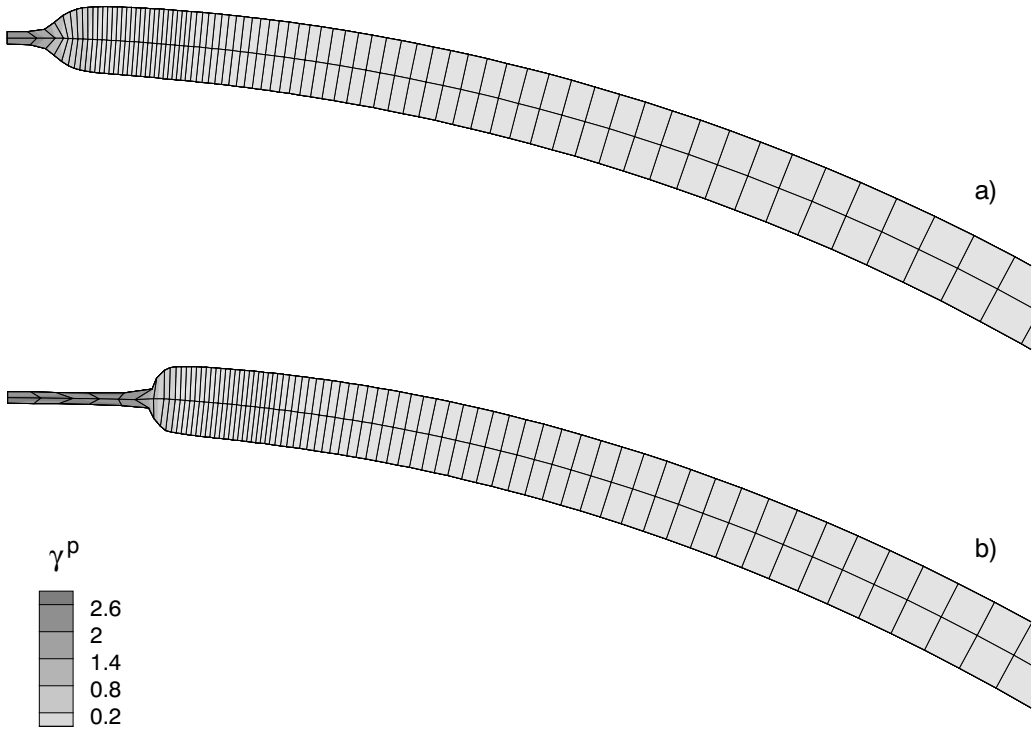

Figure 3.27 Plastic strain contours γ^p of the deformed thin walled tube at the region around the location 90° where a neck is present. The initial tube is specified by $h_0 = 0.002$ m, $h_0/R_0 = 0.0392$, $n = 1$ and $\xi_1 = 0.01$ and the applied pressure rate is $\dot{p} = 41.0$ MPa/s. Here, the tube consists of the PET material D depicted in Figure 3.25.

the mesh in the neck gets so heavily distorted that the computation stops.

Experiments have been carried out by Kyriakides (2007) for long polymer tubes consisting of PET with the dimensions $L_0/D_0 = 9.03$ and $D_0/t = 6.77$ where L_0 is the initial length of the tube, D_0 is the initial average diameter of the tube and t is the initial wall thickness. As a tube was expanded a single neck formed along the tube circumference. After that the neck had localized and propagated somewhat along the circumference of the tube the thin material in the neck started to bulge out of the near-circular cross-section. The bulged neck obtained a thickness at about 1/5 of the deformed wall thickness where no neck was present. Figure 3.28 shows the cross section of the deformed tube from the experiment performed by Kyriakides (2007) after the neck has bulged. Also in Figure 3.27 where the tube consists of material D the neck at 90° has a thickness of about 1/5 of the deformed wall thickness at 0°.

The appearance of a bulged neck is a result of the wide strain range of the softening region that is characteristic for PET as the delay in network hardening gives rise to a very thin neck. The heavily elongated neck needs extra space which it achieves either through

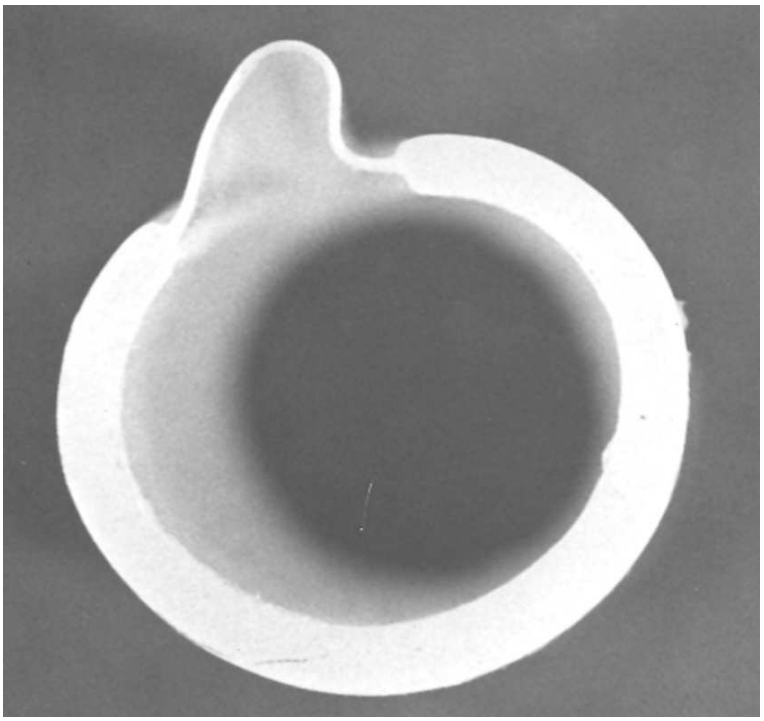

Figure 3.28 Cross section of a long expanded tube made of polyethylene after a neck has developed and started to bulge (from Kyriakides (2007)).

expansion of the entire tube (as is the case in paper [P2]), or through bulging of the neck, or perhaps by a combination of these two mechanisms. Here for PET, due to the larger softening the elongated neck will prefer to bulge like a bubble gum whereas the harder and less thinned necks in paper [P2] result in tube expansion without any bulging in the respective necks. The material used in paper [P2] represents PC or a similar polymer where the softening occurs over a much shorter strain interval also causing the necks to thin less down before hardening is obtained. Since the necks harden fast for PC the entire tube in paper [P2] expands in order to make room for the longer necks.

A numerical study demontrating the occurrence of the bulged neck would be interesting. First, a full three dimensional analysis very similar to the ones performed in paper [P2] is needed for the PET material. However, the elements in the neck in Figure 3.27 are so heavily distorted that the computations become less reliable and remeshing is required anyway. Also, the three dimensional analysis is very time consuming due to a higher number of total degrees of freedom and due to a very small time step needed in order to sustain stability despite mesh distortion. Instead, a much simplified 2D analysis is carried out to try to illustrate the mechanism that leads to bulging.

In the simplified two dimensional analysis of the region of necking it is assumed that the rest of the structure becomes infinitely stiff compared to the soft necking region. In order to model this the part of the structure away from the necking region is made infinitely stiff so that no deformation is allowed for anywhere but in the neck. Thus, the

tube is clamped a little distance from the neck. Thereby the type of necking behaviour observed in the experiments of Kyriakides (2007) and presented in Figure 3.28 can be illustrated by the 2D results in Figure 3.29.

In Figure 3.29 the plastic strain contours for a tube identical to that in Figure 3.27 are shown, but here with the only difference that after some neck propagation the tube

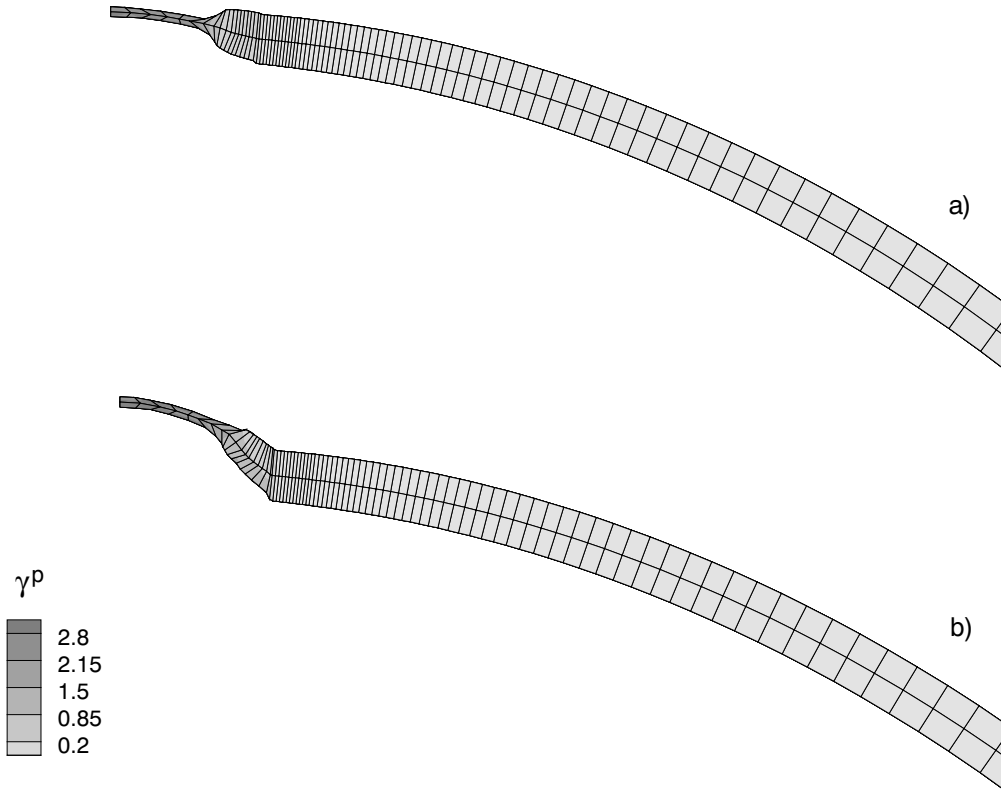

Figure 3.29 Plastic strain contours γ^p of the deformed thin walled tube illustrated in Figure 3.27 with the difference that the tube is clamped against further expansion in the interval $\theta \in [0°; 84.5°]$.

is clamped against any further expansion in the interval $\theta \in [0°; 84.5°]$, starting from the state illustrated in Figure 3.27b. This clamping attempts to simulate the situation where the thick part of the long tube is so much stiffer than the thin neck region that the thick part does not deform anymore. After this stage, the neck in Figure 3.29 begins to bulge as was seen in the experiments (Figure 3.28) carried out by Kyriakides (2007) and discussed previously. Somewhere between the parameters of PC, Figure 3.1, and the parameters of PET, Figure 3.25, a switch in necking mode must occur, causing the necking behaviour to change from pure neck propagation and subsequent tube expansion to neck bulging and less tube expansion if any.

Chapter 4
Discussion

The subject of the present thesis is large deformations of polymers with a main focus on polymers within the group of thermoplasts. Three papers [P1]-[P3] written during the authours Ph.D study have been included at the end of this thesis. Two different, but somewhat similar constitutive models are presented and discussed. Both models introduce plastic softening followed by hardening at large strains and they are implemented numerically in finite element programs, using the dynamic principle of virtual work and Newmark integration. Various problems are solved and discussed in detail especially in the papers [P1]-[P3] for one particular chosen polymer and the main observations are summarised in the present work. Additional results not previously published are added here. Furthermore, a different polymer (PET) than that of papers [P1]-[P3] is investigated leading to new findings as well.

In paper [P1] a 2D polymer tube is analysed numerically with respect to neck initiation and neck formation along the circumference of the expanding tube. The necks are observed to form at the initial thin points only. This is very different from metal rings where the necks along the circumference follow a characteristic short wave length pattern independent of the spacing between the initial thin points. However, a preference towards many closely spaced necks is also found for polymer tubes with the clear distinction particularly for thin tubes that necking is much more pronounced when more initial thin points are added along the quarter of the tube whereas in case of only one thin point in the quarter tube region studied the necking is almost invisible. Some trace of this behaviour is also found for thicker tubes, but it is less pronounced. The position of the necks is apparently locked due to the behaviour of polymers. Also another polymer characteristic such as a switch from neck localization to neck propagation is found in good agreement with experiments carried out by G'Sell and Jonas (1979) and Marquez-Lucero et al. (1989). The results shows that necking is strain rate dependent in the polymer. Finally, as the necks have propagated to the entire tube wall a vibration mode replaces any further tube expansion.

Bulging and neck propagation are investigated for a full three dimensional thin walled polymer tube under different loading conditions. The necks are shown to propagate in both the axial and circumferential directions. In accordance with paper [P1] necks form at locations specified by initial thin points along the circumference of the tube. If the enclosed volume is taken to increase linearly with time, which is in higher agreement with experiments, a pressure maximum is reached and the necks obtain a characteristic sharp edge at the end as was found experimentally by Kyriakides (2007). Also one neck is observed to become finally more dominant than the other necks circumferentially as well axially either through neck propagation or, depending of the number of initial thin points, through coalescence of necks. In case of a single initial thin point along the quarter of the

tube analysed, more neck localization, than that found for the similar 2D case in paper [P1] is observed. But no bulge is seen to form indicating similarity to the results in paper [P1]. These last observations are further presented and discussed in section 3.2, but they are not included in paper [P2].

Studies of a polymer reinforced by transversely staggered fibers in paper [P3] predict the development of a diagonal zone of high shear intensity to develop in the polymer matrix between the stiff overlapping fiber ends. Also, high strain and stress concentrations emerge at the sharp fiber edges. Cases of different transverse to longitudinal strain ratios, different fiber spacings and different fiber thickness are investigated. Furthermore, it is shown that it would have been reasonable to model the embedded E-glass fibers as infinitely stiff when carrying out the numerical analyses. A case of periodicity is analysed, relevant to fiber overlap much longer than the spacing, and a band of elevated shear intensity is observed to appear between the fibers, but no obvious localization into a shear band is found. This appears to be an effect similar to that of neck localization, see paper [P1], where the necks stop thinning down when a certain thickness of the specific neck is reached and a switch to neck propagation occurs. Shear zone propagation takes place as the shear stress within the shear zone increases analogous to the neck propagation found in the papers [P1] and [P2].

Finally, 2D tubes constisting af another polymer than that of papers [P1]-[P3] are studied with respect to necking. Since the polymer investigated, PET, has a wider strain range of softening and thereby a delay in network hardening compared to the polymer used in paper [P1] the single neck observed to develop in the PET tube thins much more down than is the case for the similar tube made of the polymer in paper [P1]. The occurrence of a very thin neck is emphasised by experiments performed by Kyriakides (2007) for PET. Moreover, the experiments from Kyriakides (2007) reveal that the heavily elongated neck obtains extra space through neck bulging instead of the pure tube expansion seen in papers [P1]-[P2]. Due to heavily distorted elements in the neck of the numerical solution, a full 3D numerical analysis demonstrating the development of the bulged neck achieved by Kyriakides (2007) is not carried out. Such an analysis would require remeshing. Instead, a simplified numerical 2D analysis is used to illustrate bulged neck formation like that found in the experiment of Kyriakides (2007). Hence, it must be concluded that the necking mechanism observed depends on the choise of material. A study of a full three dimensional PET tube with respect to bulging of the neck would be a natural continuation of the present investigation.

References

Andrews, M. C., Day, R. J., Patrikis, A. K. and Young, R. J. 1994. Deformation micromechanics in aramid/epoxy composites. *Composites* **25(7)**, 745–751.

Arruda, E. M. and Boyce, M. C. 1993. Evolution of plastic anisotropy in amorphous polymers during finite straining. *Int. J. Plast.* **9**, 697–720.

Belytschko, T., Chiapetta, R. L. and Bartel, H. D. 1976. Efficient large scale non-linear transient analysis by finite elements. *Int. J. Numer. Meths. Engrg.* **10**, 579–596.

Bergstrom, J. S. and Boyce, M. C. 1998. Constitutive modelling of the large strain time dependent behavior of elastomers. *J. Mech. Phys. Solids* **46**, 931–957.

Boyce, M. C. and Arruda, E. M. 1990. An experimental and analytical investigation of the large strain compressive and tensile response of glassy polymers. *Polym. Engng. Sci.* **30**, 1288–1298.

Boyce, M. C., Parks, D. M. and Argon, A. S. 1988. Large inelastic deformation of glassy polymers. part i: rate dependent constitutive model. *Mech. Mater.* **19**, 193–212.

Boyce, M. C., Socrate, S. and Llana, P. G. 2000. Constitutive model for the finite deformation stress–strain behavior of poly(ethylene terephthalate) above the glass transition. *Polymer* **41**, 2183–2201.

Budiansky, B. 1969. Remarks on theories of solid and structural mechanics. *Siam, Philadelphia,* pp. 77–83.

Doi, M. and Edwards, M. F. 1986. The theory of polymer dynamics. *Oxford University Press*.

Fleck, N. A. 1997. Compressive failure of fiber composites. *Advanc. Appl. Mech.* **33**, 43–117.

Gearing, B. P. and Anand, L. 2004. Notch–sensitive fracture of polycarbonate. *Int. J. Solids Struct.* **41**, 827–845.

G'Sell, C. and Jonas, J. J. 1979. Determination of the plastic behaviour of solid polymers at constant true strain rate. *J. Mater. Sci.* **14**, 583–591.

Hampe, A. and Marotzke, C. 1992. Adhesion of polymers to reinforcing fibres. *Polymer Int.* **28**, 313–318.

Han, J.-B. and Tvergaard, V. 1995. Effect of inertia on the necking behaviour of ring specimens under rapid radial expansion. *Eur. J. Mech. A/Solids* **14**, 287–307.

Hutchinson, J. W. 1973. Numerical solution of non–linear structural problems. *Ed. R. F Hartung, AMD, ASME* **6**, 17–29.

Hutchinson, J. W. and Neale, K. W. 1983. Neck propagation. *J. Mech. Phys. Solids* **31(5)**, 405–426.

Hutchinson, J. W., Tennyson, R. C. and Muggeridge, D. B. 1971. Effect of a local axisymmetric imperfection on the buckling behavior of a circular cylindrical shell under axial compression. *AIAA Journal* **9**, 48–52.

Karbhari, V. M. and Wilkins, D. J. 1990. A theoretical model for fiber debonding incorporating both interfacial shear and frictional stresses. *Scripta Metall. Mater.* **24**, 1197–1202.

Kyriakides, S. 2007. Personal communication.

Lai, J. and Van der Giessen, E. 1997. A numerical study of crack-tip plasticity in glassy polymers. *Mech. Mater.* **25**, 183–197.

Larsson, M., Needleman, A., Tvergaard, V. and Storākers, B. 1982. Instability and failure of internal pressurized ductile metal cylinders. *J. Mech. Phys. Solids* **30**, 121–154.

Laws, N. and Dvorak, G. J. 1988. Progressive transverse cracking in composite laminates. *J. Comp. Mater.* **22**, 900–916.

Lindgreen, B., Tvergaard, V. and Needleman, A. 2007. Bulge formation and necking in a polymer tube under dynamic expansion. *Proceedings of the 20th Nordic Seminar on Computational Mechanics*.

Llorca, J., Needleman, A. and Suresh, S. 1991. An analysis of the effects of matrix void growth on deformation and ductility in metal–ceramic composites. *Acta Metall. Mater.* **39(10)**, 2317–2335.

Marquez-Lucero, A., G'Sell, C. and Neale, K. W. 1989. Experimental investigation of neck propagation in polymers. *Polymer* **30(4)**, 636–642.

Mikkelsen, L. P. and Tvergaard, V. 1999. A nonlocal two-dimensional analysis of instabilities in tubes under internal pressure. *J. Mech. Phys. Solids* **47**, 953–969.

Mulliken, A. D. and Boyce, M. C. 2006. Mechanics of the rate-dependent elastic-plastic deformation of glassy polymers from low to high strain rates. *Int. J. Solids Struct.* **43**, 1331–1356.

Niordson, F. I. 1965. A unit for testing materials at high strain rates. *Exp. Mech.* **5**, 29–32.

Peirce, D., Shih, C. F. and Needleman, A. 1984. A tangent modulus method for rate dependent solids. *Comp. Struct.* **18**, 875–887.

Sewell, M. J. 1965. On the calculation of potential functions defined on curved boundaries. *Proc. Roy. Soc. Lond. A* **286**, 402–411.

Sørensen, N. J. and Freund, L. B. 2000. Unstable neck formation in a ductile ring subjected to impulsive radial loading. *Int. J. Solids Structures* **37**, 2265–2283.

Tŭgcu, P. 1996. Inertial effects in ductile failure of cylindrical tubes under internal pressure. *Int. J. Impact Engng* **18(5)**, 539–563.

Tvergaard, V. 1990. Bifurcation in elastic-plastic tubes under internal pressure. *Eur. J. Mech. A/Solids* **9**, 21–35.

Tvergaard, V. 2003. Debonding of short fibres among particulates in a metal matrix composite. *Int. J. Solids Struct.* **40**, 6957–6967.

Tvergaard, V. and Needleman, A. 2008. An analysis of thickness effects in the izod test. *Accepted for publication in Int. J. Solids Structures*.

Wu, P. D. and Van der Giessen, E. 1994. Analysis of shear band propagation in amorphous glassy polymers. *Int. J. Solids Struct.* **31(11)**, 1493–1517.

Wu, P. D. and Van der Giessen, E. 1996. Computational aspects of localized deformations in amorphous glassy polymers. *Eur. J. Mech. A/Solids* **15**, 799–823.

Zhang, H. and Ravi-Chandar, K. 2006. On the dynamics of necking and fragmentation-i.real-time and post-mortem observations in al 6061-o. *Int. J. Frac.* **142**, 183–217.

P1

Dynamic neck development in a polymer tube under internal pressure loading

International Journal of Solids and Structures
45, 580-592, 2008

Available online at www.sciencedirect.com
ScienceDirect
International Journal of Solids and Structures 45 (2008) 580–592
INTERNATIONAL JOURNAL OF SOLIDS AND STRUCTURES
www.elsevier.com/locate/ijsolstr

Dynamic neck development in a polymer tube under internal pressure loading

Britta Lindgreen [a], Viggo Tvergaard [a,*], Alan Needleman [b]

[a] Department of Mechanical Engineering, Solid Mechanics, Technical University of Denmark, DK-2800 Kgs. Lyngby, Denmark
[b] Division of Engineering, Brown University, 182 Hope Street, Providence, RI 02912, USA

Received 3 May 2007; received in revised form 25 July 2007
Available online 26 August 2007

Abstract

The initiation and growth of necks in polymer tubes subjected to rapidly increasing internal pressure is analyzed numerically. Plane strain conditions are assumed to prevail in the axial direction. The polymer is characterized by a finite strain elastic–viscoplastic constitutive relation and the calculations are carried out using a dynamic finite element program. Numerical results for neck development are illustrated and discussed for tubes of various thicknesses. The sensitivity to the wave number of the thickness imperfections is studied with a focus on comparing a long wave length imperfection and a short wave length imperfection. After some thinning down at the necks, the mode of deformation switches to neck propagation along the circumference of the tube. A case is shown in which the necks have propagated along the entire tube wall, so that network locking in the polymer results in high stiffness against further expansion of the tube. The rate dependence of the necking behavior gives noticeable differences in neck development for slow loading versus fast loading.

Keywords: Polymer tubes; Neck propagation; Dynamic loading; Finite strain

1. Introduction

For thin metal rings expanded very rapidly by electromagnetic loading Niordson (1965) has observed many necks around the circumference. Analyses of such dynamical necking in rings triggered by sinusoidal thickness imperfections have been carried out numerically by Han and Tvergaard (1995), Tŭgcu (1996), and Sørensen and Freund (2000). In these numerical studies the necking is initiated at the thin points along the circumference resulting in continued necking down to a point as is typical in metals. The analyses have shown neck development following a short wave length necking pattern even when there is only a long wavelength thickness imperfection along the circumference. This is emphasized in Tŭgcu (1996) where a mode shape with a shorter wave length develops sooner than the one with a longer wavelength and exhibits more pronounced neck formation. A recent very detailed experimental investigation of the multiple neck phenomenon in rapidly

* Corresponding author. Tel.: +45 4525 4273; fax: +45 4593 1475.
E-mail address: viggo@mek.dtu.dk (V. Tvergaard).

0020-7683/$ - see front matter © 2007 Elsevier Ltd. All rights reserved.
doi:10.1016/j.ijsolstr.2007.08.005

expanding metal rings illustrates how the neck evolution results in fragmentation into many separate pieces (Zhang and Ravi-Chandar, 2006).

In cases where the specimen is made of a polymer material a somewhat different necking behavior is observed, characterized by a limited amount of thinning followed by neck propagation along the specimen. This has been investigated experimentally by G'Sell and Jonas (1979) and Marquez-Lucero et al. (1989) who found that a neck localizes at some region of the material and then propagates along the length of a tensile test specimen. It was observed that the onset of necking takes place very near the local load maximum that occurs in the polymer just before softening initiates whereas the continued elongation of the specimen accompanying neck propagation occurs under essentially constant load. When the neck propagation is complete with the neck covering the entire specimen a load increase was observed due to the material hardening in the elongated neck. A theoretical study of neck propagation has been carried out by Hutchinson and Neale (1983). In a numerical investigation, Neale and Tŭgcu (1985) have shown the initiation of necking for circular cylindrical tensile specimens followed by neck propagation around the thin points where the onset of necking occurred.

In the present paper the necking behavior of polymer tubes under dynamic pressure loading is analyzed numerically where the constitutive relation is an incremental elastic–viscoplastic law, used in Tvergaard and Needleman (2007), adopted from Wu and Van der Giessen (1996) and also Boyce et al. (1988), Boyce and Arruda (1990), Arruda and Boyce (1993), Mulliken and Boyce (2006). It is assumed that nonlinear elastic effects can be ignored so that the elastic part is taken to be linear. The finite element analysis is based on a full three dimensional implementation for which plane strain conditions are enforced in this particular case. In a real tube inflation leads to bulging followed by necking, but the plane strain idealization considered here allows the implications of a polymer-like increasing–decreasing–increasing stress–strain response for the necking behavior to be studied. A sinusoidal initial thickness imperfection along the tube circumference is used to trigger the onset of necking. The material parameters used are representative of a polycarbonate for which experimental compression curves are given in Mulliken and Boyce (2006).

2. Problem formulation

The finite element calculations are carried out using a convected coordinate Lagrangian formulation. All field quantities are considered to be functions of convected coordinates, y^i, and time, t. The dynamic principle of virtual work is written as

$$\int_V \tau^{ij}\delta E_{ij}\,\mathrm{d}V = \int_S T^i \delta u_i\,\mathrm{d}S - \int_V \rho\frac{\partial^2 u^i}{\partial t^2}\delta u_i\,\mathrm{d}V \tag{1}$$

with

$$T^i = (\tau^{ij} + \tau^{kj}u^i_{,k})v_j \tag{2}$$

$$E_{ij} = \frac{1}{2}(u_{i,j} + u_{j,i} + u^k_{,i}u_{k,j}) \tag{3}$$

where V and S are the volume and surface of the body in the reference configuration, and $(\,)_{,i}$ denotes covariant differentiation in the reference frame. Also, τ^{ij} are the contravariant components of Kirchhoff stress on the deformed convected coordinate net ($\tau^{ij} = J\sigma^{ij}$, with σ^{ij} being the contravariant components of the Cauchy or true stress and J the ratio of current to reference volume), v_j and u_j are the covariant components of the reference surface normal and displacement vectors, respectively, and ρ is the mass density.

Two polymer tubes are analyzed; a thin one and a thick one. The thin tube has initial wall thickness $h_0 = 0.002$ m and initial mean radius $R_0 = 0.051$ m whereas the thick tube has initial wall thickness $h_0 = 0.01$ m and initial mean radius $R_0 = 0.055$ m. The numerical calculations are carried out for plane strain deformations in the axial direction of the tubes. An internal pressure p increasing linearly with respect to time t is applied on the inner surface of the tubes. The corresponding components of the nominal traction vector T^i on the reference base vectors are given by

$$T^i = -p\alpha^{ir}n_r \qquad \text{for } \{(y^1)^2 + (y^2)^2\}^{1/2} = R_0 - h_0/2 + \Delta h_0 \tag{4}$$

Here the configuration dependent tensor α^{ir} is specified by

$$\alpha^{ir} = \frac{1}{2}\varepsilon^{ijk}\varepsilon^{lmr}(g_{jl} + u_{j,l})(g_{km} + u_{k,m}) \tag{5}$$

with ε^{ijk} as the alternating tensor and n_r as the normal to the inner surface in the reference coordinate system (Sewell, 1965).

An initial sinusoidal thickness imperfection Δh_0 which is similar to that used by Han and Tvergaard (1995) is imposed on both the inner and the outer surfaces of the tube in order to trigger the onset of necking so that the initial wall thickness is $h_0 + 2\Delta h_0$. With the initial mean thickness h_0 of the tube

$$\Delta h_0 = -h_0\xi_n \cos\left(\frac{n\pi\theta}{\theta_0}\right) \tag{6}$$

where θ is defined in Fig. 1 and the thickness inhomogeneity is specified through the amplitude ξ_n. Symmetry about the planes $\theta = 0$ and $\theta = \pi/2$ is assumed here so that analyses need only be carried out for a 90° segment of the tube circumference with symmetry boundary conditions applied. Therefore, the parameter value $\theta_0 = \pi/2$ is chosen.

In the results to be shown subsequently the overall deformation level of the tube is specified either in terms of the relative volume change $\Delta V/V_0$ where V_0 is the initial volume inside the tube and ΔV is current volume change, or in terms of the average logarithmic hoop strain on the inner surface given by

$$\varepsilon_{\mathrm{av}} = \ln\left(\frac{R_i}{R_{i0}}\right) \tag{7}$$

Here R_{i0} is initial inner radius of the tube cross section with no imperfection and R_i is calculated as the average inner radius based on current volume V, if the cross section of the tube remained circular during deformation, i.e.,

$$R_i = \sqrt{\frac{V}{\pi L}} \tag{8}$$

where L is the length of the tube.

Although only plane strain calculations are carried out, the finite element code is based on a full three dimensional implementation. The plane strain condition is met by using one element in the out-of-plane direction and enforcing a zero displacement condition on the out-of-plane faces. Twenty node brick elements are used with eight point integration for the force term, the left hand side of Eq. (1), and 27 point integration for the mass matrix, the last term on the right hand side of Eq. (1). A lumped mass matrix is used, Krieg and Key (1973), and time integration is carried out using the Newmark β-method with $\beta = 0$, Belytschko et al. (1976).

2.1. Constitutive relation

The constitutive relation used in the calculations is that in Tvergaard and Needleman (2007) and is adopted from Wu and Van der Giessen (1996) which, in turn, is based on models proposed by Boyce and co-workers

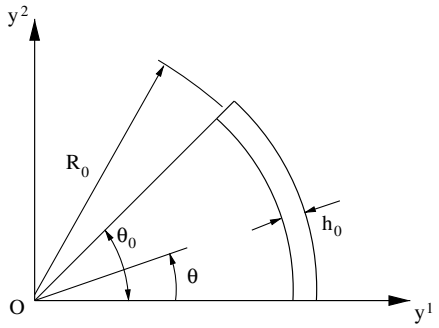

Fig. 1. A segment of a tube specimen specified by the initial mean radius R_0, the initial mean thickness h_0 and the angle θ_0.

(Boyce et al., 1988; Boyce and Arruda, 1990; Arruda and Boyce, 1993; Mulliken and Boyce, 2006). As in Tvergaard and Needleman (2007), attention is confined to an eight chain model, Arruda and Boyce (1993). The elastic part of the response is taken to be governed by a linear hypoelastic relation so that nonlinear elastic effects are neglected. Furthermore, the distinction between the Cauchy stress $\boldsymbol{\sigma}$ and the Kirchhoff stress $\boldsymbol{\tau}$ is ignored.

The rate of deformation tensor is written as

$$\boldsymbol{D} = \boldsymbol{D}^{\mathrm{e}} + \boldsymbol{D}^{\mathrm{p}} \tag{9}$$

where

$$\boldsymbol{D}^{\mathrm{e}} = \boldsymbol{L}^{-1} \cdot \hat{\boldsymbol{\sigma}} \tag{10}$$

with $\boldsymbol{L}$, the isotropic tensor of moduli with elastic constants Young's modulus E and Poisson's ratio ν and

$$\boldsymbol{D}^{\mathrm{p}} = \dot{\gamma}^{\mathrm{p}} \boldsymbol{p} \tag{11}$$

with

$$\dot{\gamma}^{\mathrm{p}} = \dot{\gamma}_0 \exp\left[-\frac{\Delta G}{kT}\left\{1 - \left(\frac{\tau}{s - \alpha(\mathrm{tr}\boldsymbol{\sigma})/3}\right)^m\right\}\right] - \dot{\gamma}_0 \exp\left[-\frac{\Delta G}{kT}\right] \tag{12}$$

Here, m, $\dot{\gamma}_0$, ΔG, and α are material constants, T is the temperature (Kelvin) and k is Boltzmann's constant $k = 1.38$ J/K. The last term in Eq. (12) is included so that $\dot{\gamma}^{\mathrm{p}} = 0$ when $\tau = 0$. Also,

$$\boldsymbol{p} = \frac{\boldsymbol{\sigma}' - \boldsymbol{b}'}{\sqrt{2}\tau} \qquad \tau = \sqrt{\frac{1}{2}(\boldsymbol{\sigma}' - \boldsymbol{b}') : (\boldsymbol{\sigma}' - \boldsymbol{b}')} \tag{13}$$

with $()'$ denoting deviatoric quantities.

The hardness s in Eq. (12) is taken to have the initial value s_0 and to evolve as

$$\dot{s} = h\left(1 - \frac{s}{s_{ss}}\right)\dot{\gamma}^{\mathrm{p}} \tag{14}$$

with h and s_{ss} material constants.

For the eight chain model, Arruda and Boyce (1993),

$$\boldsymbol{b} = \frac{1}{3} C_R \sqrt{N} \frac{\beta_c}{\lambda_c} \boldsymbol{B} \tag{15}$$

where $\boldsymbol{B} = \boldsymbol{F} \cdot \boldsymbol{F}^{\mathrm{T}}$, ($\boldsymbol{F}$ is the deformation gradient), C_R and $\sqrt{N}$ are specified material constants and

$$\lambda_c^2 = \frac{1}{3}\mathrm{tr}\,\boldsymbol{B} \qquad \beta_c = \mathcal{L}^{-1}\left(\frac{\lambda_c}{\sqrt{N}}\right) \tag{16}$$

with

$$\mathcal{L}(x) = \coth(x) - \frac{1}{x} \tag{17}$$

Standard kinematical relations are used to obtain an expression for the convected rate of the contravariant components of Kirchhoff stress appearing in the principle of virtual work Eq. (1). In order to increase the stable time step while still using an explicit stress update, the rate tangent approach of Peirce et al. (1984) is used. Also, when λ_c approaches the limit stretch $\lambda_{\max} = \sqrt{N}$, the hardening rate provided by the increased network stiffness grows very large, thus effectively suppressing all further plastic flow. As in Lai and Van der Giessen (1997), we disable viscoplastic flow ($\dot{\gamma}^{\mathrm{p}} = 0$) when λ_c exceeds $r\lambda_{\max}$, and here choose $r = 0.93$.

In the numerical analyses the time step Δt is controlled so that the plastic strain increment $\dot{\gamma}^{\mathrm{p}}\Delta t$ never exceeds a specified value $\Delta\gamma$, which is generally taken to be $\Delta\gamma = 0.000004$.

3. Results

Calculations are carried out for material properties representative of polycarbonate (PC) with Young's modulus $E = 1814.6$ MPa, $\nu = 0.38$, density $\rho = 1300$ kg/m^3, temperature $T = 298$ K, $\Delta G = 0.374 \times 10^{-18}$ J, $\dot{\gamma}_0 = 0.894 \times 10^4$ s^{-1}, $m = 0.20$, $C_r = 12.6$ MPa, $N = 2.30$ and the softening parameters $\alpha = 0.08$, $s_0 = 81.65$ MPa, $s_{ss} = 22.71$ MPa, $h = 50.0$ MPa.

First a thin walled ($h_0 = 0.002$ m) tube is analyzed with $h_0/R_0 = 0.0392$. Here the thickness inhomogeneity, Eq. (6) is specified by the wave number $n = 5$ and the amplitude $\xi_5 = 0.001$. Fig. 2 shows the evolution of the three necks that initiate in the segment analyzed due to the chosen imperfection and the corresponding contours of plastic strain γ^p. The calculations are carried out for a finite element mesh consisting of two elements through the thickness and 160 elements along the circumference. From Fig. 2a the necks are fully formed at the hoop strain $\varepsilon_{av} = 0.160$ and Fig. 2b and c illustrates how neck propagation occurs as the pressure and the average hoop strain increase. Neck propagation occurs at all three points where the onset of necking initiated due to the chosen initial imperfection. In earlier studies for metal rings under rapid expansion (Han and Tvergaard, 1995; Sørensen and Freund, 2000) a larger number of necks were found and necks also developed at points where there was no initial thickness inhomogeneity. For metals deformation localizes in the necks. On the other hand, here necking initially reduces the thickness somewhat, but subsequently the necks propagate along the circumference of the tube. Neck propagation is a characteristic behavior for polymers as observed in tension.

The difference between three finite element mesh refinements is shown in Fig. 3. Fig. 3a shows curves of applied pressure, p, normalized by the initial hardness s_0, versus the change in tube volume, ΔV, normalized by the initial volume inside the tube V_0; Fig. 3b shows the evolution of the normalized thickness, h/h_0 at 0° and 90° versus the average hoop strain, ε_{av}, defined by Eq. (7); and Fig. 3c shows curves of the average hoop strain rate $\dot{\varepsilon}_{av}$ versus the normalized volume change $\Delta V/V_0$. The crudest mesh consists of one element through the thickness and 80 elements along the circumference and the intermediate mesh (which is the mesh used for the

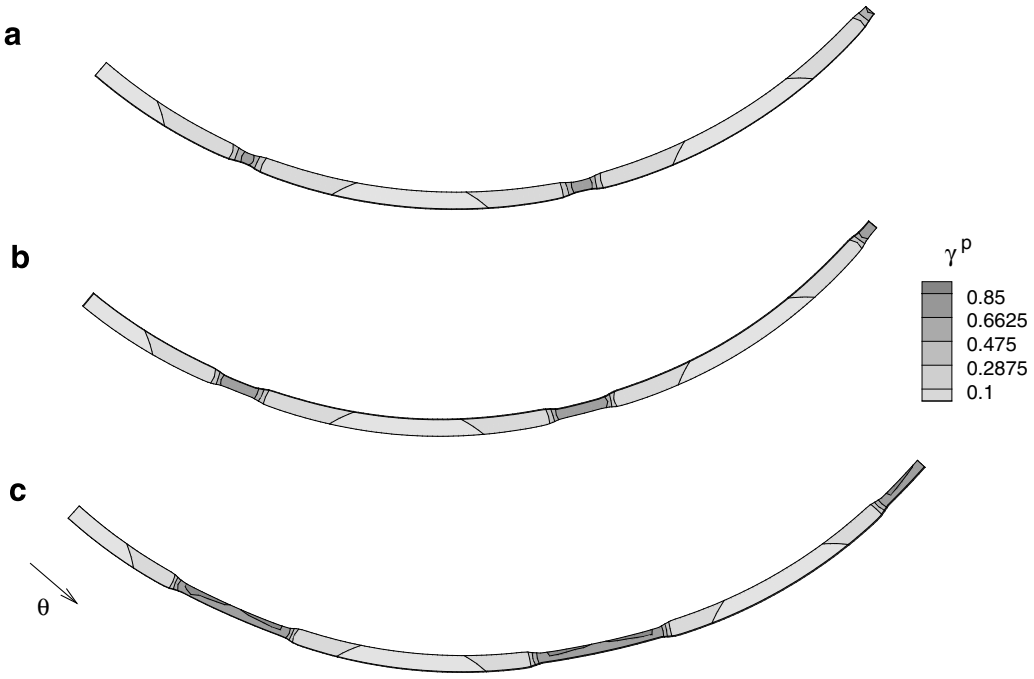

Fig. 2. Contours of effective plastic strain γ^p in the deformed configuration for a thin walled tube with $h_0 = 0.002$ m and $h_0/R_0 = 0.0392$ and with an imperfection having $n = 5$ and $\xi_5 = 0.001$. Only the segment analyzed numerically is shown and θ increases from 0° to 90° in the direction shown. The applied pressure rate is $\dot{p} = 411.7$ MPa/s. There are two elements through the thickness and 160 along the circumference. The average logarithmic hoop strain, ε_{av}, is: (a) $\varepsilon_{av} = 0.160$, (b) $\varepsilon_{av} = 0.194$, (c) $\varepsilon_{av} = 0.286$.

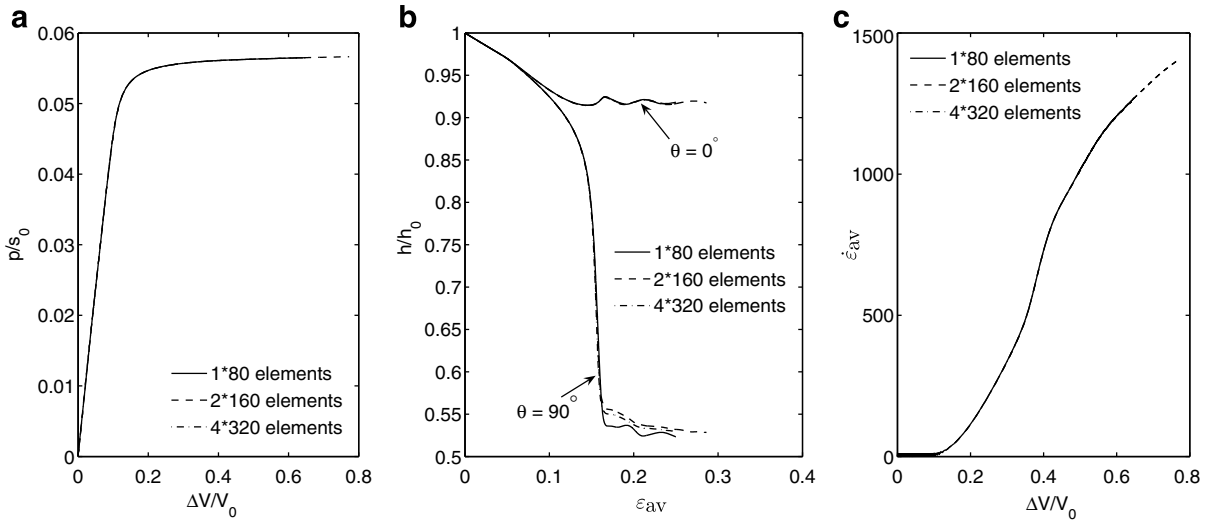

Fig. 3. The response of a thin walled tube with $h_0 = 0.002$ m, $h_0/R_0 = 0.0392$, $n = 5$, $\xi_5 = 0.001$, and $\dot{p} = 411.7$ MPa/s using various finite element discretizations. (a) Normalized applied pressure, p/s_0, versus the normalized interior volume change of the tube, $\Delta V/V_0$. (b) Thickness changes at 0° and at 90° versus average hoop strain ε_{av}, see Eq. (7). (c) Average hoop strain rate, $\dot{\varepsilon}_{av}$ versus the normalized interior volume change of the tube, $\Delta V/V_0$.

calculations in Fig. 2) has two elements through the thickness and 160 elements along the circumference. The finest mesh consists of four elements through the thickness and 320 elements along the circumference. The pressure versus volume change response in Fig. 3a is unaffected by the mesh refinement and the same is true for the strain rate versus volume change relation in Fig. 3c. The thickness change in Fig. 3b is slightly influenced by the degree of mesh refinement as the neck propagates, especially at the 90° position where there is a neck. Since the difference in results for the 2×160 finite element mesh and the 4×320 finite element mesh is small, we conclude that the 2×160 finite element mesh is sufficient to give accurate results. This discretization will be used for the thin walled tubes in the calculations reported subsequently.

The curves in Fig. 3 pertain to the case for which contour plots are shown in Fig. 2. In Fig. 3a the pressure first increases linearly with the volume expansion in the elastic range, but then in the plastic range the volume grows very rapidly so that the pressure appears to be nearly constant even though it is increasing linearly with time at the specified rate $\dot{p} = 411.7$ MPa/s. Fig. 3b shows the rapid decrease in wall thickness associated with neck development at 90° whereas at 0°, where no neck develops, there is only some decrease in thickness arising from the Poisson effect. The value of the wall thickness, h, oscillates somewhat after the onset of neck propagation. The variation of the average hoop strain rate $\dot{\varepsilon}_{av}$ with the normalized change in volume $\Delta V/V_0$ is shown in Fig. 3c.

Fig. 4 shows the effect of the prescribed pressure rate, $\dot{p}$, for the response of the thin walled tube ($h_0 = 0.002$ m) with $n = 5$ and $\xi_5 = 0.001$ (see Eq. (6)) also shown in Figs. 2 and 3. In Fig. 4a the tube expansion in the plastic range still occurs at an almost constant pressure starting from when necking initiates, with the pressure level highest for the greatest pressure rate $\dot{p} = 4117$ MPa/s and lowest for the smallest pressure rate $\dot{p} = 41.17$ MPa/s. The average hoop strain rate, $\dot{\varepsilon}_{av}$, increases with increasing applied pressure rate $\dot{p}$, see Fig. 4c. Fig. 4b shows that at 0°, where no neck is present, the thickness decreases until necks start to develop at other locations along the circumference. This leads to a brief thickness increase at 0°, but subsequently the thickness remains rather constant there with small oscillations that decay as the necks propagate. The brief increase of wall thickness at 0° occurs as a consequence of neck development elsewhere along the tube circumference. At 90°, where a neck is present, the bump on the curve for the lowest pressure rate $\dot{p} = 41.17$ MPa/s is associated with a dominating neck developing next to the neck at 90°. For $\dot{p} = 41.17$ MPa/s the neck next to the 90° neck is more dominant than the other two necks in the segment analyzed even though the thickness imperfection magnitude is the same at all three locations. For $\dot{p} = 411.7$ MPa/s the neck next to that at 90° is still slightly more dominant (this can be seen in Fig. 2a and b). With $\dot{p} = 4117$ MPa/s the necks are of almost equal size.

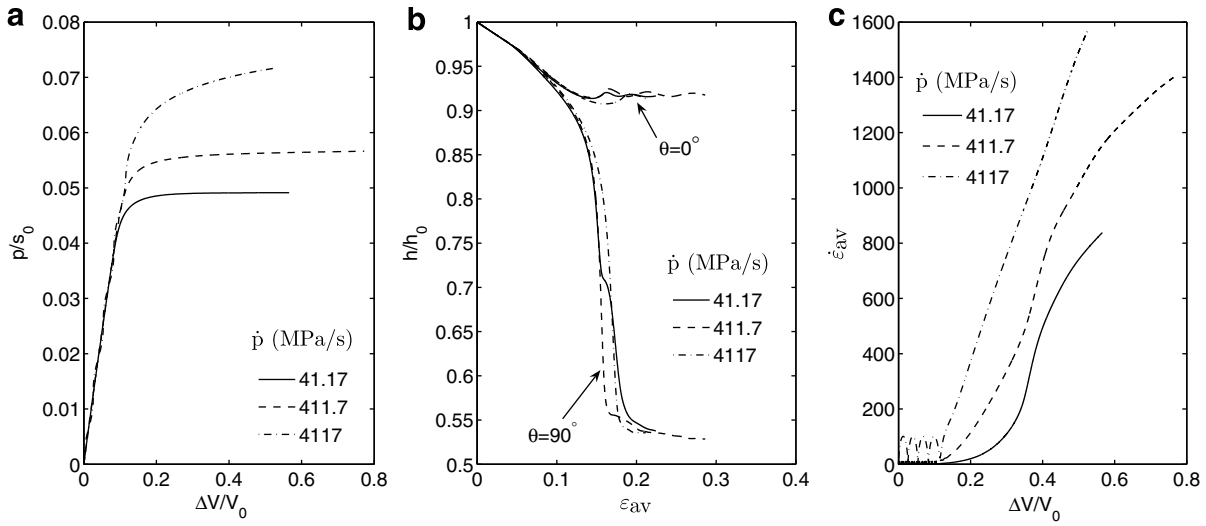

Fig. 4. The response of a thin walled tube with $h_0 = 0.002$ m, $h_0/R_0 = 0.0392$, $n = 5$, and $\xi_5 = 0.001$ subject to various pressure rates. (a) Normalized applied pressure, p/s_0, versus the normalized interior volume change of the tube, $\Delta V/V_0$. (b) Thickness changes at 0° and at 90° versus average hoop strain ε_{av}, see Eq. (7). (c) Average hoop strain rate, $\dot{\varepsilon}_{av}$ versus the normalized interior volume change of the tube, $\Delta V/V_0$.

The case considered in Fig. 5 is identical to that in Figs. 2–4 except for the imperfection which is now specified by $n = 1$ and $\xi_1 = 0.001$, which gives rise to only one thinner point at 90°. As in Figs. 2–4 the applied pressure rate is $\dot{p} = 411.7$ MPa/s. The necking in Fig. 5 is almost invisible in contrast to the earlier situation in Fig. 2 where three initial thin points lead to a clearly visible necking pattern. In Fig. 6 the influence of the applied pressure rate is illustrated for the tube shown in Fig. 5. Fig. 6b shows that the extent of necking is strongly strain rate dependent in this case. For the lowest pressure rate, $\dot{p} = 41.17$ MPa/s, the lower curve showing the thickness change at 90° looks similar to the necking curve in Fig. 4. However, the upper curve in Fig. 6b, showing the evolution of the thickness at 0°, shows that the thickness at 0° also decays after the onset of necking. For $\dot{p} = 411.7$ MPa/s and $\dot{p} = 41.17$ MPa/s the difference between the rate of thinning at 0° and at 90° is smaller. Indeed, for the highest pressure rate $\dot{p} = 4117$ MPa/s there is little difference between the rate of thinning of these two points. Previous results for the necking of metal rings during rapid extension (Sørensen and Freund, 2000; Tŭgcu, 1996) show that necks develop at several locations in a short wavelength mode, whereas a situation with few necks is not found. The results here indicate that polymer tubes may also prefer to neck at several locations in a short wavelength mode when a dynamically increasing internal pressure is applied. This possibility is investigated in the next example where a shorter wavelength imperfection is specified.

In Fig. 7 the initial imperfection is specified by $n = 9$ and $\xi_9 = 0.001$. The contours of plastic strain, γ^p, as well as the neck propagation during the expansion of the thin walled tube is illustrated for the prescribed pressure rate $\dot{p} = 411.7$ MPa/s. As for the imperfection with $n = 5$ and $\xi_5 = 0.001$ a well developed necking pattern appears. Fig. 8b shows that the degree of short wavelength necking at the initial thin points is rather rate independent, which supports the idea that also polymer tubes are more likely to follow a short wavelength necking pattern, as has been found for metal tubes. From Fig. 8b it is noticed that for $\dot{p} = 41.17$ MPa/s there is a bump on the curve describing the thickness decrease at 90° as was also found with $n = 5$ and $\xi_5 = 0.001$ in Fig. 4. Also here the bump emerges due to the fact that a more dominant neck has developed in another location along the circumference. The thickness at 0°, where there is no neck, oscillates a little bit after necking has initiated and propagated at other locations, but otherwise stays constant as was also found for $n = 5$ and $\xi_5 = 0.001$ in Fig. 4.

The situation considered in Fig. 9 is identical to that in Figs. 2 and 3, but the pressure loading is continued for a longer time so that a much larger volume expansion and a larger hoop strain are achieved. After the necks have propagated throughout the entire tube the stretching grows so large that increased network stiffness effectively suppresses further plastic flow. A cut-off value of $r = 0.93$ is implemented, as described in Section 2, so that afterwards the instantaneous response is fully elastic. Due to this network hardening effect

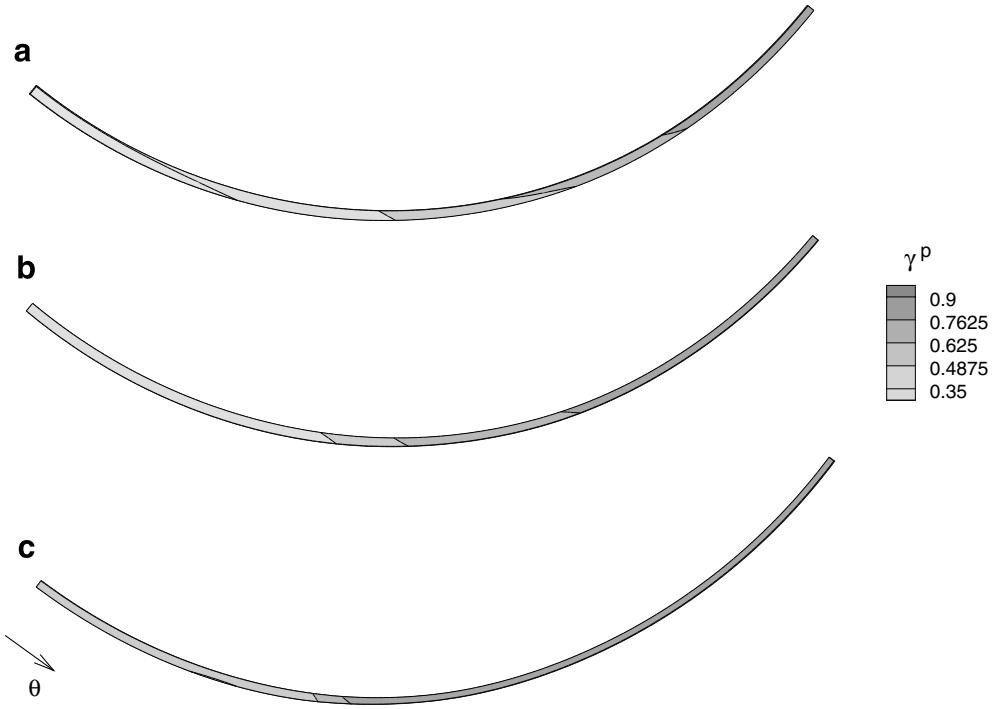

Fig. 5. Contours of effective plastic strain γ^{p} in the deformed configuration for a thin walled tube with $h_0 = 0.002$ m and $h_0/R_0 = 0.0392$ and with an imperfection having $n = 1$ and $\xi_1 = 0.001$. Only the segment analyzed numerically is shown and θ increases from 0° to 90° in the direction shown. The applied pressure rate is $\dot{p} = 411.7$ MPa/s. There are two elements through the thickness and 160 along the circumference. The average logarithmic hoop strain, ε_{av}, is: (a) $\varepsilon_{av} = 0.449$, (b) $\varepsilon_{av} = 0.505$, (c) $\varepsilon_{av} = 0.624$.

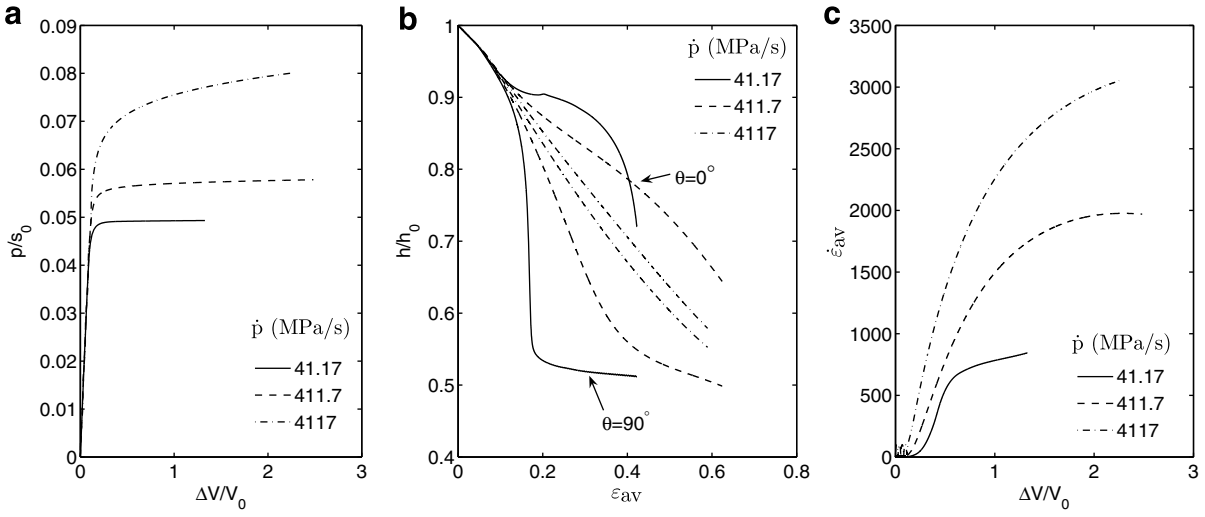

Fig. 6. The response of a thin walled tube with $h_0 = 0.002$ m, $h_0/R_0 = 0.0392$, $n = 1$, and $\xi_1 = 0.001$ subject to various pressure rates. (a) Normalized applied pressure, p/s_0, versus the normalized interior volume change of the tube, $\Delta V/V_0$. (b) Thickness changes at 0° and at 90° versus average hoop strain ε_{av}, see Eq. (7). (c) Average hoop strain rate, $\dot{\varepsilon}_{av}$ versus the normalized interior volume change of the tube, $\Delta V/V_0$.

resulting in high stiffness against further expansion of the tube, the applied pressure suddenly increases as seen in Fig. 9a and a dynamic mode is taking over causing elastic vibrations in the volume change and in the hoop strain as the pressure grows. This is also observed from Fig. 9b where the wall thickness h at 0° suddenly

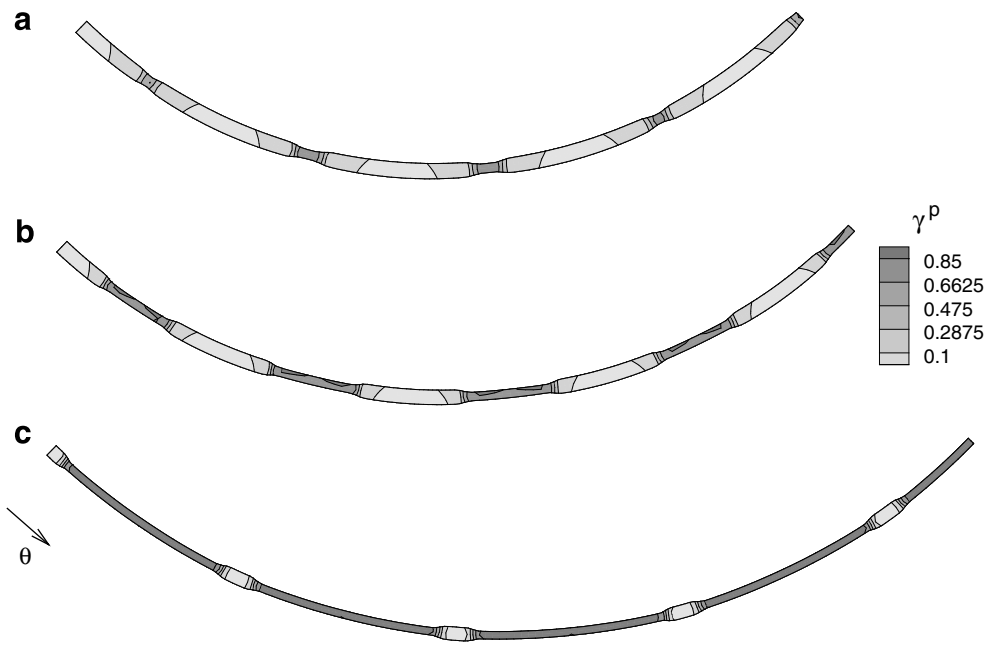

Fig. 7. Contours of effective plastic strain γ^{p} in the deformed configuration for a thin walled tube with $h_0 = 0.002$ m and $h_0/R_0 = 0.0392$ and with an imperfection having $n = 9$ and $\xi_9 = 0.001$. Only the segment analyzed numerically is shown and θ increases from 0° to 90° in the direction shown. The applied pressure rate is $\dot{p} = 411.7$ MPa/s. There are two elements through the thickness and 160 along the circumference. The average logarithmic hoop strain, ε_{av}, is: (a) $\varepsilon_{av} = 0.180$, (b) $\varepsilon_{av} = 0.330$, (c) $\varepsilon_{av} = 0.588$.

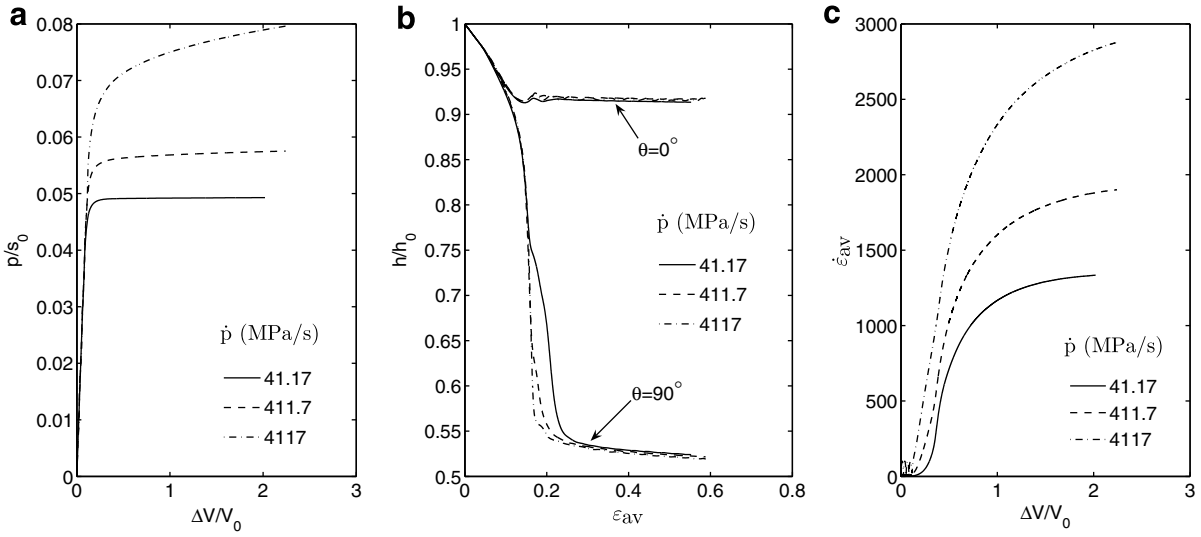

Fig. 8. The response of a thin walled tube with $h_0 = 0.002$ m, $h_0/R_0 = 0.0392$, $n = 9$, and $\xi_9 = 0.001$ subject to various pressure rates. (a) Normalized applied pressure, p/s_0, versus the normalized interior volume change of the tube, $\Delta V/V_0$. (b) Thickness changes at 0° and at 90° versus average hoop strain ε_{av}, see Eq. (7). (c) Average hoop strain rate, $\dot{\varepsilon}_{av}$ versus the normalized interior volume change of the tube, $\Delta V/V_0$.

decreases to the wall thickness at 90° as the neck propagation reaches the 0° point and the hardening results in vibrations. Also Fig. 9c illustrates the dynamic mode of oscillating average strain rate initiated as the network hardening takes over. The vibration frequency in Fig. 9c depends on the hardening behavior of the material. Since the cut-off changes the hardening from elastic–plastic to purely elastic the frequency in Fig. 9c is not

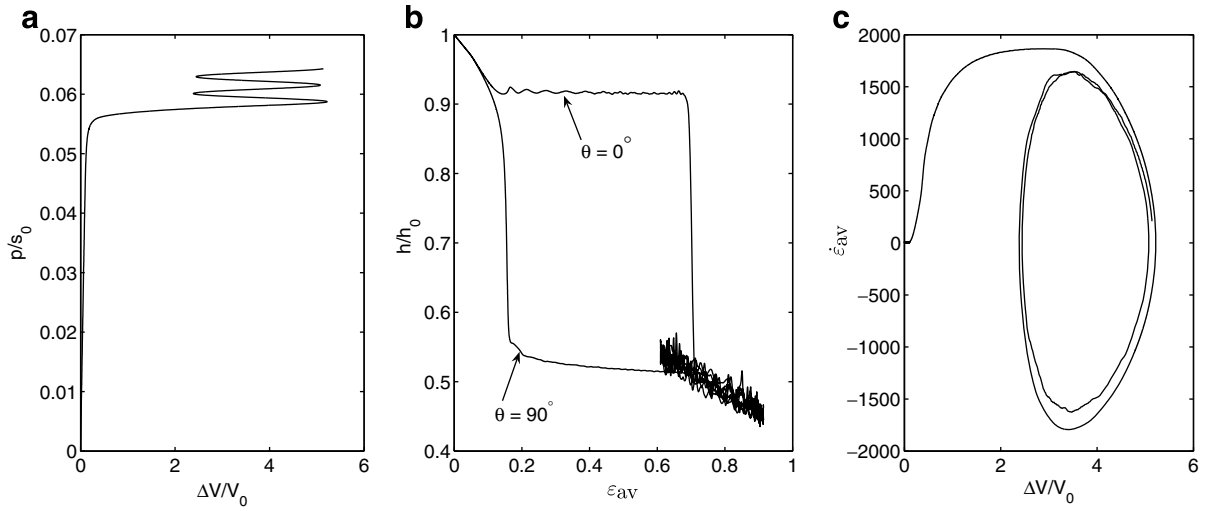

Fig. 9. The response of a thin walled tube with $h_0 = 0.002$ m, $h_0/R_0 = 0.0392$, $n = 5$, $\xi_5 = 0.001$, and $\dot{p} = 411.7$. (a) Normalized applied pressure, p/s_0, versus the normalized interior volume change of the tube, $\Delta V/V_0$. (b) Thickness changes at 0° and at 90° versus average hoop strain ε_{av}, see Eq. (7). (c) Average hoop strain rate, $\dot{\varepsilon}_{av}$ versus the normalized interior volume change of the tube, $\Delta V/V_0$.

realistic, as it depends on the elastic characteristics used to replace the actual network hardening in the polymer.

A thick walled tube is analyzed with thickness $h_0 = 0.01$ m and $h_0/R_0 = 0.182$. The applied pressure rate is $\dot{p} = 823.4$ MPa/s and the thickness imperfection is specified by $n = 1$ with the amplitude $\xi_1 = 0.01$. Contours of plastic strain, γ^p, as well as the neck propagation are shown in Fig. 10. The necking shown is clearly visible

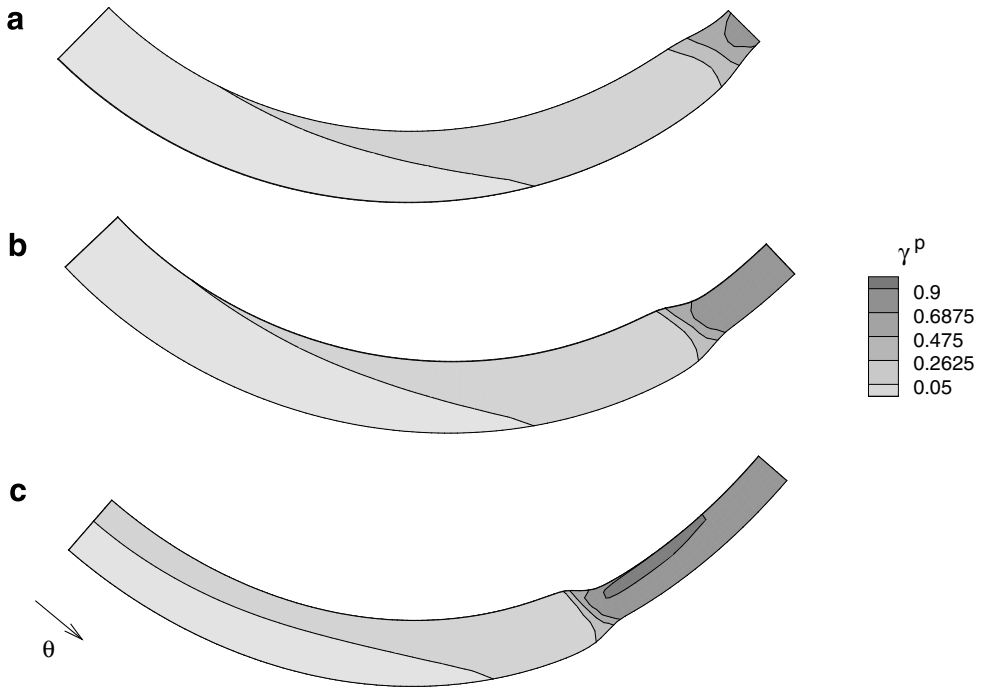

Fig. 10. Contours of effective plastic strain γ^p in the deformed configuration for a thick walled tube with $h_0 = 0.01$ m and $h_0/R_0 = 0.182$ and with an imperfection having $n = 1$ and $\xi_1 = 0.01$. Only the segment analyzed numerically is shown and θ increases from 0° to 90° in the direction shown. The applied pressure rate is $\dot{p} = 823.4$ MPa/s. There are six elements through the thickness and 120 along the circumference. The average logarithmic hoop strain, ε_{av}, is: (a) $\varepsilon_{av} = 0.133$, (b) $\varepsilon_{av} = 0.178$, (c) $\varepsilon_{av} = 0.271$.

compared to earlier cases where thin walled tubes were considered. Especially in the case of the corresponding imperfection with $n = 1$ the thin walled tube in Fig. 5 did not show a well developed short wave length necking, even when the pressure was applied slowly. The well developed necking pattern with the initial necking followed by neck propagation is illustrated in Fig. 11b. A bump on the curve for 0° occurs where neck propagation initiates. As observed in the earlier cases, the pressure in Fig. 11a increases linearly with respect to

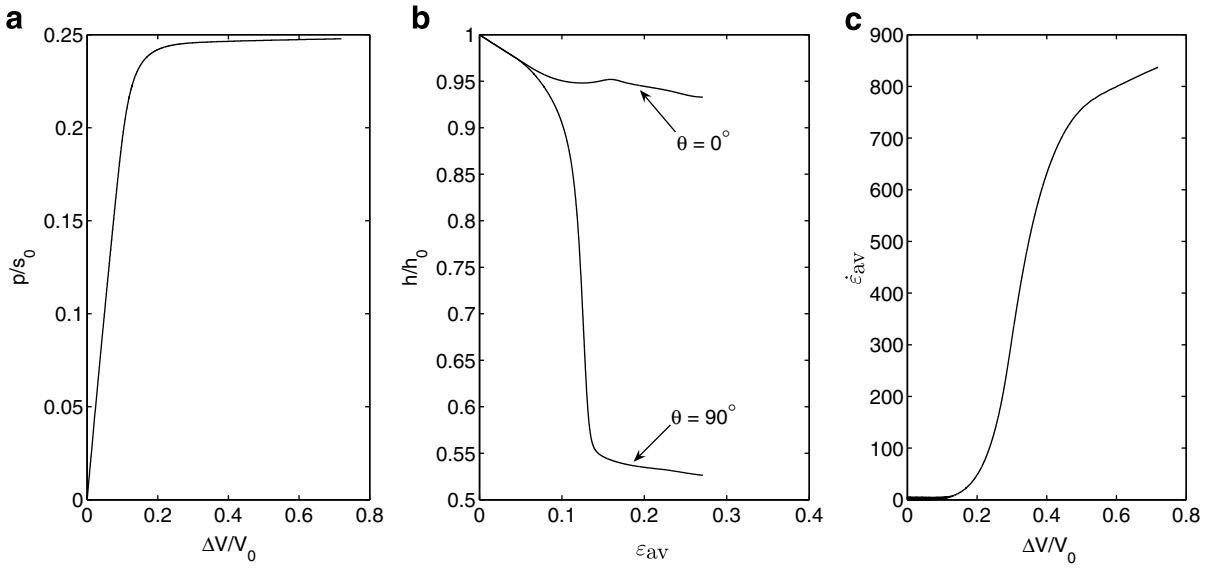

Fig. 11. The response of a thick walled tube with $h_0 = 0.01$ m, $h_0/R_0 = 0.182$, $n = 1$, $\xi_1 = 0.01$, and $\dot{p} = 823.4$. (a) Normalized applied pressure, p/s_0, versus the normalized interior volume change of the tube, $\Delta V/V_0$. (b) Thickness changes at 0° and at 90° versus average hoop strain ε_{av}, see Eq. (7). (c) Average hoop strain rate, $\dot{\varepsilon}_{av}$ versus the normalized interior volume change of the tube, $\Delta V/V_0$.

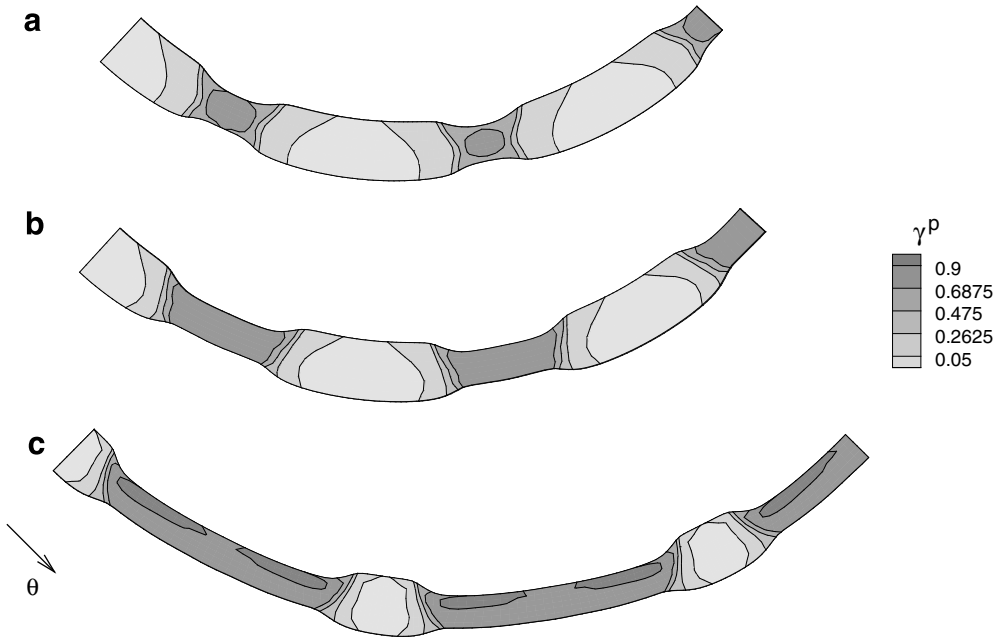

Fig. 12. Contours of effective plastic strain γ^p in the deformed configuration for a thick walled tube with $h_0 = 0.01$ m and $h_0/R_0 = 0.182$ and with an imperfection having $n = 5$ and $\xi_5 = 0.01$. Only the segment analyzed numerically is shown and θ increases from 0° to 90° in the direction shown. The applied pressure rate is $\dot{p} = 823.4$ MPa/s. There are six elements through the thickness and 120 along the circumference. The average logarithmic hoop strain, ε_{av}, is: (a) $\varepsilon_{av} = 0.224$, (b) $\varepsilon_{av} = 0.335$, (c) $\varepsilon_{av} = 0.558$.

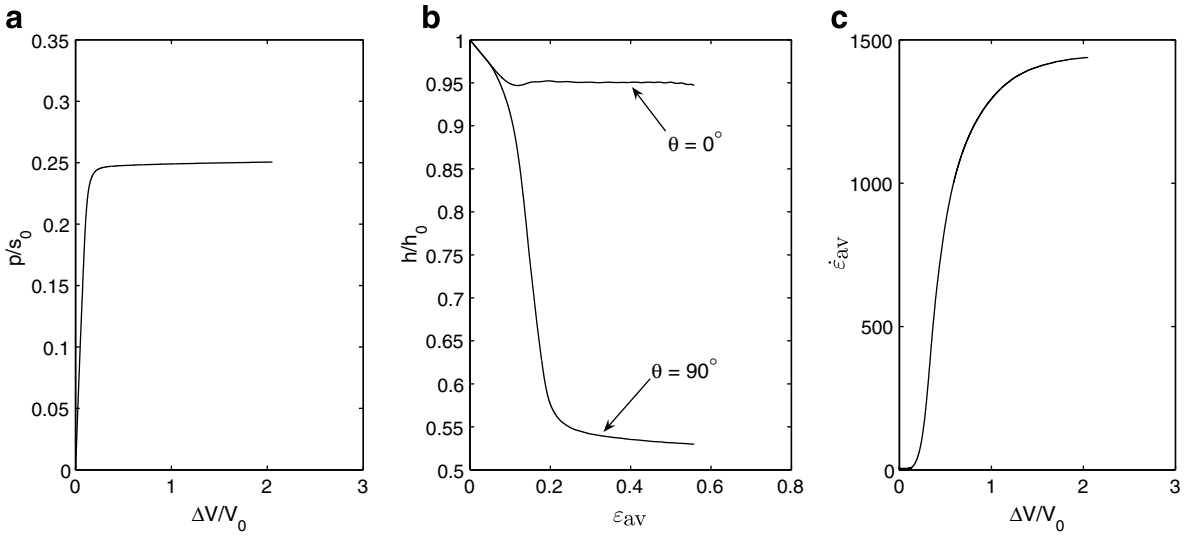

Fig. 13. The response of a thick walled tube with $h_0 = 0.01$ m, $h_0/R_0 = 0.182$, $n = 5$, $\xi_5 = 0.01$, and $\dot{p} = 823.4$. (a) Normalized applied pressure, p/s_0, versus the normalized interior volume change of the tube, $\Delta V/V_0$. (b) Thickness changes at 0° and at 90° versus average hoop strain ε_{av}, see Eq. (7). (c) Average hoop strain rate, $\dot{\varepsilon}_{av}$ versus the normalized interior volume change of the tube, $\Delta V/V_0$.

volume expansion until the volume grows so rapidly that the pressure appears to be almost constant, even though it still increases linearly with time. This is emphasized in Fig. 11c where the circumferential strain rate $\dot{\varepsilon}_{av}$ increases rapidly when the rapid expansion occurs in Fig. 11a.

Fig. 12 shows contours of plastic strain for a tube identical to that in Figs. 10 and 11, but with an imperfection defined by $n = 5$ and $\xi_5 = 0.01$. As for the imperfection $\xi_1 = 0.01$ a clearly developed necking pattern emerges. Fig. 13 shows no large deviation compared to the earlier studies, but the thickness at 0° stays nearly constant in Fig. 13b after the onset of necking, while that in Fig. 11b decays a little, thus retaining some trace of the difference between Figs. 4b and 6b.

4. Discussion

For metal rings under rapid radial expansion both experiments (Niordson, 1965; Zhang and Ravi-Chandar, 2006) and analyses (Han and Tvergaard, 1995; Sørensen and Freund, 2000) have shown a tendency to form many necks along the circumference so that finally the rings will burst into many small pieces. The metal ring analyses have shown that the occurrence of these many necks does not require an initial imperfection with a corresponding short wave pattern. Thus, for the metal rings a characteristic neck spacing tends to develop, rather independent of the wave length of the initial imperfection. The many neck mode is promoted by the fact that closely spaced necks avoid large accelerations in the circumferential direction during the rapid ring expansion.

Also the present analyses of polymer rings under rapid expansion due to an internal pressure show the occurrence of many necks along the circumference, but in the cases analyzed the necks have only been found at points where the initial imperfection had a thin point. In the metal rings the close spacing between necks is determined during the early stage of necking, and thus does not depend on the final failure process in the metal rings. Therefore, the different behavior of the polymers is expected to depend mainly on the shape of the stress strain curve in uniaxial tension, where necking initiates at a sharp stress peak after which significant material softening takes place. Apparently, this softening behavior locks the position of the necks and it seems less easy for the material to form additional necks once some points have passed the sharp stress peak. However, for the thin walled tube the results for one, three or five necks on one quarter of the tube clearly show that the higher number of necks would develop more rapidly if allowed for by the initial imperfection. This is particularly clear for the highest rate of loading considered. The results for a more thick walled tube in Figs. 10–13 show

less dependence on the number of necks around the circumference, but still the tube with only one neck in the region analyzed shows some trace of the behavior found for the corresponding thin walled tube.

The phenomenon of neck propagation gives a major difference between the polymer tubes analyzed here and the metal rings considered in earlier papers. Just after the onset of necking tube contours of plastic strain such as those in Fig. 7a are very similar to results found for metal tubes, but then neck propagation evolves in the polymer tubes, whereas the localized necks in metal rings continue thinning, leading to ring fragmentation. The cause of the neck propagation is that strongly increased network stiffness occurs in the polymer when the stretch approaches a material dependent limit stretch, and therefore the material in the thinner parts of the ring, inside the propagating necks, have reached a high stiffness. Ultimately, in the polymer tube, the necks will have propagated all over the tube wall, as illustrated in Fig. 9, and subsequently the network stiffness grows very large with little extra straining so that the tube expansion stops, being replaced by an elastic vibration mode. The final fracture of the polymer tubes is not modeled in the present analyses.

It should be noted that the polycarbonate experiments of Mulliken and Boyce (2006) were carried out in compression. Under tensile load polycarbonate tends to fail before large plastic strains have occurred (e.g., see Gearing and Anand, 2004). Therefore, the present studies of necking in an inflated ring focus generally on the implications of a polymer-like increasing–decreasing–increasing stress–strain response rather than on the response of a particular polycarbonate.

The assumption of an internal pressure increasing linearly with time is special and may not be easy to realize in practice. But it is expected that this type of loading and the comparison of different loading rates does give a good parametric understanding of the behavior of ductile polymer tubes under rapid expansion.

References

Arruda, E.M., Boyce, M.C., 1993. Evolution of plastic anisotropy in amorphous polymers during finite straining. Int. J. Plast. 9, 697–720.

Belytschko, T., Chiapetta, R.L., Bartel, H.D., 1976. Efficient large scale non-linear transient analysis by finite elements. Int. J. Numer. Methods Eng. 10, 579–596.

Boyce, M.C., Arruda, E.M., 1990. An experimental and analytical investigation of the large strain compressive and tensile response of glassy polymers. Polym. Eng. Sci. 30, 1288–1298.

Boyce, M.C., Parks, D.M., Argon, A.S., 1988. Large inelastic deformation of glassy polymers. Part I: Rate dependent constitutive model. Mech. Mater. 19, 193–212.

Gearing, B.P., Anand, L., 2004. Notch–sensitive fracture of polycarbonate. Int. J. Solids Struct. 41, 827–845.

G'Sell, C., Jonas, J.J., 1979. Determination of the plastic behaviour of solid polymers at constant true strain rate. J. Mater. Sci. 14, 583–591.

Han, J.-B., Tvergaard, V., 1995. Effect of inertia on the necking behaviour of ring specimens under rapid radial expansion. Eur. J. Mech. A/Solids 14, 287–307.

Hutchinson, J.W., Neale, K.W., 1983. Neck propagation. J. Mech. Phys. Solids 31 (5), 405–426.

Krieg, R.O., Key, S.W., 1973. Transient shell response by numerical time integration. Int. J. Numer. Methods Eng. 7, 273–286.

Lai, J., Van der Giessen, E., 1997. A numerical study of crack-tip plasticity in glassy polymers. Mech. Mater. 25, 183–197.

Marquez-Lucero, A., G'Sell, C., Neale, K.W., 1989. Experimental investigation of neck propagation in polymers. Polymer 30 (4), 636–642.

Mulliken, A.D., Boyce, M.C., 2006. Mechanics of the rate-dependent elastic–plastic deformation of glassy polymers from low to high strain rates. Int. J. Solids Struct. 43, 1331–1356.

Neale, K.W., Tŭgcu, P., 1985. Analysis of necking and neck propagation in polymeric materials. J. Mech. Phys. Solids 33, 323–337.

Niordson, F.I., 1965. A unit for testing materials at high strain rates. Exp. Mech. 5, 29–32.

Peirce, D., Shih, C.F., Needleman, A., 1984. A tangent modulus method for rate dependent solids. Comp. Struct. 18, 875–887.

Sewell, M.J., 1965. On the calculation of potential functions defined on curved boundaries. Proc. R. Soc. Lond. A 286, 402–411.

Sørensen, N.J., Freund, L.B., 2000. Unstable neck formation in a ductile ring subjected to impulsive radial loading. Int. J. Solids Struct. 37, 2265–2283.

Tŭgcu, P., 1996. Inertial effects in ductile failure of cylindrical tubes under internal pressure. Int. J. Impact Eng. 18 (5), 539–563.

Tvergaard, V., Needleman, A., 2007. An analysis of thickness effects in the izod test. Report, Dept. Mechanical Engineering, Technical University of Denmark.

Wu, P.D., Van der Giessen, E., 1996. Computational aspects of localized deformations in amorphous glassy polymers. Eur. J. Mech. A/Solids 15, 799–823.

Zhang, H., Ravi-Chandar, K., 2006. On the dynamics of necking and fragmentation—I. Real-time and post-mortem observations in al 6061-o. Int. J. Frac. 142, 183–217.

P2

Bulge formation and necking in a polymer tube under dynamic expansion

Submitted, 2008

Bulge formation and necking in a polymer tube under dynamic expansion

Britta Lindgreen[a], **Viggo Tvergaard**[a], **Alan Needleman**[b]

[a]Department of Mechanical Engineering, Solid Mechanics, Technical University of Denmark, DK-2800 Kgs. Lyngby, Denmark

[b]Division of Engineering, Brown University, 182 Hope Street, Providence, RI 02912, USA

Abstract.

Bulging and necking in long thin polymer tubes subjected to increasing internal pressure is analyzed numerically. The polymer is characterized by a finite strain elastic-viscoplastic constitutive relation and the calculations are carried out using a dynamic finite element program. Two types of imposed loading are prescribed: (i) a pressure that increases linearly with time; and (ii) a change in enclosed volume that increases linearly with time. For both loading conditions, an axisymmetric bulge develops on the tube followed by necking in the bulge. The necks propagate in both the circumferential and axial directions. Multiple necks form at locations given by the thin points associated with the wave number of the prescribed initial thickness imperfection. When a change in enclosed volume is prescribed, the pressure reaches a maximum, decreases and then stays approximately constant. One neck eventually becomes dominant in that it propagates further along the tube axis than any of the other necks.

Keywords: Polymers, viscoplasticity, tube expansion, dynamic loading, neck propagation.

1. Introduction

Plane strain analyses for polymer tubes under rapidly increasing internal pressure have been carried out by Lindgreen *et al.* [1]. A number of investigations of metal rings expanded rapidly by electromagnetic loading (Niordson [2], Han and Tvergaard [3], Tŭgcu [4], Sørensen and Freund [5]) have been carried out. Due to the plane strain assumption, the analyses in Lindgreen *et al.* [1] illustrate the difference between the response of metal tubes and polymer tubes subject to rapid pressure loading. Necking develops as the rings expand and the metal rings have shown neck development in a short wave pattern even when there is only a long wavelength thickness imperfection along the circumference. In the polymer tubes the predicted necking behavior is somewhat different in that necks only form at the thin points defined by the initial thickness imperfection. Furthermore, once the necks have formed in the polymer tube they

propagate along the tube wall in the same way as neck propagation occurs along the length of tensile specimens observed experimentally by G'Sell and Jonas [6] and Marquez-Lucero *et al.* [7]. Due to network hardening in the polymer it was found [1] that the load increases when the necks have spread throughout the entire tube wall so that the stiffness is much increased.

For a long tube the plane strain assumption of Lindgreen *et al.* [1] cannot be used. Long metal tubes under internal pressure loading have been investigated experimentally and numerically by Larsson *et al.* [8], Tvergaard [18] and Mikkelsen and Tvergaard [9] for the purpose of studying the possibility of instabilities when the internal pressure is high enough to give large plastic strains. In these studies an increasing internal tube volume has been prescribed by pumping in a fluid, so that it has been possible to pass the maximum pressure point and study the occurrence of instabilities after that point. Immediately after the maximum pressure point a critical axisymmetric bifurcation mode developed, which was subsequently followed by bifurcations into non-axisymmetric modes. Mikkelsen and Tvergaard [9] have shown that localized necking occurs in the axisymmetric bulge, and this neck region finally gives rise to shear band instabilities which develop into a shear fracture [8].

In the present paper the behavior of a long polymer tube under dynamic internal pressure loading is analyzed numerically. The elastic-viscoplastic material model applied is the polymer model used by Tvergaard and Needleman [10] and also applied for the tube analyses of Lindgreen *et al.* [1]. This material model is based on Wu and Van der Giessen [11] and also on Boyce *et al.* [12], Boyce and Arruda [13], Arruda and Boyce [14], Mulliken and Boyce [15]. As in Lindgreen *et al.* [1] a sinusoidal thickness imperfection is used to initiate the onset of necking along the circumference of the tube and a small axisymmetric radius imperfection is used to trigger the growth of a bulge on the tube. The numerical analysis is a full three dimensional study, taking account of the large strains that develop during bulging and neck propagation in the polymer tube.

2. Problem formulation

A long polymer tube with initial wall thickness $h_0 = 0.002$ m, initial mean radius $R_0 = 0.051$ m and length $2L = 0.8162$ m is considered. In the Cartesian reference coordinate system, y^i, the y^3–axis is along the axis of the tube, while y^1 and y^2 are perpendicular to the tube axis (see Figure 1). With a bulge forming at the middle of the tube, at $y^3 = 0$, symmetry conditions are applied here so that the numerical analysis is only carried out for half of the tube, for $0 \leq y^3 \leq L$. An internal pressure p is applied on the inner surface of the tubes. The corresponding components T^i of the nominal traction vector on the reference base vectors are given by

$$T^i = -p\alpha^{ir} n_r, \qquad \text{on } S_p\text{:} \quad \{(y^1)^2 + (y^2)^2\}^{1/2} = R_0 + \Delta R_0 - h_0/2 + \Delta h_0 \tag{1}$$

Here, S_p is the current inner surface of the tube and the configuration dependent tensor α^{ir} is specified by

$$\alpha^{ir} = \frac{1}{2}\varepsilon^{ijk}\varepsilon^{lmr}(g_{jl} + u_{j,l})(g_{km} + u_{k,m}) \tag{2}$$

with ε^{ijk} as the alternating tensor and n_r as the normal to the inner surface in the reference coordinate system (Sewell [16]). The initial radius and thickness of the perfect tube are R_0 and h_0, respectively, while ΔR_0 and Δh_0 are imperfections to be specified.

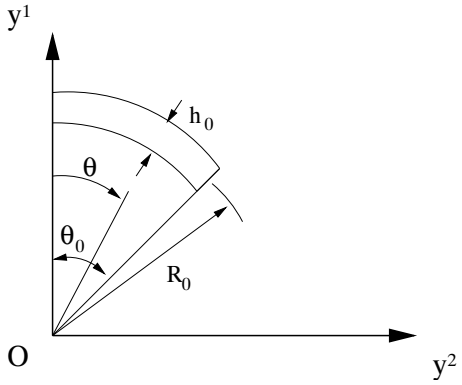

Figure 1. A segment of the tube specified by the initial mean radius R_0, the initial mean thickness h_0 and the angle θ_0 (the y^3–axis points into the paper).

A cosine dimple function Hutchinson *et al.* [17]

$$g(y^3) = \begin{cases} \frac{1}{2}\left(1 + \cos\left(\frac{\pi y^3}{R_{i0}}\right)\right) & 0 \le y^3 \le R_{i0} \\ 0 & R_{i0} < y^3 \le L \end{cases} \tag{3}$$

is used to specify the localized imperfections, which are introduced in order to trigger the onset of instabilities in the form of an axisymmetric bulge on the tube and necks along the tube. The function $g(y^3)$ in Eq. (3) is employed on both the thickness and radial imperfections. An initial sinusoidal thickness imperfection Δh_0 is prescribed Han and Tvergaard [3] on both the inner and the outer surfaces of the tube in order to initiate the onset of necking. Thus, the initial wall thickness is $h_0 + 2\Delta h_0$, with the initial mean thickness h_0 of the tube and with Δh_0 defined by application of the function Eq. (3),

$$\Delta h_0 = -g(y^3)h_0\xi_n\cos\left(\frac{n\pi\theta}{\theta_0}\right) \tag{4}$$

Here θ is defined in Figure 1 and the thickness inhomogeneity is specified through the amplitude ξ_n. Analyses need only be carried out for a 90° segment of the tube circumference since symmetry about the planes $\theta = 0$ and $\theta = \pi/2$ is assumed (symmetry boundary conditions are applied as well) and the

parameter value $\theta_0 = \pi/2$ is chosen. To trigger an axisymmetric bulge an imperfection function ΔR_0 Tvergaard [18] is added to the initial mean radius

$$\Delta R_0 = g(y^3)\xi R_{i0} \tag{5}$$

where $R_{i0} = R_0 - h_0/2$ is the initial inner radius of the tube cross section with no imperfection.

In the results to be shown subsequently the overall deformation level of the tube is specified in terms of the relative volume change $\Delta V/V_0$ where V_0 is the initial enclosed volume and ΔV is the current volume change,

$$\Delta V = \int_{S_p} \alpha^{ir} n_r u_i \, dS \tag{6}$$

where α_{ir} and S_p are defined in Eq. (1). Also, the average logarithmic hoop strain on the inner surface in the middle of the bulge given by

$$\varepsilon_{\text{av}} = \ln\left(\frac{R_i}{R_{i0}}\right) \qquad \text{for} \qquad y^3 = 0 \tag{7}$$

will be used to refer to a deformation stage in the results to follow. Here R_i is the average inner radius based on the current inner cross sectional area A at $y^3 = 0$, and defined by

$$R_i = \sqrt{\frac{A}{\pi}} \tag{8}$$

Two types of applied loading are considered. In one type of prescribed loading, the pressure, p, is prescribed to increase linearly with time as in Lindgreen *et al.* [1]. In the other type of prescribed loading, the volume change, ΔV, is taken to increase linearly with time. This is implemented by continuously adjusting the pressure increment, $\dot{p}\Delta t$, through a regulating algorithm so that the time variation of the pressure keeps the actual volume change ΔV very close to the prescribed linear increase in time. The algorithm adjusts the pressure increment depending on how close the current value of the actual volume change is to the prescribed volume change ΔV and on the value of the rate of volume change relative to the prescribed value $\Delta\dot{V}$.

The finite element calculations are carried out using a convected coordinate Lagrangian formulation with the reference frame taken to be Cartesian. The dynamic principle of virtual work is written as

$$\int_V \tau^{ij}\delta E_{ij} \, dV = -p\int_{S_p} \alpha^{ir} n_r \delta u_i \, dS - \int_V \rho \frac{\partial^2 u^i}{\partial t^2}\delta u_i \, dV \tag{9}$$

with

$$E_{ij} = \frac{1}{2}(u_{i,j} + u_{j,i} + u^k_{,i} u_{k,j}) \tag{10}$$

where V and S are the volume and surface of the body in the reference configuration, and $(\ )_{,i}$ denotes covariant differentiation in the reference frame. The tensor τ^{ij} gives the contravariant components of the Kirchhoff stress on the deformed convected coordinate net ($\tau^{ij} = J\sigma^{ij}$, with σ^{ij} being the contravariant

components of the Cauchy or true stress and J the ratio of current to reference volume), ν_j and u_j are the covariant components of the reference surface normal and displacement vectors, respectively, and ρ is the mass density.

The finite element code is based on a full three dimensional implementation and zero displacement conditions are enforced on the out-of-plane faces at $y^3 = 0$ and $y^3 = L$. Twenty node brick elements are used with eight point integration for the force term, the left hand side of Eq. (9), and twenty-seven point integration for the mass matrix, the last term on the right hand side of Eq. (9). A lumped mass matrix based on Hinton *et al.* [19] is used and time integration is carried out using the Newmark β-method with $\beta = 0$, Belytschko *et al.* [20].

2.1. Constitutive Relations

The constitutive relation used is based on models proposed by Boyce and co-workers Boyce *et al.* [12], Boyce and Arruda [13], Arruda and Boyce [14], Mulliken and Boyce [15] and is adopted from Wu and Van der Giessen [11]. As in Tvergaard and Needleman [10] and Lindgreen *et al.* [1], the elastic part of the response is taken to be governed by a linear hypoelastic relation so that nonlinear elastic effects as well as the distinction between the Cauchy stress $\boldsymbol{\sigma}$ and the Kirchhoff stress $\boldsymbol{\tau}$ are neglected.

The rate of deformation tensor is written as

$$\boldsymbol{D} = \boldsymbol{D}^e + \boldsymbol{D}^p = \boldsymbol{L}^{-1} \cdot \hat{\boldsymbol{\sigma}} + \boldsymbol{D}^p = \boldsymbol{L}^{-1} \cdot \hat{\boldsymbol{\sigma}} + \dot{\gamma}^p \boldsymbol{p} \tag{11}$$

where $\boldsymbol{L}$ is the isotropic tensor of moduli with elastic constants Young's modulus E and Poisson's ratio ν and

$$\dot{\gamma}^p = \dot{\gamma}_0 \exp\left[-\frac{\Delta G}{kT}\left\{1 - \left(\frac{\tau}{s - \alpha(\mathrm{tr}\boldsymbol{\sigma})/3}\right)^m\right\}\right] - \dot{\gamma}_0 \exp\left[-\frac{\Delta G}{kT}\right] \tag{12}$$

Here, m, $\dot{\gamma}_0$, ΔG and α are material constants, T is the temperature (Kelvin) and k is Boltzmann's constant $k = 1.38 \cdot 10^{-23}$ J/K. The last term in Eq. (12) is included so that $\dot{\gamma}^p = 0$ when $\tau = 0$. The exponent m has been considered as having a fixed value in previous implementations of Eq. (12), but is regarded here as a parameter to improve the fitting to experimental results. The value used for the parameter α is sufficiently small so that the term $(s - \alpha(\mathrm{tr}\boldsymbol{\sigma})/3$ in Eq. (12) remains positive over the range encountered. Also,

$$\boldsymbol{p} = \frac{\boldsymbol{\sigma}' - \boldsymbol{b}'}{\sqrt{2}\tau} \qquad \tau = \sqrt{\frac{1}{2}(\boldsymbol{\sigma}' - \boldsymbol{b}') : (\boldsymbol{\sigma}' - \boldsymbol{b}')} \tag{13}$$

with $(\,)'$ denoting deviatoric quantities.

The deformation resistance s in Eq. (12) is taken to have the initial value s_0 and to evolve as

$$\dot{s} = h\left(1 - \frac{s}{s_{ss}}\right)\dot{\gamma}^p \tag{14}$$

where h and s_{ss} are material constants that determine the the extent of softening. More pronounced softening is introduced through a smaller s_{ss}, which is the value of s achieved at steady state.

For the eight chain model of rubber–elasticity, Arruda and Boyce [14],

$$\boldsymbol{b} = \frac{1}{3} C_R \sqrt{N} \frac{\beta_c}{\lambda_c} \boldsymbol{B} \tag{15}$$

where $\boldsymbol{B} = \boldsymbol{F} \cdot \boldsymbol{F}^T$, ($\boldsymbol{F}$ is the deformation gradient), C_R and $\sqrt{N}$ are specified material constants and

$$\lambda_c^2 = \frac{1}{3} \mathrm{tr} \boldsymbol{B} \qquad \beta_c = \mathcal{L}^{-1} \left(\frac{\lambda_c}{\sqrt{N}} \right) \tag{16}$$

with

$$\mathcal{L}(x) = \coth(x) - \frac{1}{x} \tag{17}$$

In eq. (15) the polymer network has been assumed to consist of eight non–Gaussian polymer chains.

Standard kinematical relations are used to obtain an expression for the convected rate of the contravariant components of Kirchhoff stress appearing in the principle of virtual work Eq. (9). The rate tangent method of Peirce *et al.* [21] is used in order to increase the stable time step. Since when λ_c approaches the limit stretch $\lambda_{max} = \sqrt{N}$, the hardening rate given by the increased network stiffness becomes very large, which effectively suppresses all further plastic flow, viscoplastic flow ($\dot{\gamma}_p = 0$) is disabled when λ_c exceeds $0.93\lambda_{max}$ Lai and Van der Giessen [23].

In the numerical analyses the time step Δt is controlled so that the plastic strain increment $\dot{\gamma}_p \Delta t$ never exceeds a specified value $\Delta\gamma$, generally taken as $\Delta\gamma = 0.0002$.

3. Results

The material parameters are chosen to be representative of polycarbonate (PC) with Young's modulus $E = 1814.6$ MPa, $\nu = 0.38$, density $\rho = 1300$ kg/m^3, temperature $T = 298$ K, $\Delta G = 0.374 \cdot 10^{-18}$ J, $\dot{\gamma}_0 = 0.894 \cdot 10^4$ s^{-1}, $m = 0.20$, $C_r = 12.6$ MPa, $N = 2.30$ and the softening parameters $\alpha = 0.08$, $s_0 = 81.65$ MPa, $s_{ss} = 22.71$ MPa, $h = 50.0$ MPa. These material parameters give a reasonable approximation of the compression experiments by Mulliken and Boyce [15]. Under tension PC tends to fail before large plastic strains have been reached Gearing and Anand [22], but failure is not accounted for in the present analyses. The present analyses focus more on the response of polymers in general, with the characteristic polymer increasing–decreasing–increasing stress–strain response.

The numerical calculations are carried out for a long polymer tube with initial wall thickness $h_0 = 0.002$ m, initial mean radius $R_0 = 0.051$ m and total length $L = 0.4081$ m. First, a pressure p increasing linearly with respect to time t is applied on the inner surface of the tube with the prescribed pressure rate $\dot{p} = 411.7$ MPa/s. The finite element mesh used consists of 1 element through the thickness,

60 elements along the circumference and 153 elements along the length. In Lindgreen *et al.* [1] calculations were carried out with 1, 2 and 4 elements through the thickness. It was found that the pressure versus volume change response and the strain rate versus volume change response were well-represented with one 20 node element through the thickness.

In Figure 2 the contours of plastic strain are shown at three levels of deformation. The clearly visible bulge that appears in Figure 2 is initiated through the imperfections in Eqs. (4) and (5) with $n = 9$, $\xi_9 = 0.01$ and $\xi = 0.01$. First, a bulge starts to develop and then necks form at the peak of the

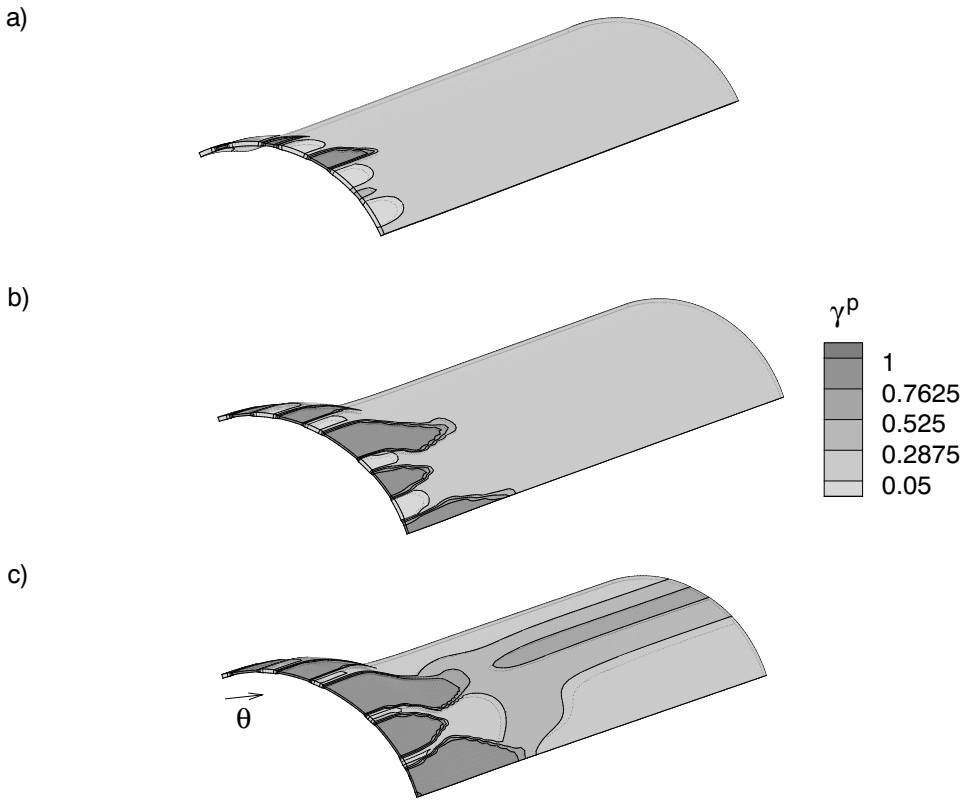

Figure 2. Contours of effective plastic strain γ^p in the deformed configuration for a thin walled tube with $h_0 = 0.002$ m and $h_0/R_0 = 0.0392$ and with an imperfection specified by $n = 9$, $\xi_9 = 0.01$ and $\xi = 0.01$. Only the segment analyzed numerically is shown and θ increases from 0° to 90° in the direction shown. The pressure increases linearly with time and the applied pressure rate is $\dot{p} = 411.7$ MPa/s. The normalized interior volume of the tube, V/V_0, and the average logarithmic hoop strain, $\varepsilon_{\rm av}$, are: (a) $V/V_0 = 1.302$ and $\varepsilon_{\rm av} = 0.217$ (b) $V/V_0 = 1.596$ and $\varepsilon_{\rm av} = 0.404$ (c) $V/V_0 = 1.996$ and $\varepsilon_{\rm av} = 0.540$.

bulge, where the circumferential strains are largest. As was also observed in the plane strain analyses of Lindgreen *et al.* [1] necking only occurs at the thin points defined by the initial thickness imperfection.

After some thinning down at the initial thin points, circumferential neck propagation takes place with the thickness of the necks remaining essentially constant as was also found by Lindgreen *et al.* [1] for polymer tubes under plane strain conditions. This phenomenon of neck propagation is seen experimentally for polymer tensile specimens, e.g. in G'Sell and Jonas [6] and Marquez-Lucero *et al.* [7]. For the three dimensional tube in Figure 2, the necks also propagate along the length of the tube in a way similar to that found by Mikkelsen and Tvergaard [9] for metal tubes. With the pressure prescribed to increase on the entire inner surface, plastic yielding will inevitably occur in the region outside the imperfection, Eqs. (4) and (5), for $y^3 > R_{i0}$, so that necking and neck propagation will also rapidly develop in this region, with a little delay relative to neck formation in the bulge. Figure 2c shows a neck forming outside the bulge region that is beginning to link up with a neck in the bulge. In Figure 2a the neck at $\theta = 90^\circ$ has hardly developed at all, but in Figure 2b it is well developed and in Figure 2c it appears that this is neck and the neighboring necks in the bulge are going to interact with the neck that has formed outside the bulge region.

For the case shown in Figure 2, Figure 3a shows a plot of the growth of the enclosed volume $V = V_0 + \Delta V$ normalized by the initial enclosed volume V_0 versus time t as the tube expands. It is seen that in the elastic range the volume increases linearly with time, but as plastic deformation takes over the tube expands rapidly causing the volume to increase at a very high rate. In Figure 3b the internal pressure p is seen to increase linearly with time t as prescribed. The evolution of the normalized tube thickness h/h_0 at 0° and at 90° (see Figure 2) versus V/V_0 are shown in Figure 3c. As also discussed in

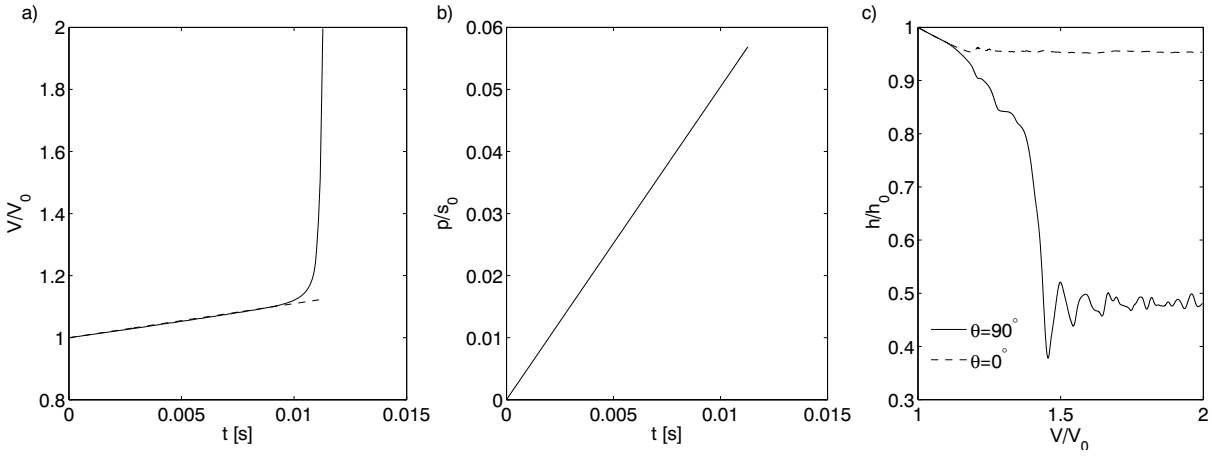

Figure 3. Results for a thin walled tube with $h_0 = 0.002$ m, $h_0/R_0 = 0.0392$, $n = 9$, $\xi_9 = 0.01$ and $\xi = 0.01$ subject to the internal pressure increasing linearly with time. (a) Normalized interior volume of the tube, V/V_0, versus time, t. (b) Normalized applied pressure, p/s_0, versus time, t. (c) Thickness changes at 0° and at 90°, for $y^3 = 0$, versus V/V_0.

Lindgreen *et al.* [1] the oscillations on the curve at the 90° position where a neck is present are associated with more dominant necks that develop elsewhere along the tube circumference and are especially a consequence of a neck developing next to the neck at 90°. At 0° where no neck develops some initial thickness reduction takes place from the Poisson effect.

While a continuously increasing pressure (Figure 3b) will give necking all over the tube, a prescribed volume increase obtained by pumping an incompressible fluid into the tube is expected to emphasize the growth of the bulge. As a consequence, the pressure inside the tube would decay so that neck development is less likely in the region outside the imperfection. Figures 4 and 5 show results for a tube with the enclosed volume prescribed to increase linearly with time. The material properties and the initial imperfection are the same as for the previous case in Figures 2 and 3 where the pressure was prescribed to increase linearly with time. Initially when the deformation is purely elastic the enclosed volume increases linearly with time in both Figures 3a and 5a. In order to provide a similar loading rate in both cases, the pressure rate $\dot{p} = 411.7$ MPa/s is applied at the beginning of the elastic deformation corresponding to $\dot{V}/V_0 = 11.0\text{s}^{-1}$. Subsequently, the pressure is regulated so that the volume rate remains almost constant at about $\dot{V}/V_0 = 11.0\ \text{s}^{-1}$.

The plastic strain contours in Figure 4 show bulge formation followed by neck propagation in the circumferential and axial directions The deviation of the increasing actual enclosed volume from the desired linearly increasing enclosed volume with rate $\dot{V}/V_0 = 11.0\ \text{s}^{-1}$ is seen from Figure 5a to be almost negligible. As a consequence of a linearly increasing enclosed volume the pressure curve in Figure 5b has a maximum soon after plastic deformation has started in the bulge region. This decrease in pressure is the reason that no additional neck occurs outside the bulge in Figure 4c (also for an even larger hoop strains than obtained in Figure 4c) when compared to Figure 2c.

In the early stage of necking, the necks on the bulge do not propagate equally at all initial thin points, for the prescribed linearly increasing pressure as well as for the prescribed linearly increasing volume (see Figure 2a, Figure 4a and Figure 4b). In Figure 2c the lengths of the necks in circumferential direction are rather similar, but this has not happened in Figure 4c where the neck at $\theta = 90°$ has coalesced with its neighbor, while another neck is still very small. One of the reasons may be that necking is highly strain rate dependent as discussed by Lindgreen *et al.* [1] for plane strain, where it was shown that the difference between the neck sizes at the thin points along the tube circumference increases with decreasing strain rate. Therefore, for a prescribed linearly increasing enclosed volume, where the strain rate is rather low, each of the individual necks propagates differently, whereas for a prescribed linearly increasing pressure the necks tend have an essentially equal size due to the suddenly increasing strain rate. In the present full three dimensional analysis the tube shows more individually dominant necks along the circumference

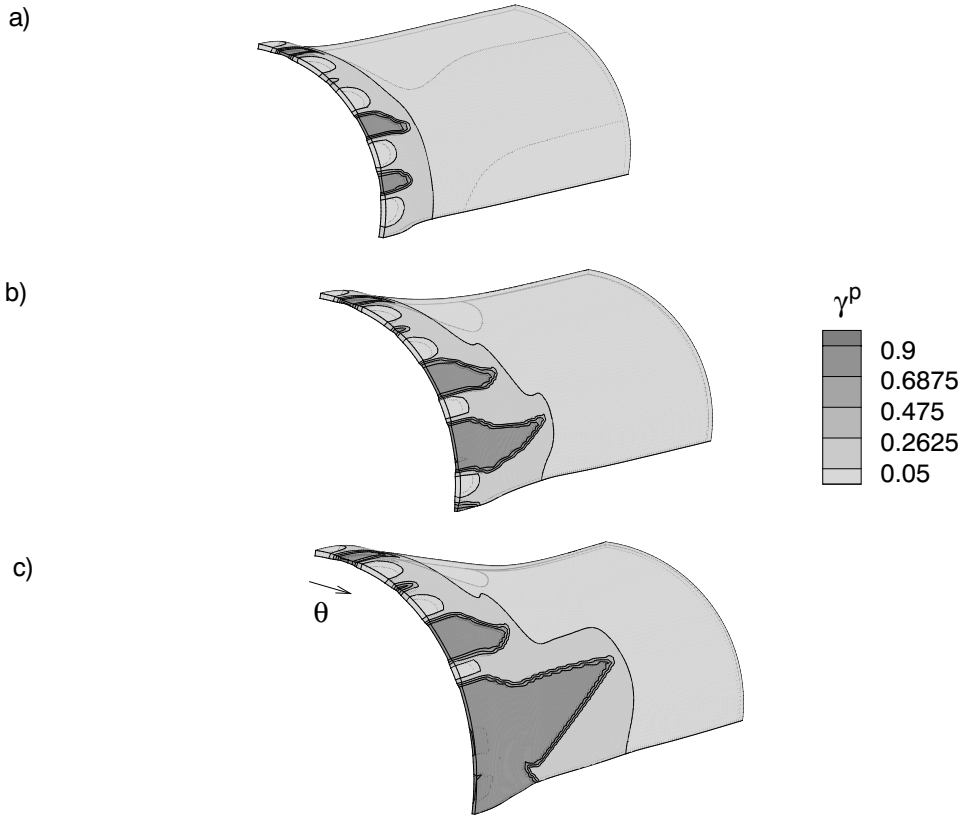

Figure 4. Contours of effective plastic strain γ^p in the deformed configuration for a thin walled tube with $h_0 = 0.002$ m and $h_0/R_0 = 0.0392$ and with an imperfection specified by $n = 9$, $\xi_9 = 0.01$ and $\xi = 0.01$. Only the segment analyzed numerically is shown and θ increases from 0° to 90° in the direction shown. The applied pressure rate is controlled to give $\dot{V}/V_0 = 11.0\ \mathrm{s}^{-1}$. The normalized interior volume of the tube, V/V_0, and the average logarithmic hoop strain, $\varepsilon_{\mathrm{av}}$, are: (a) $V/V_0 = 1.209$ and $\varepsilon_{\mathrm{av}} = 0.209$ (b) $V/V_0 = 1.291$ and $\varepsilon_{\mathrm{av}} = 0.286$ (c) $V/V_0 = 1.466$ and $\varepsilon_{\mathrm{av}} = 0.400$.

(Figure 4) than is found in the plane strain analyses of Lindgreen *et al.* [1]. In general the largest neck in the analysis here shows a tendency to grow more in the axial direction than along the circumference and the neck tends to end in a sharp angle. In Figure 4c the largest neck results from two neighboring necks growing together by neck propagation.

In Figure 5c more dominant necks developing along the tube circumference lead to oscillations in the thickness response at the position of 90° where a neck is present. As is seen in Figure 4a and 4b the neck at 90° develops much more slowly initially than the other necks, but at the end of the calculation this neck has coalesced with the neighboring neck to become very large.

The situation considered in Figures 6 and 7 is identical to that in Figures 4 and 5 with the only

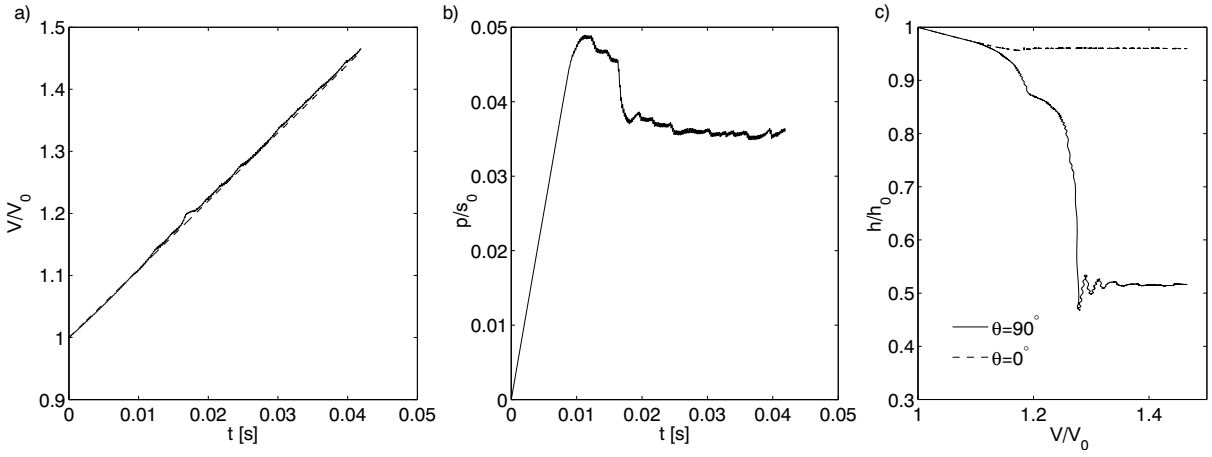

Figure 5. Results for a thin walled tube with $h_0 = 0.002$ m, $h_0/R_0 = 0.0392$, $n = 9$, $\xi_9 = 0.01$ and $\xi = 0.01$ subject to the internal volume increasing linearly with time. (a) Normalized interior volume of the tube, V/V_0, versus time, t. (b) Normalized applied pressure, p/s_0, versus time, t. (c) Thickness changes at 0° and at 90°, for $y^3 = 0$, versus V/V_0.

difference being that the imperfection is now defined by $n = 5$, $\xi_5 = 0.01$ and $\xi = 0.01$. As in Figure 4 some necks in Figure 6 become clearly more dominant than others both in the circumferential and axial directions. In Figure 6a initially at a small hoop strain $\varepsilon_{\text{av}} = 0.191$ the two necks away from the thin point at 90° are more well developed, but at larger strains the neck at 90° develops to gradually become the most dominant neck. The case shown in Figure 4 exhibits a similar tendency of the relative growth rate of necks switching. The neck that has grown furthest in the axial direction in Figure 4a is not the dominant neck in Figures 4b and 4c. As for the earlier cases considered the necks in Figure 6 tend to grow longer in the direction of the tube axis and end in a sharp edge.

Figure 7a shows that the actual enclosed volume V is sufficiently close to increasing linearly with time t and therefore, as in the previous case considered, the pressure reaches a maximum followed by a decrease towards a lower constant level, see Figure 7b. An obvious neck localization and neck propagation at 90° along the tube circumference is seen in Figure 7c whereas no neck develops at 0°.

Next, a case with a higher number of necks is to be investigated. In Figure 8 the plastic strain contours are shown for the linearly increasing internal volume with imperfections defined by $n = 13$, $\xi_{13} = 0.01$ and $\xi = 0.01$. As the necks initiate and propagate in the circumferential and axial directions it is again observed that some necks deform and propagate much more than others even though the initial thickness imperfections are identical. The necks gradually grow longer in the direction of the tube axis. Also, as was observed earlier the three necks closest to the position of 90° coalesce to one large neck

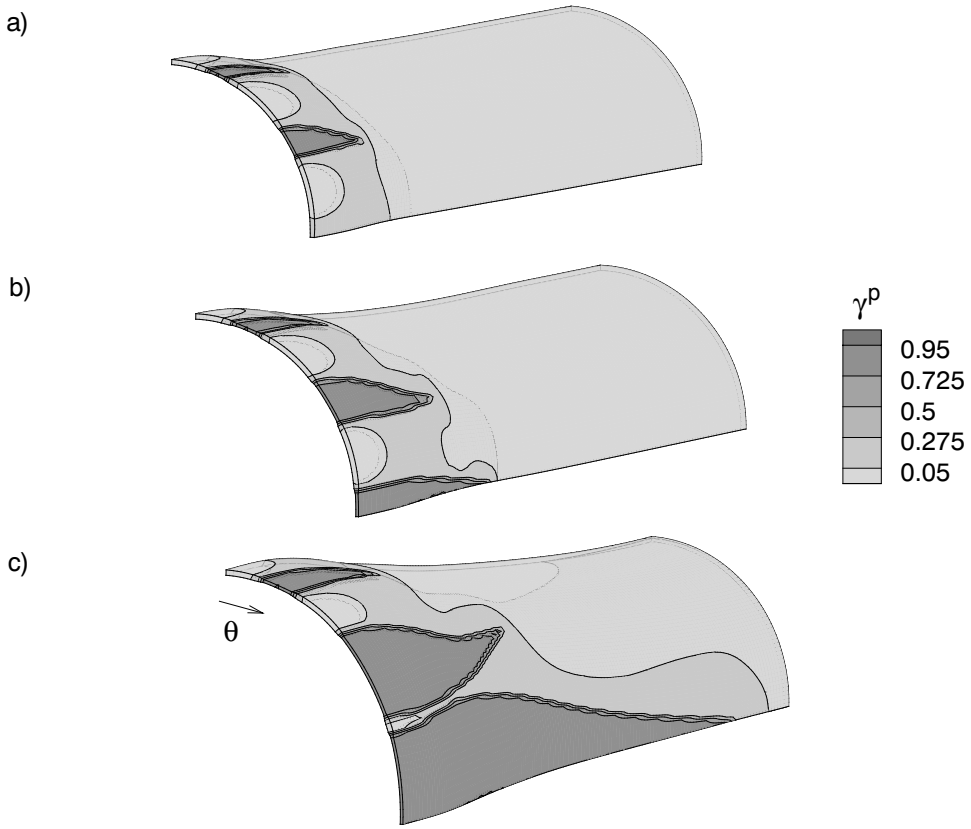

Figure 6. Contours of effective plastic strain γ^p in the deformed configuration for a thin walled tube with $h_0 = 0.002$ m and $h_0/R_0 = 0.0392$ and with an imperfection specified by $n = 5$, $\xi_5 = 0.01$ and $\xi = 0.01$. Only the segment analyzed numerically is shown and θ increases from 0° to 90° in the direction shown. The applied pressure rate is controlled to follow the volume rate $\dot{V}/V_0 = 11.0$ s^{-1}. The normalized interior volume of the tube, V/V_0, and the average logarithmic hoop strain, $\varepsilon_{\rm av}$, are: (a) $V/V_0 = 1.198$ and $\varepsilon_{\rm av} = 0.191$ (b) $V/V_0 = 1.255$ and $\varepsilon_{\rm av} = 0.260$ (c) $V/V_0 = 1.582$ and $\varepsilon_{\rm av} = 0.434$.

ending in a sharp edge.

Figure 9a shows that the enclosed volume variation is close to a linear increase with time, resulting in a pressure maximum (Figure 9b) soon after plastic deformation has initiated in the bulge area. As discussed for the previous cases the thickness response in Figure 9c at the position of 90° oscillates as more dominant necks develop close to the one at 90°, but when the three necks coalesce into one neck near 90°, the thickness is essentially constant since the large neck is now well into the neck propagation mode.

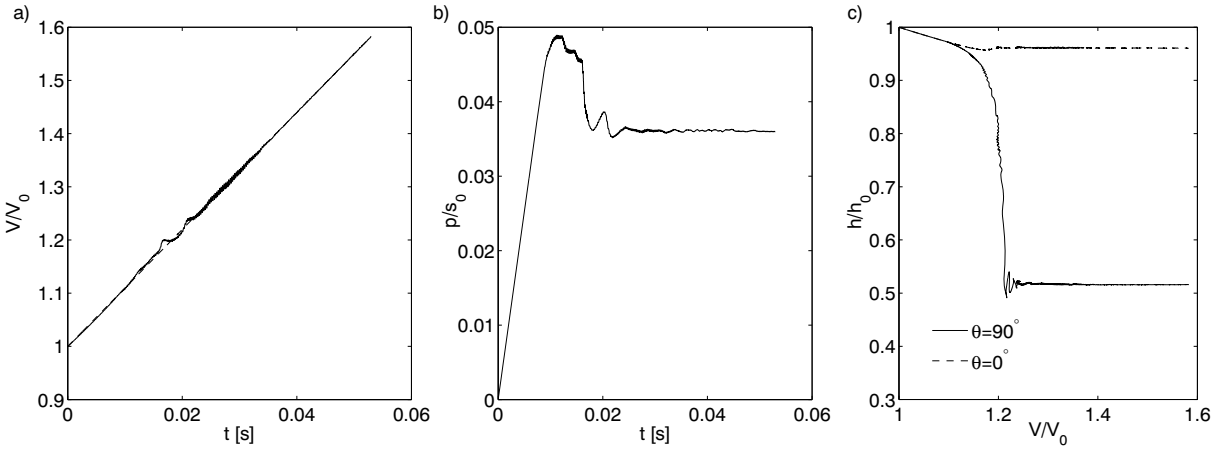

Figure 7. Results for a thin walled tube with $h_0 = 0.002$ m, $h_0/R_0 = 0.0392$, $n = 5$, $\xi_5 = 0.01$ and $\xi = 0.01$ subject to the internal volume increasing linearly with time. (a) Normalized interior volume of the tube, V/V_0, versus time, t. (b) Normalized applied pressure, p/s_0, versus time, t. (c) Thickness changes at 0° and at 90°, for $y^3 = 0$, versus V/V_0.

4. Discussion

A previous investigation [1] of dynamic neck development in pressurized polymer tubes was highly idealized in that the tubes were constrained to satisfy plane strain conditions. Thus any possibility of the deformation pattern varying along the length of the tubes is eliminated *a priori*. Hence, the situation analyzed in Lindgreen *et al.* [1] has a close relation to that in previously published experiments and calculations on the rapid expansion of metal rings [2, 3, 24]. The plane strain results for the polymer tubes have shown the significant difference from metal rings in that the spacing between the necks is strongly tied to the initial thickness imperfections in the tube, whereas the metal rings tend to approach a characteristic neck spacing, independent of the initial imperfection. It is believed that this difference results from the characteristic increasing–decreasing–increasing shape of the uniaxial stress strain curve for polymers.

The expected behavior of long tubes under internal pressure known from metal tubes [8, 9, 18] is that an axisymmetric bulge will develop on the tube and that necking will first develop in the bulge region where the hoop strains grow largest. This type of behavior is also found in the present analyses for polymer tubes. When comparing the effect of either three, five or seven initial thin points along the quarter circumference of the tube it is seen (Figure 7c) that the smallest number gives the earliest neck propagation from the symmetry plane at $\theta = 90°$. Apparently, this results from a rather complex mechanism for the larger numbers of thin points (Figures 5c and 9c) where the large necks near $\theta = 90°$

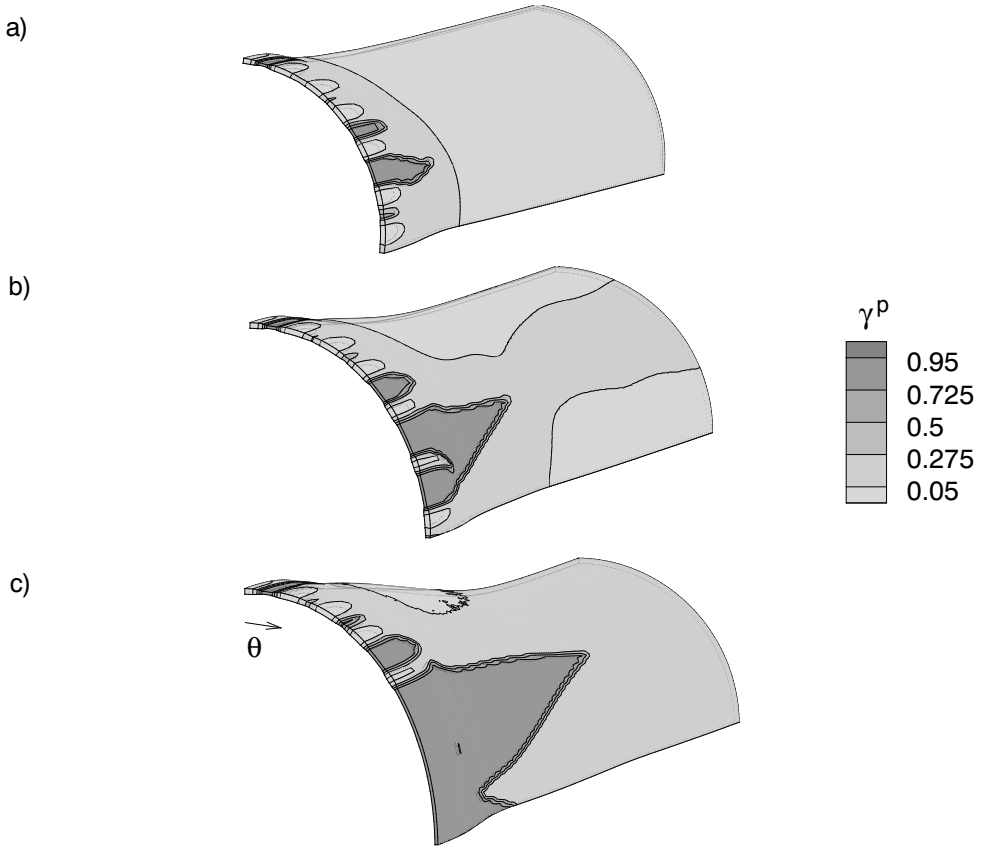

Figure 8. Contours of effective plastic strain γ^p in the deformed configuration for a thin walled tube with $h_0 = 0.002$ m and $h_0/R_0 = 0.0392$ and with an imperfection specified by $n = 13$, $\xi_{13} = 0.01$ and $\xi = 0.01$. Only the segment analyzed numerically is shown and θ increases from 0° to 90° in the direction shown. The applied pressure rate is controlled to follow the volume rate $\dot{V}/V_0 = 11.0\ \mathrm{s}^{-1}$. The normalized interior volume of the tube, V/V_0, and the average logarithmic hoop strain, $\varepsilon_{\mathrm{av}}$, are: (a) $V/V_0 = 1.218$ and $\varepsilon_{\mathrm{av}} = 0.214$ (b) $V/V_0 = 1.306$ and $\varepsilon_{\mathrm{av}} = 0.296$ (c) $V/V_0 = 1.510$ and $\varepsilon_{\mathrm{av}} = 0.420$.

form by coalescence of a number of neighboring necks. In all three cases one neck becomes finally more dominant than the others, with significant neck propagation both in the circumferential direction and in the axial direction. This is very different from the predictions of the plane strain tube analyses [1] where necks of nearly identical length and thickness propagate around each of the initial thin points.

In Figure 2c, with a prescribed linearly increasing pressure, the circumferential lengths of the necks in the middle of the bulge are indeed nearly the same, as in the plane strain results of Lindgreen *et al.* [1] where the pressure was also prescribed to increase linearly with time. Here, a rapid increase of the enclosed volume occurs suddenly (Figure 3a) as soon as plasticity has initiated in the bulge, which means that very large strain rates develop so that viscoplastic effects play a large role. Also, at such explosive

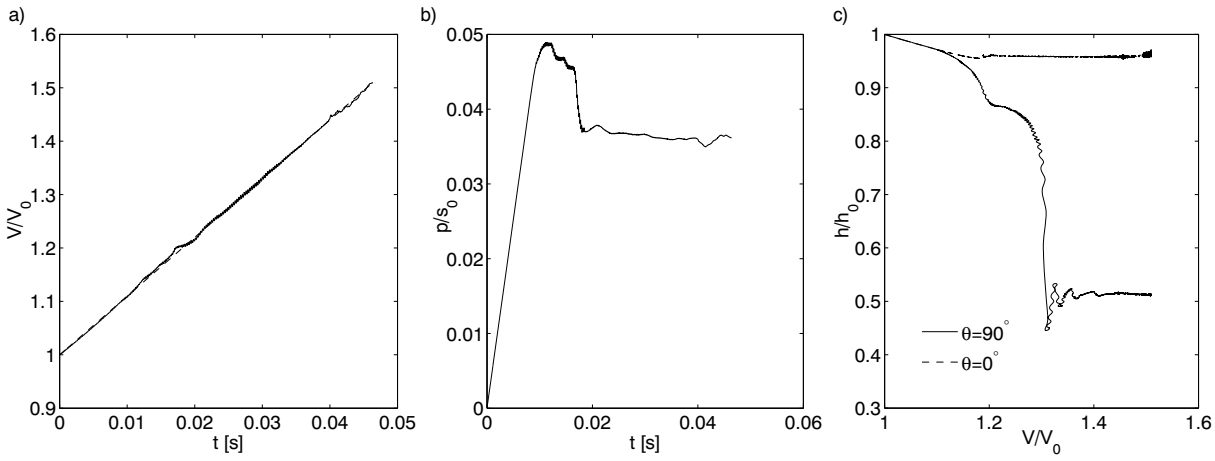

Figure 9. Results for a thin walled tube with $h_0 = 0.002$ m, $h_0/R_0 = 0.0392$, $n = 13$, $\xi_{13} = 0.01$ and $\xi = 0.01$ subject to the internal volume increasing linearly with time. (a) Normalized interior volume of the tube, V/V_0, versus time, t. (b) Normalized applied pressure, p/s_0, versus time, t. (c) Thickness changes at 0° and at 90°, for $y^3 = 0$, versus V/V_0.

deformation rates the solution will try to minimize inertia in the circumferential direction, as is well known from studies of rapidly expanding metal rings. Nevertheless, Figure 2c shows that under this very rapid deformation some of the necks become more dominant in the axial direction.

An enclosed volume that increases linearly with time has been prescribed in most of the present analyses since this gives a behavior more like that observed in experiments where a tube is expanded rather slowly by pumping a nearly incompressible fluid into it at a constant volume rate. When plasticity starts this gives a comparatively slow evolution of the bulge and of the necks that develop in the bulge region. Under linearly increasing pressure, plasticity initiates outside the bulge region shortly after the bulge has started to grow. Then, necks form at many places on the tube and undergo rapid neck propagation. A situation is eventually reached where the entire tube is fully expanded to a near cylindrical shape only limited by the high network stiffness that develops in the polymer. At some stage this mode of deformation would be interrupted by fracture, if a fracture criterion were incorporated in the analyses.

When the enclosed volume is prescribed to increase linearly with time, the internal pressure reaches a maximum soon after the onset of plastic yielding (Figures 5b, 7b and 9b) and subsequently the pressure stays at a lower near constant level while neck propagation occurs. This is the stage at which one dominant neck develops on the tubes by neck propagation in the circumferential direction on the bulge and coalesces with other necks, but also significant neck propagation occurs in the axial direction where these dominant necks show a characteristic sharp edge at the end.

References

[1] Lindgreen, B., Tvergaard, V., and Needleman, A. (2008). Dynamic neck development in a polymer tube under internal pressure loading. *Int. J. Solids Struct.*, **45**, 580–592.

[2] Niordson, F. I. (1965). A unit for testing materials at high strain rates. *Exp. Mech.*, **5**, 29–32.

[3] Han, J.-B. and Tvergaard, V. (1995). Effect of inertia on the necking behaviour of ring specimens under rapid radial expansion. *Eur. J. Mech. A/Solids*, **14**, 287–307.

[4] Tŭgcu, P. (1996). Inertial effects in ductile failure of cylindrical tubes under internal pressure. *Int. J. Impact Engng*, **18**, 539–563.

[5] Sørensen, N. J. and Freund, L. B. (2000). Unstable neck formation in a ductile ring subjected to impulsive radial loading. *Int. J. Solids Structures*, **37**, 2265–2283.

[6] G'Sell, C. and Jonas, J. J. (1979). Determination of the plastic behaviour of solid polymers at constant true strain rate. *J. Mater. Sci.*, **14**, 583–591.

[7] Marquez-Lucero, A., G'Sell, C., and Neale, K. W. (1989). Experimental investigation of neck propagation in polymers. *Polymer*, **30**, 636–642.

[8] Larsson, M., Needleman, A., Tvergaard, V., and Storãkers, B. (1982). Instability and failure of internal pressurized ductile metal cylinders. *J. Mech. Phys. Solids*, **30**, 121–154.

[9] Mikkelsen, L. P. and Tvergaard, V. (1999). A nonlocal two-dimensional analysis of instabilities in tubes under internal pressure. *J. Mech. Phys. Solids*, **47**, 953–969.

[10] Tvergaard, V. and Needleman, A. (2007). An analysis of thickness effects in the izod test. *Int. J. Solids Struct.*, to be published.

[11] Wu, P. D. and Van der Giessen, E. (1996). Computational aspects of localized deformations in amorphous glassy polymers. *Eur. J. Mech. A/Solids*, **15**, 799–823.

[12] Boyce, M. C., Parks, D. M., and Argon, A. S. (1988). Large inelastic deformation of glassy polymers. part i: rate dependent constitutive model. *Mech. Mater.*, **19**, 193–212.

[13] Boyce, M. C. and Arruda, E. M. (1990). An experimental and analytical investigation of the large strain compressive and tensile response of glassy polymers. *Polym. Engng. Sci.*, **30**, 1288–1298.

[14] Arruda, E. M. and Boyce, M. C. (1993). Evolution of plastic anisotropy in amorphous polymers during finite straining. *Int. J. Plast.*, **9**, 697–720.

[15] Mulliken, A. D. and Boyce, M. C. (2006). Mechanics of the rate-dependent elastic-plastic deformation of glassy polymers from low to high strain rates. *Int. J. Solids Struct.*, **43**, 1331–1356.

[16] Sewell, M. J. (1965). On the calculation of potential functions defined on curved boundaries. *Proc. Roy. Soc. Lond. A*, **286**, 402–411.

[17] Hutchinson, J. W., Tennyson, R. C., and Muggeridge, D. B. (1971). Effect of a local axisymmetric imperfection on the buckling behavior of a circular cylindrical shell under axial compression. *AIAA Journal*, **9**, 48–52.

[18] Tvergaard, V. (1990). Bifurcation in elastic-plastic tubes under internal pressure. *Eur. J. Mech. A/Solids*, **9**, 21–35.

[19] Hinton, E., Rock, T., and Zienkiewicz, O. (1976). A note on mass lumping and related processes in the finite element method. *Earthq. Eng. Struct. Dynam.*, **4**, 245–249.

[20] Belytschko, T., Chiapetta, R. L., and Bartel, H. D. (1976). Efficient large scale non-linear transient analysis by finite elements. *Int. J. Numer. Meths. Engrg.*, **10**, 579–596.

[21] Peirce, D., Shih, C. F., and Needleman, A. (1984). A tangent modulus method for rate dependent solids. *Comp. Struct.*, **18**, 875–887.

[22] Gearing, B. P. and Anand, L. (2004). Notch–sensitive fracture of polycarbonate. *Int. J. Solids Struct.*, **41**, 827–845.

[23] Lai, J. and Van der Giessen, E. (1997). A numerical study of crack-tip plasticity in glassy polymers. *Mech. Mater.*, **25**, 183–197.

[24] Zhang, H. and Ravi-Chandar, K. (2006). On the dynamics of necking and fragmentation- i.real-time and post-mortem observations in al 6061-o. *Int. J. Frac.*, **142**, 183–217.

P3

Analysis of a high intensity shear zone between overlapping fiber ends in a polymer matrix composite

To be published in
European Journal of Mechanics - A/Solids

Analysis of a high intensity shear zone between overlapping fiber ends in a polymer matrix composite

Britta Lindgreen

Department of Mechanical Engineering, Solid Mechanics, Technical University of Denmark, DK-2800 Kgs. Lyngby, Denmark

12th February 2008

Abstract

The formation of high intensity shear zones in a glass fiber reinforced thermoplast is studied numerically. The thermoplast is characterized by a finite strain elastic–viscoplastic constitutive relation and the calculations are carried out using a dynamic finite element program where plane strain conditions are assumed to prevail in the direction of the thickness. Different ratios of the elongation strain and the transverse strain are studied to consider the effect of different levels of stress triaxiality and the effect of these states on the shear zone development and emerging strain and stress concentrations. Comparing a case of embedded infinitely stiff fibers to a case with glass fiber reinforcement shows little difference thus illustrating that the glass fibers act approximately as infinitely stiff. Fiber spacing and fiber width are shown to influence the shear zones and the stress fields that develop as the highly deformed region approaches the limit resulting from network stiffening in the polymer. A simple analysis assuming periodicity is included in order to study the mechanical behaviour of the polymer matrix between fiber ends with long overlap.

1 Introduction

Several investigations on fiber reinforced polymers have focused on describing fiber–matrix debonding due to interfacial shear stresses occuring between the fiber and the matrix, fiber pull out etc. as dealt with analytically by Karbhari and Wilkins (1990) and experimentally by Hampe and Marotzke (1992) and Andrews et al. (1994). It is highly interesting to improve the fiber–matrix adhesion mechanism as reviewed by Kalantar and Drzal (1990) and studied in Hampe and Marotzke (1992). Also, delamination and interface damage has been analyzed numerically by Marsal et al. (2006). Using a shear lag model formulation, Laws and Dvorak (1988) have shown simulation examples of interface damage and transverse matrix cracking with a focus on glass–fiber/epoxy composites, as also discussed by Berthelot (2003).

In the present paper the development of high intensity shear zones in a glass–fiber reinforced thermoplast is investigated. The occurrence of diagonal high intensity shear zones between the fibers in a manner similar to that of fiber reinforced metal matrix composites, see Llorca et al. (1991), are of interest since they might result in debonding or matrix failure much like that of fracture occuring in a shear band in the direction of 45° to the loading axis as described by Fleck (1997). Furthermore, polymer matrix composites have a low shear strength (Fleck (1997)) which limits the tensile strength of the composite (Hampe and Marotzke (1992)) and therefore the shear behaviour at the fiber–matrix interface must be known.

Here, a realististic numerical polymer model is applied to study a local problem of a fiber reinforced polymer. Prevoius numerical investigations of local behaviour in polymer matrix composites have mostly been carried out by using models that describe the mechanical behaviour of metals e.g. J_2-flow theory, without incorporating network stiffening in the material behaviour even though this is an important polymer characteristic. Also, it is

highly interesting to analyse whether the high intensity shear zones that are expected to develop in the matrix between the fiberends localize into a shear band as is known to be the case when the polymer matrix has been modelled using a constitutive law for metals. Besides, for polymers the localization of deformation in terms of shear banding (Seelig and Van der Giessen (2002)) or necking (G'Sell and Jonas (1979), Lindgreen et al. (2008)) is known to stabilize by network hardening of the polymer due to the alignment of the macromolecular network at large strains, which tends to lead to broadening of localized bands.

In the present numerical analyses, the fibers are transversely staggered and high strain and stress concentrations are expected to appear at the sharp fiber edges in a manner similar to that described by Llorca et al. (1991) and Tvergaard (2003) where fiber reinforced metal matrix composites were considered. This would inevitably lead to debonding and fracture along the interface between the matrix and the reinforcement. Also, E-glass fiber reinforced polycarbonate experiments performed by Hampe and Marotzke (1992) show a brittle fracture process between fiber and matrix that indicates high stresses at the fiber–matrix interface during fiber pull out.

Here, numerical analyses of bands of high shear intensity, strain and stress concentrations developing in the polymer matrix between the fibers and at the interface are carried out using an elastic–viscoplastic constitutive relation adopted from Boyce et al. (1988). A few changes of the model are incorporated based on the mathematical formulations suggested by Boyce and co-workers (Boyce et al. (2000), Boyce and Arruda (1990), Arruda and Boyce (1993), Mulliken and Boyce (2006)), and used by Lai and Van der Giessen (1997) and Tvergaard and Needleman (2007). The finite element analysis is based on a two dimensional plane strain implementation of the numerical code. A slightly different version of the constitutive relation than that of Boyce et al. (1988) (adopted from Wu and Van der Giessen (1996) and also based on models suggested by Boyce and co–workers) was used

in Tvergaard and Needleman (2007), Lindgreen et al. (2008) and Lindgreen et al. (2007).

The matrix material parameters to be used in the subsequent calculations are fitted to describe a polycarbonate that is chosen to represent the thermoplast matrix. The E–glass fibers are assumed to be linearly elastic.

2 Problem formulation

The finite element calculations are carried out using a convected coordinate Lagrangian formulation based on the dynamic principle of virtual work

$$\int_V \tau^{ij}\delta E_{ij}\, dV = \int_S T^i \delta u_i\, dS - \int_V \rho \frac{\partial^2 u^i}{\partial t^2}\delta u_i\, dV \tag{1}$$

with

$$T^i = (\tau^{ij} + \tau^{kj} u^i_{,k})\nu_j \tag{2}$$

$$E_{ij} = \frac{1}{2}(u_{i,j} + u_{j,i} + u^k_{,i} u_{k,j}) \tag{3}$$

where V and S are the volume and surface of the body in the reference configuration, and $(\ )_{,i}$ denotes covariant differentiation in the reference frame. The tensor τ^{ij} denotes the contravariant components of Kirchhoff stress on the deformed convected coordinate net ($\tau^{ij} = J\sigma^{ij}$, with σ^{ij} being the contravariant components of the Cauchy or true stress and J the ratio of current to reference volume), ν_j and u_j are the covariant components of the reference surface normal and displacement vectors, respectively, and ρ is the mass density. Since no surface forces are applied in the present paper, there will be no prescribed components T^i of the nominal traction vector. Although a transient analysis is applied the loading rates considered are rather low so that inertia has practically no effect on the results presented. Therefore, the computations could have been carried out using a static solution. However, the implementation of the dynamic principle of virtual work eq. (1) allows for solving the equations directly without an equation solver and the calcuation

time grows linearly and more slowly with the total number of degrees of freedom than is the case if a static solution was applied. This way of solving equilibrium equations is sometimes called dynamic relaxation and it has been used in many studies by Tvergaard and Needleman (1992) and Tvergaard and Needleman (2006).

The material region to be analyzed numerically has initial overall length a and width b, as shown in Figure 1, and it is a part of a fiber reinforced polymer where the transversely staggered fiber ends are assumed to be periodically distributed. Each stiff fiber has the total length $2a_1$ and width $2b_1$ since symmetry boundary conditions are applied along $y^1 = 0$ and $y^2 = 0$. However, the results are expected to be relevant to much larger fibres, such that only a region near fiber overlap is studied. In the Cartesian reference coordinate system, y^i, the y^1-axis follows the length a of the specimen and the y^2-axis follows the width b. For the main case considered the geometry is specified by the values $a_1/a = 2/3$,

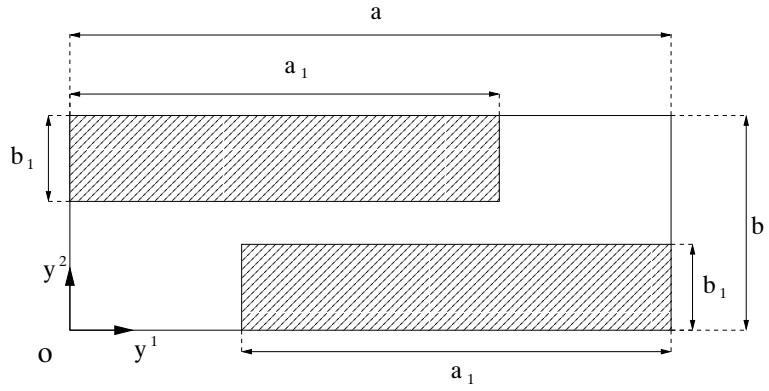

Figure 1. Specimen specified by overall length a, overall width b, half fiber length a_1 and half fiber width b_1.

$b/a = 1/4$ and $b_1/b = 1/3$ of the length and width ratios. Deviations from these values will be studied in order to investigate the sentitivity to fiber spacing and fiber thickness. The computations are actually carried out for unrealistically large fibers, but since intertia has practically no influence at the loading rates considered here, the results also apply to realistic fiber dimensions. Plane strain conditions are assumed in the third direction and therefore the studies are limited to a two dimensional analysis, such that only idealized

planar, rectangular fibers with sharp edges are considered. The fact that the geometry to be studied is point-symmetric with respect to the center could have been exploited in order to reduce the size of the mesh. However, a full two dimensional analysis is carried out. Here, plane strain is assumed, but in reality the three dimensional geometry of the fibers is important for the mean stress results to be discussed later. In order to investigate the three dimensional effects an axisymmetric analysis could be carried out, analogous to the use of point-symmetry as applied by Tvergaard (2003) in a study of short fiber reinforced metal matrixes composites. However, the plane strain assumption is expected to give a reasonable insight in the behaviour at the overlapping fiber ends.

A prescribed velocity $v(t)$ is applied along $y^1 = a$ so that

$$\dot{u}_1(a, y^2) = v(t) \qquad \text{for} \qquad 0 \leq y^2 \leq b \tag{4}$$

where

$$v(t) = \begin{cases} v_1 t/t_r & \text{for} \quad t < t_r \\ \\ v_1 & \text{for} \quad t > t_r \end{cases} \tag{5}$$

The loading is modelled using the velocity $v_1 = (5/6)a$ s^{-1} and the ramping time $t_r = 0.02$ s in all the cases analyzed. During deformation the total volume V_c of the specimen is:

$$V_c = h(a + u_1)(b + u_2) \tag{6}$$

where u_1 is the displacement at $y^1 = a$ in the direction of y^1 and u_2 is the displacement at $y^2 = b$ in the direction of y^2. The thickness h is taken to equal 1 since the analyses are carried out for plane strain only. If the volume V_c is to remain constant, the volume increment $\dot{V}_c$=0 and thereby

$$[\dot{u}_2]_{incomp} = -\dot{u}_1 \frac{b + u_2}{a + u_1} \tag{7}$$

is the incremental displacement rate to be applied along $y^2 = b$ if the region analyzed is to remain incompressible during deformation. The velocity actually prescribed along $y^2 = b$

is taken to be

$$\dot{u}_2 = \alpha[\dot{u}_2]_{incomp} \qquad \text{for} \qquad 0 \leq \alpha \leq 1 \tag{8}$$

where $\alpha = 1$ corresponds to pure incompressibility and $\alpha = 0$ will cause a significant volume change since $\dot{u}_2 = 0$. Cases of intermediate values of α are also solved and discussed in Section 3.

The finite element code is based on a two dimensional plane strain implementation of the constitutive model. Eight node isoparametric elements are used with four integration points for calculating the force term numerically (the left hand side of eq. (1)) whereas a nine point integration is needed for the mass matrix (the last term on the right side of eq. (1)). The mass matrix is lumped leading to both computational efficiency and accuracy (see Krieg and Key (1973)). Also, the integrations for the mass matrix need only be carried out once since a Lagrangian formulation is applied and the meshes are chosen so that the element sizes in the matrix between overlapping fibers are the same in all computations. The numerical time integration of the equations is carried out using the Newmark β–method with $\beta = 0$ (Belytschko et al. (1976)).

2.1 Constitutive Relations

The constitutive relations used in the numerical calculations are mainly adopted from Boyce et al. (1988), but some changes are made based on the mathematical formulations proposed by Boyce and co-workers (Boyce et al. (2000), Boyce and Arruda (1990), Arruda and Boyce (1993), Mulliken and Boyce (2006)). Nonlinear elastic effects are neglected and all stresses referred to in the following eq. (9) – (25) are Cauchy stresses.

Boyce et al. (1988) presents a model that divides the overall deformation resistance into an intermolecular resistance A acting in parallel with a network resistance B. The deformation resistance A is further divided into an elastic $(\ )^e$ and plastic $(\ )^p$ contribution. The total

deformation gradient, $\boldsymbol{F}$, is the same for resistance A and B so that $\boldsymbol{F} = \boldsymbol{F}_A = \boldsymbol{F}_B$ and the total stress $\boldsymbol{\sigma}$ acting on the system has a contribution from each resistance.

For resistance A the rate of deformation tensor is written as

$$\boldsymbol{D} = \boldsymbol{D}^e + \boldsymbol{D}^p \tag{9}$$

assuming $\boldsymbol{D}^e$ to be the elastic contribution and $\boldsymbol{D}^p$ to be the plastic contribution with the rate of deformation tensor, $\boldsymbol{D}$, defined as the symmetric part of the velocity gradient tensor $\boldsymbol{L}$ given by

$$\boldsymbol{L} = \dot{\boldsymbol{F}}\boldsymbol{F}^{-1} \tag{10}$$

where $\boldsymbol{F}$ is the total deformation gradient. The total deformation gradient can be decomposed into elastic and plastic components through multiplicative decomposition

$$\boldsymbol{F} = \boldsymbol{F}^e\boldsymbol{F}^p \tag{11}$$

where $\boldsymbol{F}^e$ is the elastic deformation gradient and $\boldsymbol{F}^p$ is the plastic deformation gradient. They can be further decomposed into stretch and rotation components as follows

$$\boldsymbol{F}^e = \boldsymbol{V}^e\boldsymbol{R}^e \tag{12}$$

Inserting eq. (11) into eq. (10) yields

$$\boldsymbol{L} = \dot{\boldsymbol{F}}^e\boldsymbol{F}^{e-1} + \boldsymbol{F}^e\dot{\boldsymbol{F}}^p\boldsymbol{F}^{p-1}\boldsymbol{F}^{e-1} = \boldsymbol{L}^e + \tilde{\boldsymbol{L}}^p \tag{13}$$

Given that

$$\tilde{\boldsymbol{L}}^p = \boldsymbol{D}^p + \tilde{\boldsymbol{W}}^p \tag{14}$$

the decomposition in an elastic and a plastic part is made unique by taking the spin tensor $\tilde{\boldsymbol{W}}^p = 0$. Thus, rotations are included in the elastic part $\boldsymbol{W}^e$. Using eq. (14) together with the last term of eq. (13) it is found that

$$\dot{\boldsymbol{F}}^p = \boldsymbol{F}^{e-1}\boldsymbol{D}^p\boldsymbol{F} \tag{15}$$

The updated $\dot{\boldsymbol{F}}^p$ is multiplied by the time increment Δt and added to the old $\boldsymbol{F}^p$ in order to calculate the new $\boldsymbol{F}^p$. Hereafter, the elastic contribution, $\boldsymbol{F}^e$, is found from eq. (11) through $\boldsymbol{F}^e = \boldsymbol{F}\boldsymbol{F}^{p-1}$. The plastic part of deformation, $\boldsymbol{D}^p$, is specified as

$$\boldsymbol{D}^p = \dot{\gamma}^p \boldsymbol{p}_A \tag{16}$$

with (Tvergaard and Needleman (2007))

$$\dot{\gamma}^p = \dot{\gamma}_0 \exp\left[-\frac{\Delta G}{kT}\left\{1 - \left(\frac{\tau}{s - \alpha(\mathrm{tr}\boldsymbol{\sigma})/3}\right)^m\right\}\right] - \dot{\gamma}_0 \exp\left[-\frac{\Delta G}{kT}\right] \tag{17}$$

Here, m, $\dot{\gamma}_0$, ΔG and α are material constants, T is the temperature (Kelvin) and k is Boltzmann's constant $k = 1.38 \cdot 10^{-23}$ J/K. The last term in eq. (17) is included so that $\dot{\gamma}^p = 0$ when $\tau = 0$. Also,

$$\boldsymbol{p}_A = \frac{\boldsymbol{\sigma}'_A}{\sqrt{2}\tau_A} \qquad , \qquad \tau_A = \sqrt{\frac{1}{2}\boldsymbol{\sigma}'_A \boldsymbol{\sigma}'_A} \tag{18}$$

with $(\ )'$ denoting deviatoric quantities. The stress $\boldsymbol{\sigma}_A$ is found from

$$\boldsymbol{\sigma}_A = \frac{1}{J_A} L^e \ \ln \boldsymbol{V}^e \tag{19}$$

Here $J_A = \det \boldsymbol{F}^e$ is the volume change, L^e is the fourth order tensor of elastic constants defined by

$$L^e_{ijkl} = \frac{E}{1+\nu}\left[\frac{1}{2}\left(\delta_{ik}\delta_{jl} + \delta_{il}\delta_{jk}\right) + \frac{\nu}{1-2\nu}\delta_{ij}\delta_{kl}\right] \tag{20}$$

and $\ln \boldsymbol{V}^e$ is a strain that is calculated using $(\boldsymbol{V}^e)^2 = \boldsymbol{F}^e \boldsymbol{F}^{eT}$.

The deformation resistance s in eq. (17) is taken to have the initial value s_0 and to evolve from

$$\dot{s} = h\left(1 - \frac{s}{s_{ss}}\right)\dot{\gamma}^p \tag{21}$$

where h and s_{ss} are material constants.

For the network contribution, an eight chain model of rubber–elasticity (Boyce et al.

(1988)) is used

$$\boldsymbol{\sigma}_B = \frac{1}{J_B}\frac{C_R}{3}\frac{\sqrt{N}}{\lambda_c}\beta_c(\boldsymbol{B} - \lambda_c^2\boldsymbol{I}) \tag{22}$$

where $\boldsymbol{B} = J_B^{-2/3}\boldsymbol{F}\boldsymbol{F}^T$, $J_B = \det\boldsymbol{F}$, C_R and $\sqrt{N}$ are specified material constants and

$$\lambda_c^2 = \frac{1}{3}\mathrm{tr}\boldsymbol{B}^n \qquad \beta_c = \mathcal{L}^{-1}\left(\frac{\lambda_c}{\sqrt{N}}\right) \tag{23}$$

with

$$\mathcal{L}(x) = \coth(x) - \frac{1}{x} \tag{24}$$

In eq. (22) it has been assumed that the polymer network consists of eight non–Gaussian polymer chains.

The total Cauchy stress $\boldsymbol{\sigma}$ acting on the system is then given by

$$\boldsymbol{\sigma} = \boldsymbol{\sigma}_A + \boldsymbol{\sigma}_B \tag{25}$$

Standard kinematical relations are used to obtain an expression for the contravariant components of the Kirchhoff stress in the convected coordinate system, appearing in the principle of virtual work eq. (1).

When λ_c approaches the limit stretch $\lambda_{max} = \sqrt{N}$, the hardening rate provided by the increased network stiffness grows very large, thus effectively suppressing all further plastic flow which also leads to a dramatic stress increase due to the Langevin function eq. (24). As in Lai and Van der Giessen (1997) and Tvergaard and Needleman (2007), viscoplastic flow is disabled ($\dot{\gamma}^p = 0$) when λ_c exceeds $r\lambda_{max}$. In the present paper $r = 0.85$ is chosen. The choise of $r = 0.85$ only affects the results slightly since the plastic flow is already heavily suppressed at this stage and therefore it can be neglected. If the cut off $r = 0.85$ was not implemented the calculations would become unstable.

3 Results

The fiber reinforced polymer used is representative of polycarbonate (PC), among other amorphous glassy polymers, with Young's modulus $E = 1814.6$ MPa, $\nu = 0.38$, density $\rho = 1300$ kg/m^3, temperature $T = 298$ K. Further material parameters are $\Delta G = 0.374 \cdot 10^{-18}$ J, $\dot{\gamma}_0 = 0.894 \cdot 10^4$ s^{-1}, $m = 0.20$, $C_r = 12.6$ MPa, $N = 2.30$ and the softening parameters $\alpha = 0.08$, $s_0 = 81.65$ MPa, $s_{ss} = 22.71$ MPa, $h = 50.0$ MPa. These parameters were used by Tvergaard and Needleman (2007), Lindgreen et al. (2008) and Lindgreen et al. (2007) and they were fitted to experimental compression curves for PC given in Mulliken and Boyce (2006). The fiber material is chosen to represent E–glass deforming purely elastically with Young's modulus $E = 72.0$ GPa, $\nu = 0.22$, density $\rho = 2600$ kg/m^3. The material behaviour of the fiber is approximated as isotropic elasticity since the fibers are assumed much stiffer than the matrix material and the major purpose of the subsequent analyses is to model the material behaviour of the polymer matrix between overlapping fiber ends.

A region (Figure 1) is analyzed where the dimensions are specified by $b/a = 1/4$, $a_1/a = 2/3$ and $b_1/b = 1/3$. For the situation $\alpha = 0.75$ Figure 2 shows contourplots for the maximum principal logarithmic strain ε_{max}, the normalized stretch λ_c/λ_{max}, see eq. (23), and mean stress $\sigma_m = \frac{1}{3}\text{tr}\boldsymbol{\sigma}$ (or in tensor components $\frac{1}{3}G_{kl}\sigma^{kl}$). The logarithmic strain at the stage shown is $\varepsilon_1 = 0.0575$ where $\varepsilon_1 = \ln(1 + u_1/a)$. A diagonal band of high shear intensity is seen to develop between the fiber ends in Figure 2a, as was also observed and discussed by Llorca et al. (1991) for a SiC fiber reinforced metal-matrix. It is seen that the largest principal logarithmic strain develops at the sharp fiber edges. Also in MMC's it has been found that fibers give rise to higher strain concentrations at the sharp fiber edges (Llorca et al. (1991); Tvergaard (2003)).

As network stiffening takes over, viscoplastic flow is cut off causing the material to deform

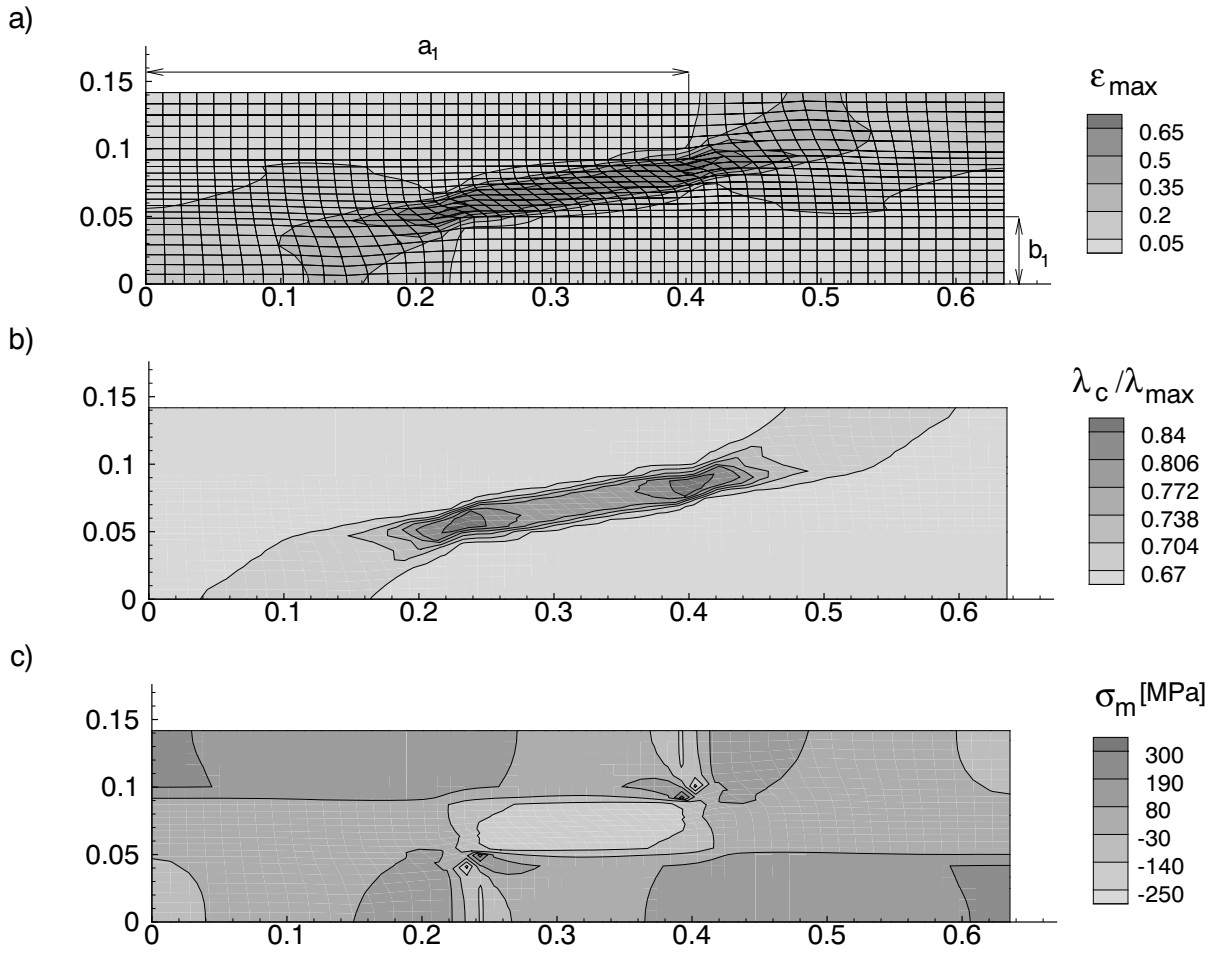

Figure 2. Contours of: (a) Maximum principal logarithmic strain ε_{max} (b) Normalized stretch λ_c/λ_{max} (c) Mean stress σ_m. Here $\alpha = 0.75$, $\varepsilon_1 = 0.0575$ and the region analyzed is specified by the normalized length $a_1/a = 2/3$ and by the widths $b/a = 1/4$, $b_1/b = 1/3$.

elastically when $\lambda_c > 0.85\lambda_{max}$ (according to the limit $r = 0.85$ chosen in the present paper). From Figure 2b this network stiffening is observed to have initiated in the polymer at the fiber edges where the strain concentrations are highest. Elsewhere along the shear zone this limiting value of λ_c has not yet been reached, but the network stiffening is already large causing the material in the shear zone to deform almost elastically since the plastic flow is suppressed by the effect of σ_B according to (22). This is seen from Figure 2a where the mesh lines are nearly parallel in the shear zone between the high strain

concentrations.

In Figure 2c the largest mean stress appears as stress concentrations at the sharp fiber edges in the polymer matrix. This is in agreement with experiments performed by Hampe and Marotzke (1992) for E–glass reinforced PC where brittle fracture indicating high stresses occurs at the fiber matrix interface. Similar results were obtained by Tvergaard (2003) for fiber reinforced metal-matrices. Large mean stresses are also seen to develop in the fibers (Figure 2c) due to the stiffness of the fibers. In the load carrying matrix between the fibers, negative mean stresses emerge since $\alpha = 0.75$ nearly corresponds to a uniaxial plane strain deformation, as will be shown subsequently in Figure 5a.

Figures 3 and 4 show the effect of lower values of α and all other parameters are identical to those in Figure 2. It is noticed that the strains ε_1 of which the contourplots are shown are slightly different from the first value $\varepsilon_1 = 0.0575$ in Figure 2. When $\alpha = 0.50$ as in Figure 3, strain and stress concentrations are still found at the sharp edges of the fibers together with a high intensity shear zone connecting the strain concentration points as observed earlier. A significant change in Figure 3 relative to the situation considered in Figure 2 is the increased level of stress in the matrix area between the fibers, Figure 3c versus Figure 2c, due to the larger deviation from uniaxial plane strain for the present case where $\alpha = 0.50$ rather than the earlier case of $\alpha = 0.75$.

If instead $\alpha = 0$ is considered, Figure 4 shows a less intensive shear zone with a much broader band compared to the ones in the two earlier studies (Figure 2 and 3) where α is larger. Both strain and stress concentrations still appear at the edges of the fiber. As a result of $\alpha = 0$ no negative mean stresses develop in the polymer matrix, particularly not between the fiber ends as was the case in the previous studies. Opposite to metals polymers are very sensitive to hydrostatic pressure in the sense that their plastic behaviour depends on it. This is seen directly from eq. (17) where the effective plastic strain rate is seen to increase if the mean stress is positive, while $\dot{\gamma}^p$ is reduced if the mean stress is

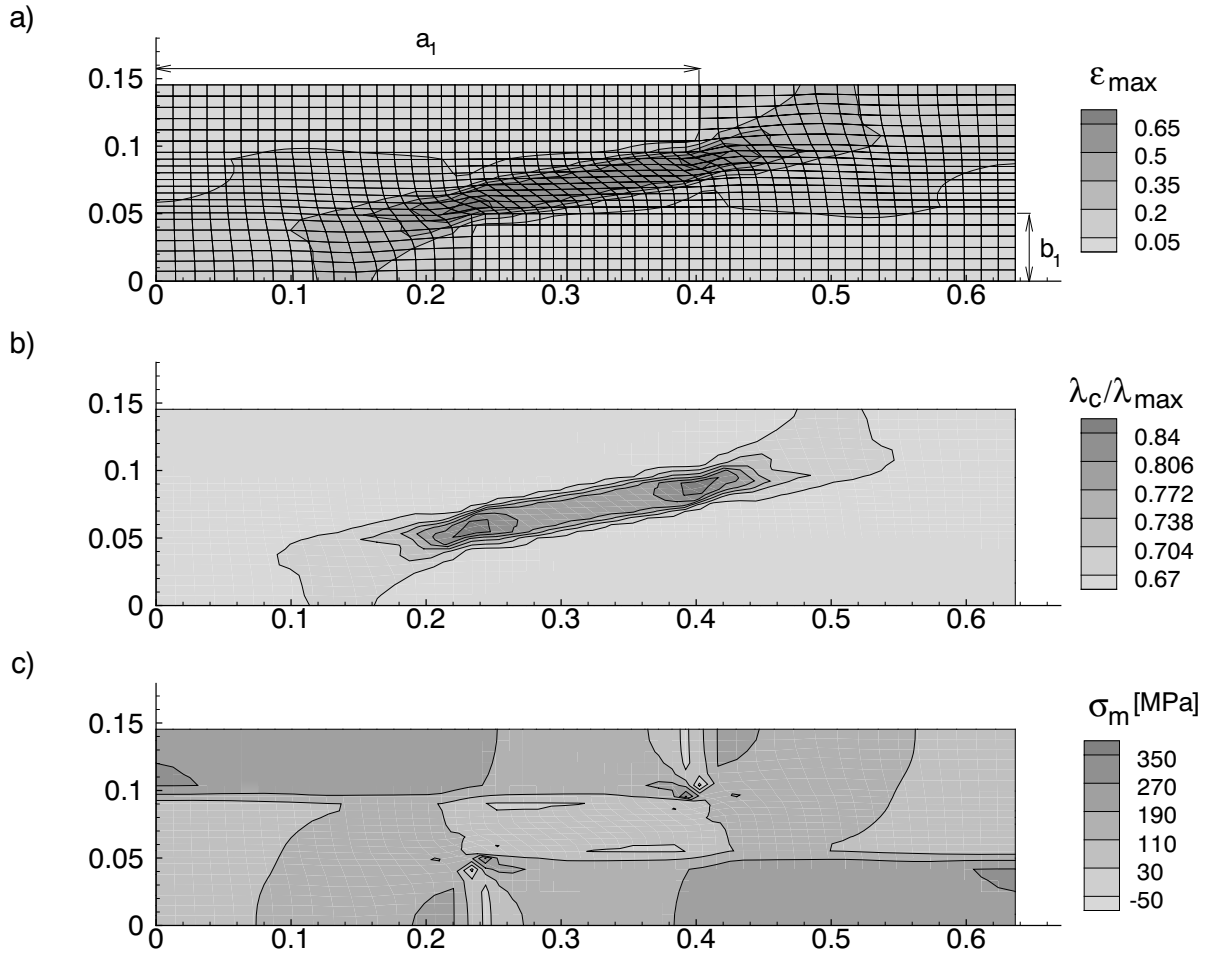

Figure 3. Contours of: (a) Maximum principal logarithmic strain ε_{max} (b) Normalized stretch λ_c/λ_{max} (c) Mean stress σ_m. Here $\alpha = 0.50$, $\varepsilon_1 = 0.0588$ and the region analyzed is specified by the normalized length $a_1/a = 2/3$ and by the widths $b/a = 1/4$, $b_1/b = 1/3$.

negative.

In general the average stress σ_1 along the y^1–axis is higher than the average stress σ_2 along the y^2–axis for all cases studied, as can be seen from the stress curves in Figure 5. When the value of α in eq. (8) is reduced σ_1 increases, especially at higher values of the logarithmic strain ε_1. The negative average stress σ_2 in Figure 5a is directly connected to the prescribed overall deformation that also results in negative stresses σ_m between the fibers in Figure 2. This is also the cause of the σ_1–curve in Figure 5a decreasing a little at

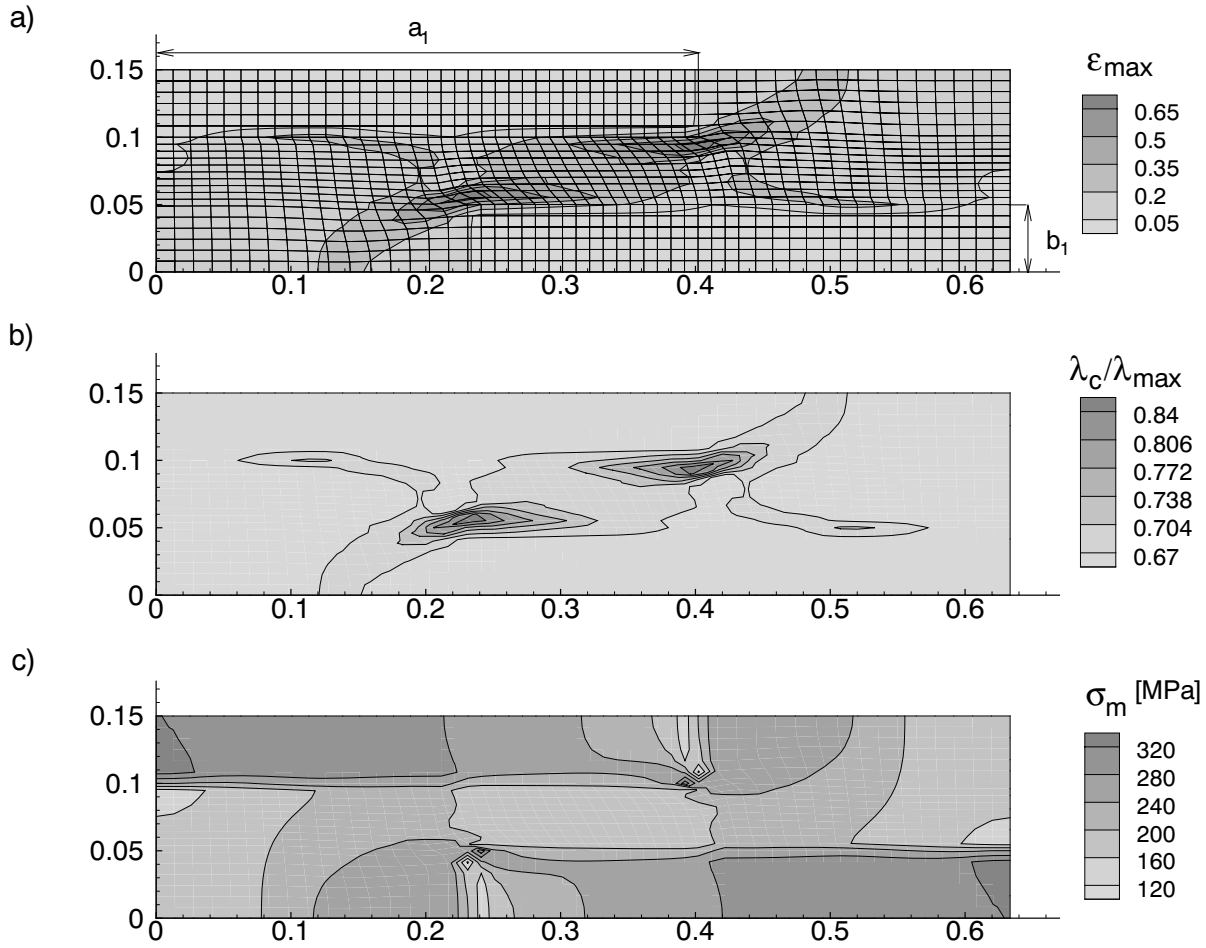

Figure 4. Contours of: (a) Maximum principal logarithmic strain ε_{max} (b) Normalized stretch λ_c/λ_{max} (c) Mean stress σ_m. Here $\alpha = 0$, $\varepsilon_1 = 0.0542$ and the region analyzed is specified by the normalized length $a_1/a = 2/3$ and by the widths $b/a = 1/4$, $b_1/b = 1/3$.

the end. The increase in the average stress σ_2 for lower α, see Figure 5a-c, is a result of the increasing stress triaxiality for decreasing α, which agrees with the increasing mean stresses σ_m in the polymer matrix between the fiber ends as α decreases.

In general E–glass fibers are nearly rigid with a Young's modulus $E = 72.0 - 85.0$ GPa which is more than 40 times higher than that of polycabonate and silimar glassy polymers. Therefore, an analysis has been carried out assuming that the fibers are infinitely stiff so that the originally applied boundary conditions along the fibers are applied directly to

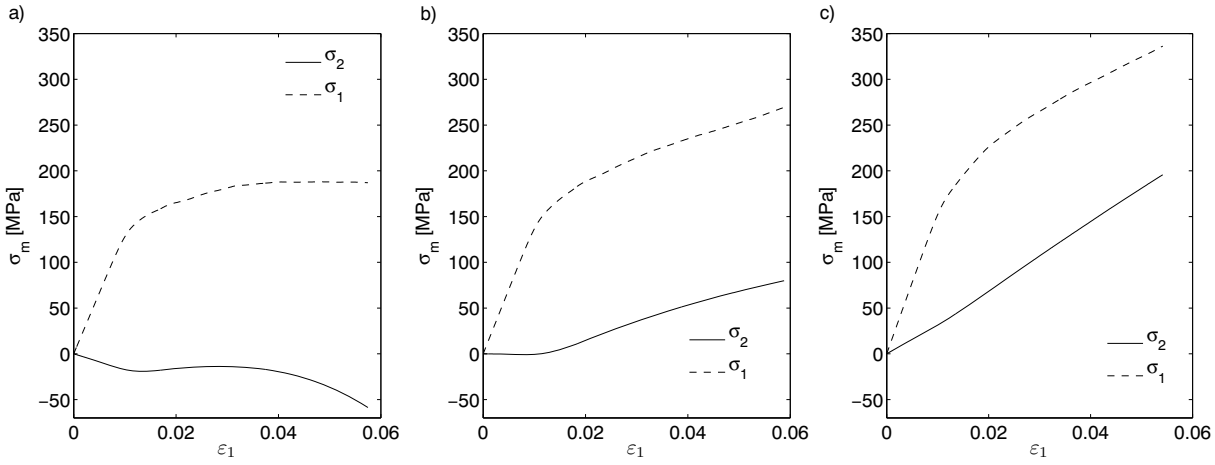

Figure 5. Average stress σ_1 along $y^1 = a$ and average stress σ_2 along $y^2 = b$ versus logarithmic strain ε_1 for the cases: (a) $\alpha = 0.75$, corresponding to Figure 2 (b) $\alpha = 0.50$, corresponding to Figure 3 (c) $\alpha = 0$, corresponding to Figure 4.

the polymer matrix at the fiber–matrix interface. The associated contourplots are shown in Figure 6 and the corresponding stress curves are illustrated in Figure 7. Comparison of Figure 6 for infinitely stiff fibers with Figure 4 for E–glass fibers confirms that the fiber Young's modulus $E = 72.0$ GPa is high enough to be well represented as a rigid fiber. All three contour plots in Figure 6 show contour levels of local strain and normalized stretch rather close to those in Figure 4, but it is noted that the overall strain $\varepsilon_1 = 0.0468$ in Figure 6 is smaller than $\varepsilon_1 = 0.0542$ (Figure 4) due to the infinite stiff fiber of Figure 6. This gives rather similar strain states in the two figures, but due to the smaller strain the stress concentrations found at the sharp fiber edges in Figure 4 are not quite achieved for the infinitely stiff fibers in Figure 6. From Figure 7 it is observed that the stress curves of the infinitely stiff fiber reinforced PC are slightly larger than those of the E–glass reinforced PC. Since the approximation of an inifinitely stiff fiber reinforced PC appears to be in rather good agreement with results for the same polymer reinforced by E–glass, the results for E–glass fibers are expected to also give a good approximation for other fibers with high stiffness.

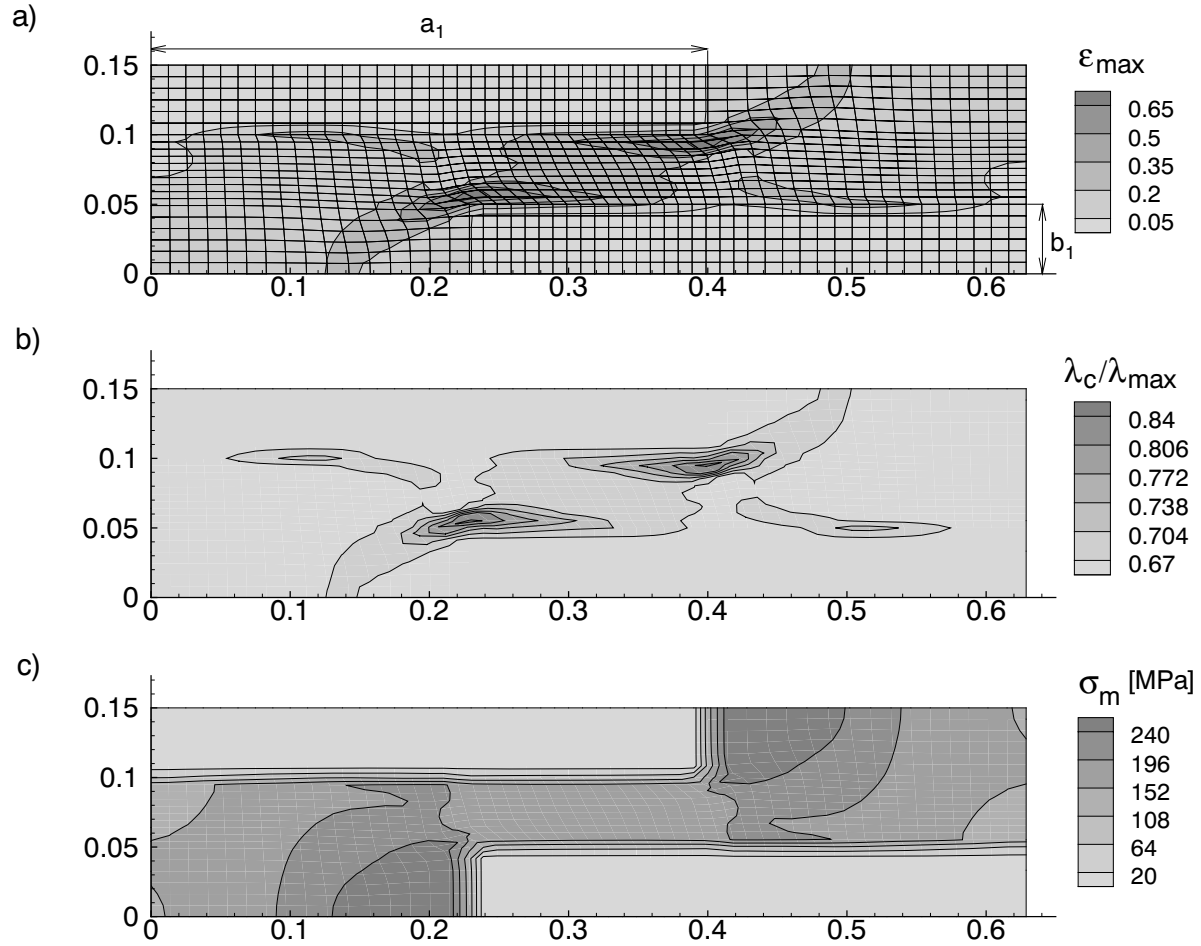

Figure 6. Contours of: (a) Maximum principal logarithmic strain ε_{max} (b) Normalized stretch λ_c/λ_{max} (c) Mean stress σ_m in case of infinitely stiff fibers. Here $\alpha = 0$, $\varepsilon_1 = 0.0468$ and the region analyzed is specified by the normalized length $a_1/a = 2/3$ and by the widths $b/a = 1/4$, $b_1/b = 1/3$.

Now, the sensitivity to the fiber spacing and the fiber thickness are to be investigated. Changes in geometry are made for the case of $\alpha = 0.50$ and the results are compared to the situation in Figure 3 with the original geometry and $\alpha = 0.50$. If the transverse distance between the fibers is increased as illustrated in Figure 8, a wider overall shear zone is seen compared to Figure 3, but the shear zone of the highest intensity in the middle has gotten slightly slimmer. The main effect of the larger fiber spacing is that strain levels

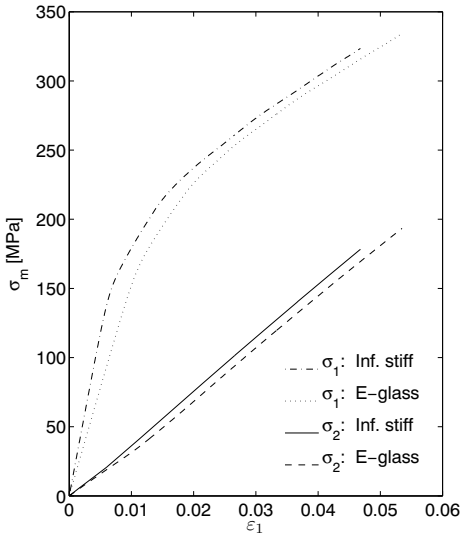

Figure 7. Average stress σ_1 along $y^1 = a$ and average stress σ_2 along $y^2 = b$ versus logarithmic strain ε_1 for infinitely stiff fibers (Figure 6) and E–glass fibers (Figure 4) compared when $\alpha = 0$.

as high as those in Figure 3 are now reached at larger overall strain $\varepsilon_1 = 0.0719$ as seen in Figure 8 for larger transverse distance between the fibers. In addition, the mean stress level in the matrix between the fibers is observed to have increased either due to the larger Poisson's ratio of the polymer matrix, which now takes up a larger volume fraction when the spacing has been increased, or because of the larger amount of material between the fibers to carry the load (compare Figure 8b and Figure 3c).

In Figure 9 the contours are shown for the case $\alpha = 0.50$ where the longitudinal spacing between the fiber ends is decreased. In order to achieve similar levels of the strain contour peak at the fiber corners as in Figure 3 for the original geometry and Figure 8 for larger transverse distance between the fibers the needed overall strain $\varepsilon_1 = 0.0873$ is even larger than the strain for the increased transverse fiber spacing in Figure 8. Since the fiber overlap in Figure 9 is smaller the shear zone in Figure 9a is shorter than the one in Figure 3a. The stress level in the middle of the matrix beween the fibers is increased relative to that of Figure 3c but at the same stage the matrix at the fiber ends and the fibers obtain

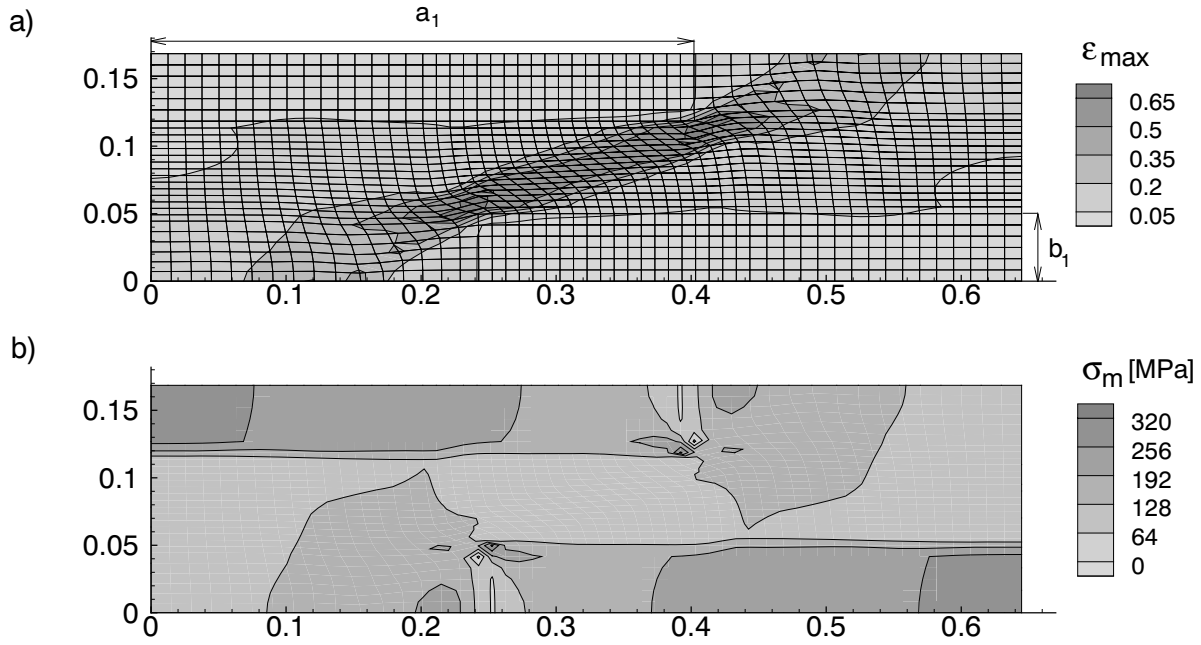

Figure 8. Contours of: (a) Maximum principal logarithmic strain ε_{max} (b) Mean stress σ_m. Here $\alpha = 0.50$, $\varepsilon_1 = 0.0719$ and the region analyzed is specified by the normalized length $a_1/a = 2/3$ and by the widths $b/a = 7/24$, $b_1/b = 2/7$.

a lower stress than that of the original geometry in Figure 3c. The increased stress level between the fibers occur since less material is available to transfer the main part of the load from one fiber to the other.

Figure 10 illustrates a case where the fibers are thinner, still for $\alpha = 0.50$, but the transverse spacing between the overlapping fibers is the same as that in Figure 3. The overall strain $\varepsilon_1 = 0.0727$ is larger than that in Figure 3, but not as large as the one illustrated in Figure 9 for the shorter fiber overlap. The thinner fibers in Figure 10 are more stretched than those in Figure 3 and therefore the thin–fiber case in Figure 10 will need a larger overall strain ε_1 in order to reach a similar local strain state e.g. at the sharp fiber ends and between the fibers.

In Figure 11 the curves of the average longitudinal stress σ_1 and the average transverse

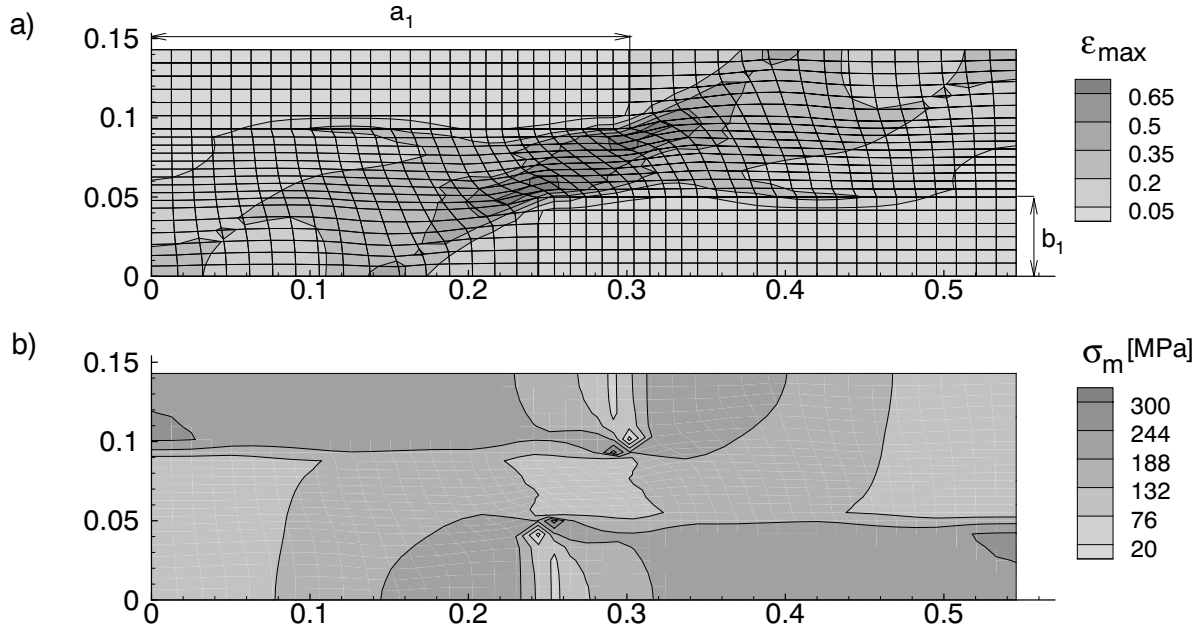

Figure 9. Contours of: (a) Maximum principal logarithmic strain ε_{max} (b) Mean stress σ_m. Here $\alpha = 0.50$, $\varepsilon_1 = 0.0873$ and the region analyzed is specified by the normalized lengths $a/a_{old} = 5/6$ (a_{old} is the length of the region considered in Figure 2), $a_1/a_{old} = 1/2$ and by the widths $b/a_{old} = 1/4$, $b_1/b = 1/3$.

stress σ_2 are shown for the previous three cases considered and the stress–strain curves in Figure 5b for the original geometry in Figure 3 are shown for comparison. Compared to the stress–strain curves in Figure 5b a lower σ_1 in Figure 11a and 11b is observed due to increased spacing of the fibers or a shorter fiber overlap which is in agreement with the fact that the longitudinal stiffness decreases in those cases. The σ_2 curves in Figures 11a (larger transverse spacing), 11b (shorter fiber overlap) and 5b (original geometry) do not deviate much. In case of thinner fibers smaller tranverse stresses σ_2 are obtained than in the other cases and the σ_1 curve is above that from Figure 5b. When comparing to Figure 3a it is seen that the thinner fibers in Figure 10a give a different deformation pattern at the fiber end, including a localized band of intense shearing along the opposite fiber. This leads to much higher σ_m in the fiber in Figure 10c than that in Figure 3c. Apparently, for the fixed strain ratio $\alpha = 0.50$ the case of thinner fibers leads to a larger difference

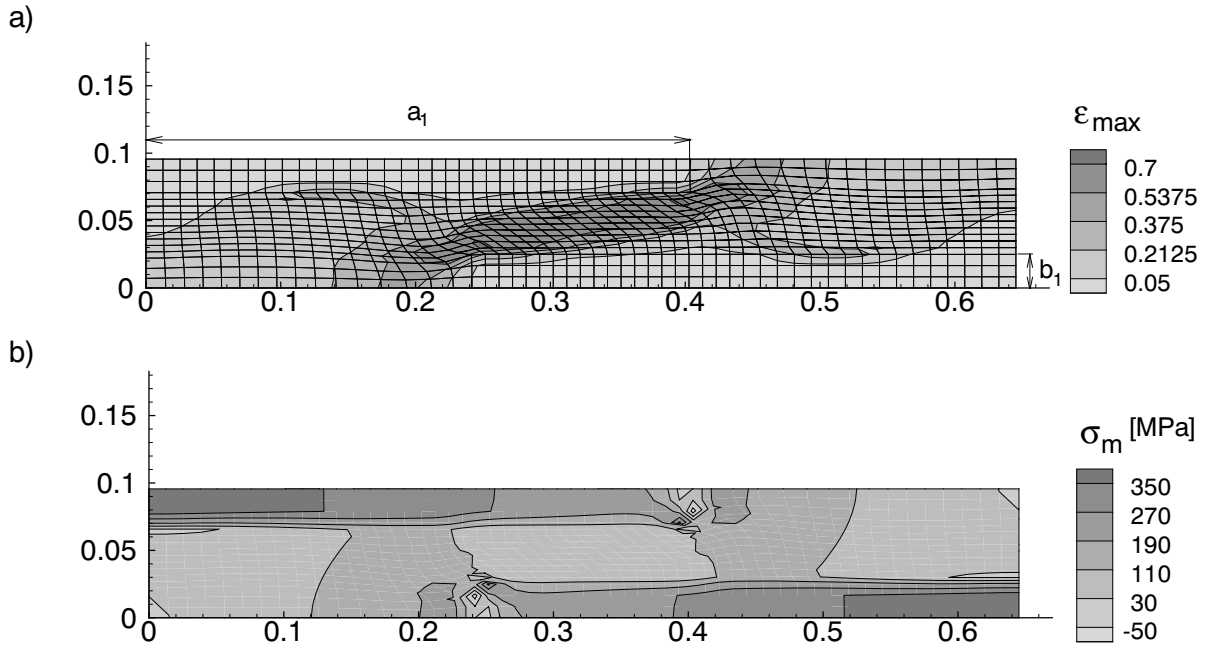

Figure 10. Contours of: (a) Maximum principal logarithmic strain ε_{max} (b) Mean stress σ_m. Here $\alpha = 0.50$, $\varepsilon_1 = 0.0727$ and the region analyzed is specified by the normalized length $a_1/a = 2/3$ and by the widths $b/a = 1/6$, $b_1/b = 1/4$.

between σ_1 and σ_2.

Next, a simple model analysis using periodicity for the polymer matrix is illustrated in Figure 12. This is a simplified way of modelling the mechanical behaviour of the polymer matrix between stiff fibers when the overlap length is much larger than the spacing. The height of the specimen $b/a_{old} = 1/12$ (a_{old} is the length of the region considered in Figure 2) corresponds to the transverse distance between the fibers in Figure 4 (the original geometry with $\alpha = 0$) and the thickness $a/a_{old} = 1/60$ of the strip of material analyzed is chosen equal to the element length along fibers in the previous analyses. The periodic specimen in Figure 12 is clamped at $y^2 = 0$ and at $y^2 = b$ the displacement $u_2 = 0$, while a prescibed velocity v as stated in eq. (5) is applied in the direction of the y^1–axis using $v_1 = (5/6)a_{old}$ s^{-1} and the ramping time $t_r = 0.02$ s as in all earlier cases analyzed. Periodicity requires that the displacements on both sides be the same, and therefore that

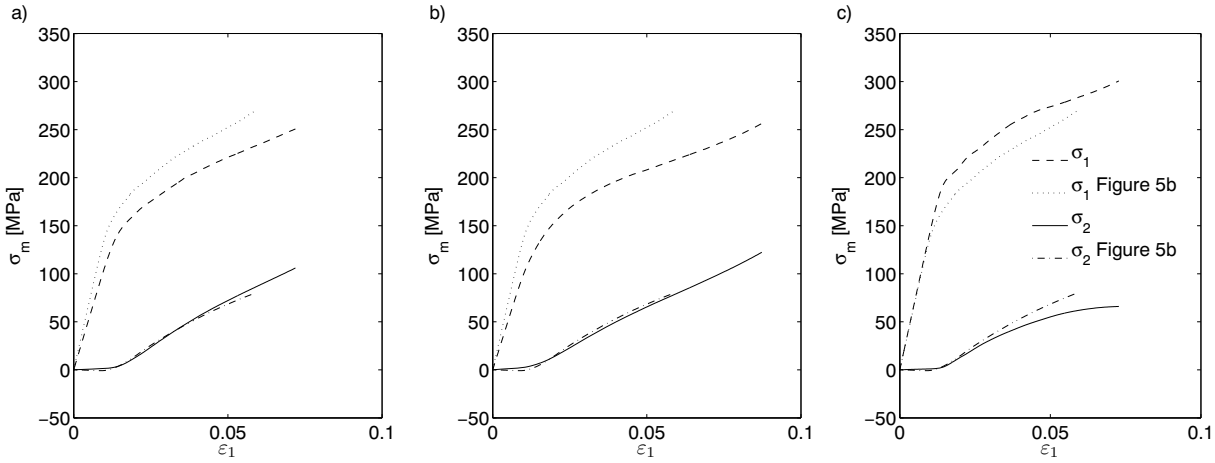

Figure 11. Average stress σ_1 along $y^1 = a$ and average stress σ_2 along $y^2 = b$ versus logarithmic strain ε_1 considering $\alpha = 0.50$ for the cases: (a) Larger transverse spacing between fibers, corresponding to Figure 8. (b) Shorter fiber overlap, corresponding to Figure 9. (c) Thinner fibers, corresponding to Figure 10.

the accelerations must be the same along the two sides. That is, if $F^1_{y^1=0}$ and $F^2_{y^1=0}$ are the nodal forces along $y^1 = 0$ in the direction of the y^1–axis and the y^2–axis respectively, $F^1_{y^1=a}$ and $F^2_{y^1=a}$ are the corresponding nodal forces along $y^1 = a$ in the direction of the y^1–axis and the y^2–axis respectively, and m_1 and m_2 are their respective nodal masses then the accelerations $\ddot{x}^i$ required at both locations in the two directions y^1 and y^2 have to satisfy

$$\ddot{x}^i = \frac{F^i_{y^1=0} + F^i_{y^1=a}}{m_1 + m_2} \tag{26}$$

where $i = 1, 2$ denote the two directions y^1 and y^2 respectively.

For the stage of the periodic case shown in Figure 12 the average shear strain is $\gamma = 0.489$. This average shear strain can be compared with the average shear strain in the matrix between the fiber overlap in Figure 4 (fiber–reinforced with the original geometry and $\alpha = 0$). The average shear strain γ used for comparison is calculated along the transverse line at the centre of the overlap in Figure 4 in order to neglect the influence from strain concentrations appearing at the fiber corners.

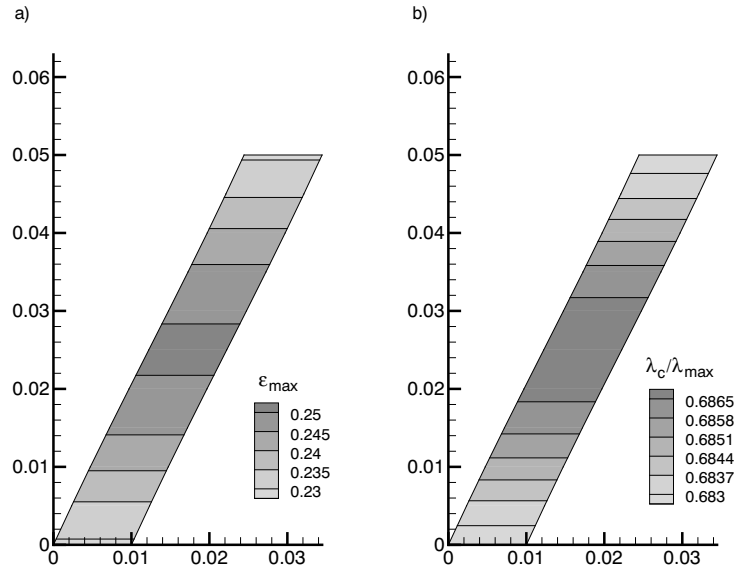

Figure 12. Contours of: (a) Maximum principal logarithmic strain ε_{max} (b) Normalized stretch λ_c/λ_{max} for the periodic version of the situation in Figure 4. Here the average shear strain $\gamma = 0.489$ and the region analyzed is specified by the initial thickness $a/a_{old} = 1/60$ and hight $b/a_{old} = 1/12$.

To trigger the possible onset of a localized shear zone as was done by Wu and Van der Giessen (1994) at $y^2 = b/2$, an imperfection is applied to the expression for the plastic strain increment $\dot{\gamma}^p$ in eq. (17) through multiplying $\dot{\gamma}_0$ by $1 + 0.01\sin(\pi y^2/b)$. The periodic case in Figure 12 is seen to have a slightly increased principal logarithmic strain ε_{max} at the centre, but no shear localization is visible at this stage.

Curves illustrating the shear stress τ at the fiber–matrix interface versus the average shear strain γ are shown in Figure 13 for the periodic case in Figure 12 and for fiber overlap in Figure 4. Considering Figure 4 the stress τ is calcutated from the forces in the five nodes along the interface where initially $y^1/a_{old} \in [29/60; 31/60]$ and $y^2/a_{old} = 1/6$, i.e. near the central transverse line from which γ is calculated. The curves in Figure 13 have maximum points at nearly the same value of $\gamma \approx 0.097$. However, the shear stress

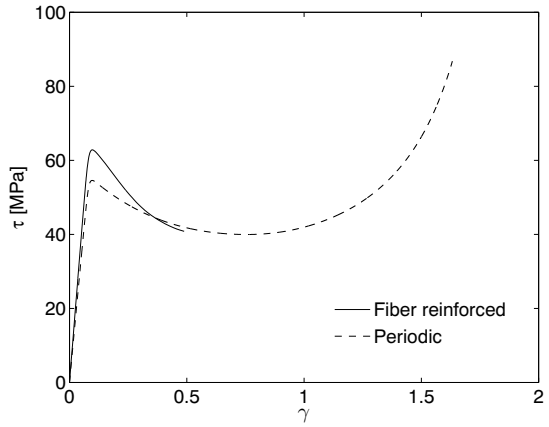

Figure 13. Shear stress τ versus average shear strain γ for the fiber reinforced case in Figure 4 and the periodic case in Figure 12. The situation in Figure 4 is illustrated at the average shear strain $\gamma = 0.489$. The curve illustrating periodicity has a cut off at $\lambda_c = 0.95\lambda_{max}$ incorporated, but this is never reached.

corresponding to the situation in Figure 4 with fiber overlap deviates somewhat from the shear stress obtained in case of infinitely long and stiff fibers, see Figure 12, showing that the fiber ends in Figure 4 affect the shear stress. Longer fiber overlap than that in Figure 4 would lower the upper stress curve towards the stress curve of periodicity. Nevertheless, Figures 13 and 12 indicate that the simple assumption of periodicity gives a reasonable approximation to the behaviour in the fiber overlap region far from fiber edges obtained earlier in Figure 4. Moreover, for the periodic case in Figure 13 the computation has been continued further so it is seen how the initial softening is followed by hardening due to network stiffening. Purely elastic deformation is here prescribed to be applied when a cut–off at $\lambda_c = 0.95\lambda_{max}$ is reached though this is not achieved yet in Figure 13. The point where the solid curve ends in Figure 13 is far from having reached the final network stiffening. Also, the deformed mesh in Figure 4a illustrates that shearing in the middle of the overlap zone is much less than the shearing reached in the most highly strained region.

For the periodic case shown in Figure 12 it was observed during the deformation that

the principal logarithmic strain ε_{max} at the centre started to increase slightly when the maximum on the stress–strain curve in Figure 13 was passed until the curve increases ($\gamma \approx 0.85$) due to hardening, but it never localized into a shear band. This is a consequence of shear zone propagation very similar to the neck propagation observed and described by Lindgreen et al. (2008). While the plastic strain first grows in the centre of the periodic region it later propagates away from the centre to the entire region as hardening initiates in the sheared region in the centre, $y^2 = b/2$, and the surrounding material passes the stress peak to reach plastic flow. The phenomenon of shear zone propagation, also called shear band widening, is further discussed by Wu and Van der Giessen (1994). When hardening is reached and the shear zone has stopped localizing the plastic strain propagation was observed to continue to the entire region until the plastic strain was practically the same all over the periodic region in agreement with the observations of Wu and Van der Giessen (1994).

4 Discussion

The development of diagonal high intensity shear zones in a metal matrix reinforced by transversely staggered fibers was studied previously by Llorca et al. (1991) and Tvergaard (2003). These analyses also showed high strain and stress concentrations emerging at the sharp fiber edges which are expected to eventually cause either cracking of the matrix or debonding and fracture along the fiber–matrix interface. In cases where the composite has a polymer matrix a somewhat similar tendency is expected which is further emphasized by experiments (Hampe and Marotzke (1992)) showing brittle fracture at the fiber–matrix interface in a glass fiber reinforced polycarbonate when subjected to fiber pull out. Moreover, the tensile strength of a polymer composite is limited due to low shear strengths as mentioned by Hampe and Marotzke (1992). Eventually this could lead to failure by mechanisms as those studied by Gearing and Anand (2004) for polycarbonate.

Also the present investigations of fiber reinforced thermoplast show a diagonal band of elevated shear intensity emerging in the polymer matrix between the overlapping glass fiber ends, see Figures 2, 3 and 4. The embedded fibers also cause high stress and strain concentrations at the sharp fiber edges as is seen from the figures just mentioned. It is found that modelling the fibers as infinitely stiff gives a good approximation of the E–glass fiber reinforced polycarbonate in terms of shear zone development, strain and stress distributions.

Depending on the value of the displacement ratio α in eq. (8) the strain contour plots develop at different speed with respect to ε_1. In case of nearly no volume change, corresponding to $\alpha = 0.75$ in Figure 2, the local strain levels shown in Figure 2 are reached rather fast. If α is decreased so that $\alpha = 0.50$ (Figure 3) similar local strain levels are reached a little slower than found for $\alpha = 0.75$. An even further decrease to $\alpha = 0$ requires a much larger ε_1 in order to reach these local strain levels than found for the larger values of α. In Figure 4 the high intensity strain concentrations at the sharp fiber edges are achieved, but since the observed shear zone is much weaker at the maximum strain level considered the specimen must be stretched even further to a larger value of ε_1 if an overall strain state as the ones in Figures 2a and 3a is to be reached. As α is reduced an increased level of the transverse stress σ_2 develops as observed from Figure 5.

Investigations of the sensitivity to fiber spacing and fiber thickness show that an increase of transverse fiber spacing (Figure 8), a shorter fiber overlap (Figure 9) or thinner embedded fibers cause the local strain levels to develop more slowly as functions of the overall strain ε_1. When either the transverse spacing is increased or the fiber overlap is shortened the mean stress level in the matrix between the fibers increases more rapidly. The average transverse stress σ_2 is not much affected while the average longitudinal stress σ_1 is somewhat reduced.

For $\alpha = 0$ the use of periodicity (Figure 12) allows for a simplified way of analyzing the

mechanical behaviour of the polymer matrix between the stiff fibers, approximating a case where the fiber overlap is much longer than the spacing, see Figure 4 for comparison. Figures 13 and 12 illustrates that the assumption of periodicity for the matrix between the fibers in Figure 4 can be reasonable. A shear zone is seen to develop in the matrix between the fibers, but no clear localization into a shear band is observed neither in the case of periodicity nor for the actual corresponding case in Figure 4. This is an effect similar to that of neck localization along a polymer tube wall (Lindgreen et al. (2008)) where the necks are observed to thin down to a certain point and propagate. Here when periodicity is considered, shear zone propagation occurs when the local shear stress τ within the shearzone starts to increase at approximately $\gamma \approx 0.85$. This effect was observed by Wu and Van der Giessen (1994) and it is very similar to the neck propagation found for polymer tubes (Lindgreen et al. (2008) and Lindgreen et al. (2007)).

Acknowledgements

The contribution of the authors Ph.D. thesis advisor, Professor Viggo Tvergaard, is gratefully acknowledged.

References

Andrews, M. C., Day, R. J., Patrikis, A. K., Young, R. J., 1994. Deformation micromechanics in aramid/epoxy composites. Composites 25(7), 745–751.

Arruda, E. M., Boyce, M. C., 1993. Evolution of plastic anisotropy in amorphous polymers during finite straining. Int. J. Plast. 9, 697–720.

Belytschko, T., Chiapetta, R. L., Bartel, H. D., 1976. Efficient large scale non-linear transient analysis by finite elements. Int. J. Numer. Meths. Engrg. 10, 579–596.

Berthelot, J. M., 2003. Transverse cracking and delamination in cross–ply glass–fiber and

carbon–fiber reinforced plastic laminates: Static and fatigue loading. Appl. Mech. Rev. 56(1), 111–147.

Boyce, M. C., Arruda, E. M., 1990. An experimental and analytical investigation of the large strain compressive and tensile response of glassy polymers. Polym. Engng. Sci. 30, 1288–1298.

Boyce, M. C., Parks, D. M., Argon, A. S., 1988. Large inelastic deformation of glassy polymers. part i: rate dependent constitutive model. Mech. Mater. 19, 193–212.

Boyce, M. C., Socrate, S., Llana, P. G., 2000. Constitutive model for the finite deformation stress–strain behavior of poly(ethylene terephthalate) above the glass transition. Polymer 41, 2183–2201.

Fleck, N. A., 1997. Compressive failure of fiber composites. Advanc. Appl. Mech. 33, 43–117.

Gearing, B. P., Anand, L., 2004. Notch–sensitive fracture of polycarbonate. Int. J. Solids Struct. 41, 827–845.

G'Sell, C., Jonas, J. J., 1979. Determination of the plastic behaviour of solid polymers at constant true strain rate. J. Mater. Sci. 14, 583–591.

Hampe, A., Marotzke, C., 1992. Adhesion of polymers to reinforcing fibres. Polymer Int. 28, 313–318.

Kalantar, J., Drzal, L. T., 1990. The bonding mechanism of aramid fibres to epoxy matrices. J. Mater. Sci. 25, 4186–4193.

Karbhari, V. M., Wilkins, D. J., 1990. A theoretical model for fiber debonding incorporating both interfacial shear and frictional stresses. Scripta Metall. Mater. 24, 1197–1202.

Krieg, R. O., Key, S. W., 1973. Transient shell response by numerical time integration. Int. J. Numer. Meths. Engrg. 7, 273–286.

Lai, J., Van der Giessen, E., 1997. A numerical study of crack-tip plasticity in glassy polymers. Mech. Mater. 25, 183–197.

Laws, N., Dvorak, G. J., 1988. Progressive transverse cracking in composite laminates. J. Comp. Mater. 22, 900–916.

Lindgreen, B., Tvergaard, V., Needleman, A., 2007. Bulge formation and necking in a polymer tube under dynamic expansion, report, Technical University of Denmark.

Lindgreen, B., Tvergaard, V., Needleman, A., 2008. Dynamic neck development in a polymer tube under internal pressure loading. Int. J. Solids Struct. 45, 580–592.

Llorca, J., Needleman, A., Suresh, S., 1991. An analysis of the effects of matrix void growth on deformation and ductility in metal–ceramic composites. Acta Metall. Mater. 39(10), 2317–2335.

Marsal, D., Ladevèze, P., Lubineau, G., 2006. On the out–of–plane interactions between ply damage and interface damage in laminates. In T. Sadowski (ed.), IUTAM Symposium on multiscale modelling of damage and fracture processes in composite materials Springer, 97–104.

Mulliken, A. D., Boyce, M. C., 2006. Mechanics of the rate-dependent elastic-plastic deformation of glassy polymers from low to high strain rates. Int. J. Solids Struct. 43, 1331–1356.

Seelig, T., Van der Giessen, E., 2002. Localized plastic deformation in ternary polymer blends. Int. J. Solids Struct. 39, 3505–3522.

Tvergaard, V., 2003. Debonding of short fibres among particulates in a metal matrix composite. Int. J. Solids Struct. 40, 6957–6967.

Tvergaard, V., Needleman, A., 1992. Effect of crack meandering on dynamic, ductile fracture. J. Mech. Phys. Solids 40(2), 447–471.

Tvergaard, V., Needleman, A., 2006. Three dimensional microstructural effects on plane strain ductile crack growth. Int. J. Solids Struct. 43, 6165–6179.

Tvergaard, V., Needleman, A., 2007. An analysis of thickness effects in the izod test, report, Technical University of Denmark.

Wu, P. D., Van der Giessen, E., 1994. Analysis of shear band propagation in amorphous glassy polymers. Int. J. Solids Struct. 31(11), 1493–1517.

Wu, P. D., Van der Giessen, E., 1996. Computational aspects of localized deformations in amorphous glassy polymers. Eur. J. Mech. A/Solids 15, 799–823.

Solid Mechanics

Department of
Mechanical Engineering

Technical University
of Denmark

Nils Koppels Allé, Building 404
DK-2800 Kgs. Lyngby, Denmark
Phone + 45 4525 4250
Fax + 45 4593 1475
info.fam@mek.dtu.dk
www.mek.dtu.dk

ISBN 978-87-89502-79-3

DCAMM
Danish Center for Applied
Mathematics and Mechanics
Nils Koppels Allé, Building 404
DK-2800 Kgs. Lyngby, Denmark
dcamm@dcamm.dk
www.dcamm.dk
ISSN 0903-1685